BACTERIAL MOTILITY PATTERNS IN CHEMOTAXIS AND POLYMER SOLUTIONS

by

Yang Yang

B.S. in Physics, University of Science and Technology of China, 2010

M.S. in Physics, University of Pittsburgh, 2012

Submitted to the Graduate Faculty of

the Kenneth P. Dietrich School of Arts and Sciences in partial fulfillment

of the requirements for the degree of

Doctor of Philosophy

University of Pittsburgh

2018

UNIVERSITY OF PITTSBURGH

KENNETH P. DIETRICH SCHOOL OF ARTS AND SCIENCES

This dissertation was presented

by

Yang Yang

It was defended on

April 27, 2018

and approved by

Xiao-Lun Wu, Professor

Hanna Salman, Associate Professor

James R. Faeder, Associate Professor

Rob Coalson, Professor

Vladimir Savinov, Professor

Dissertation Director: Xiao-Lun Wu, Professor

BACTERIAL MOTILITY PATTERNS IN CHEMOTAXIS AND POLYMER SOLUTIONS

Yang Yang, PhD

University of Pittsburgh, 2018

We investigate bacterial chemotactic strategies using run-tumble and run-reverse-flick motility patterns. The former is typically observed in enteric bacteria such as *Escherichia coli* and *Salmonella*, and the latter is observed in marine bacteria *Vibrio alginolyticus* and possibly exhibited by other polar flagellated species. It is shown that while the 3-step motility pattern helps the bacterium to localize near hot spots, an exploitative behavior, its exploratory potential in short times can be significantly enhanced by employing a non-Poissonian regulation scheme for its flagellar motor switches.

We also explored the interaction of polymer solutions with *Vibrio alginolyticus*. As the polymer concentrations increase, the flick of *Vibrio alginolyticus* is suppressed by the surrounding media. Two theoretical models are developed to explain the interaction, which confirms non-Poissonian property of *Vibrio alginolyticus* swimming interval distribution and reveals that motor fluctuations can be modeled with a damped harmonic oscillator. The motor fluctuations are coupled with the viscoelastic environment so that a "resonance-like" effect of the directional autocorrelation function of swimming bacteria can be observed. On the other hand, we only see the decreasing of swimming speed with increasing polymer concentration, which is different from the non-monotonic results of *E. coli* observed by Martinez et al. The swimming speed vs. concentration of polymer solutions shows a scaling law.

TABLE OF CONTENTS

LIST OF TABLES

LIST OF FIGURES

Dedicated to my parents, for all their support, love, sacrifices and encouragement.

PREFACE

I would like to express gratitude to my advisor, Dr. Xiao-Lun Wu. This work would not have happened without his understanding and careful help. I also acknowledge my thanks to the committee members, Dr. Hanna Salman, Dr. James R. Faeder, Dr. Rob Coalson and Dr. Vladimir Savinov for help and suggestion. I am grateful to all past and current members in Wu's lab and Hanna's lab, for their help and support: Dr. Li Xie, Dr. Jing He and Corey Dominick. I would also like to express my appreciation for the camaraderie provided by my old friends from my undergraduate college, USTC, and new friends in Pitt, in particular Dr. Huijie Yuan and Kuan Wang.

1.0 INTRODUCTION

1.1 THE DETAILS OF BACTERIA USED IN THE EXPERIMENTS

In this section, we will introduce the details of bacteria used in the experiment and in next section the physical models needed as our theoretical tools will be presented.

The bacteria in our study are wild-type *Escherichia coli* (*E. coli*) RP437 and *Vibrio alginolyticus* (*V. alginolyticus*) YM4. *E. coli* can be found in the human intestine system. It is a well-studied microorganism with a rod shape, the typical size of which is approximately 1 μm in width by 2 μm in length. Most strains of *E. coli* are not harmful. Instead, they are beneficial for microbial balance in the intestine system, aiding in digestion, and helping provide vitamin K [8].

V. alginolyticus is less studied than *E. coli* but still very well-known to researchers. It is a marine bacterium with a similar shape, and the typical size of a single cell is similar to *E. coli* [6].

1.1.1 Bacterial flagella and flagellar motor

Both *E. coli* and *V. alginolyticus* are flagellated bacteria, meaning that they can use this lash-like appendage to do locomotion. The wild-type *E. coli* has multiple flagella around its cell body while wild-type *V. alginolyticus* has a single polar flagellum, which is shown in Fig. 1. The typical size of *E. coli*'s flagella is about 10 μm long and 20 nm in thickness [9]. The average length and thickness of *V. alginolyticus*' flagella are about 5.5 μm and 20 nm, respectively [10][11].

Each bacterial flagellum is connected to a flagellar motor, located in the cellular mem-

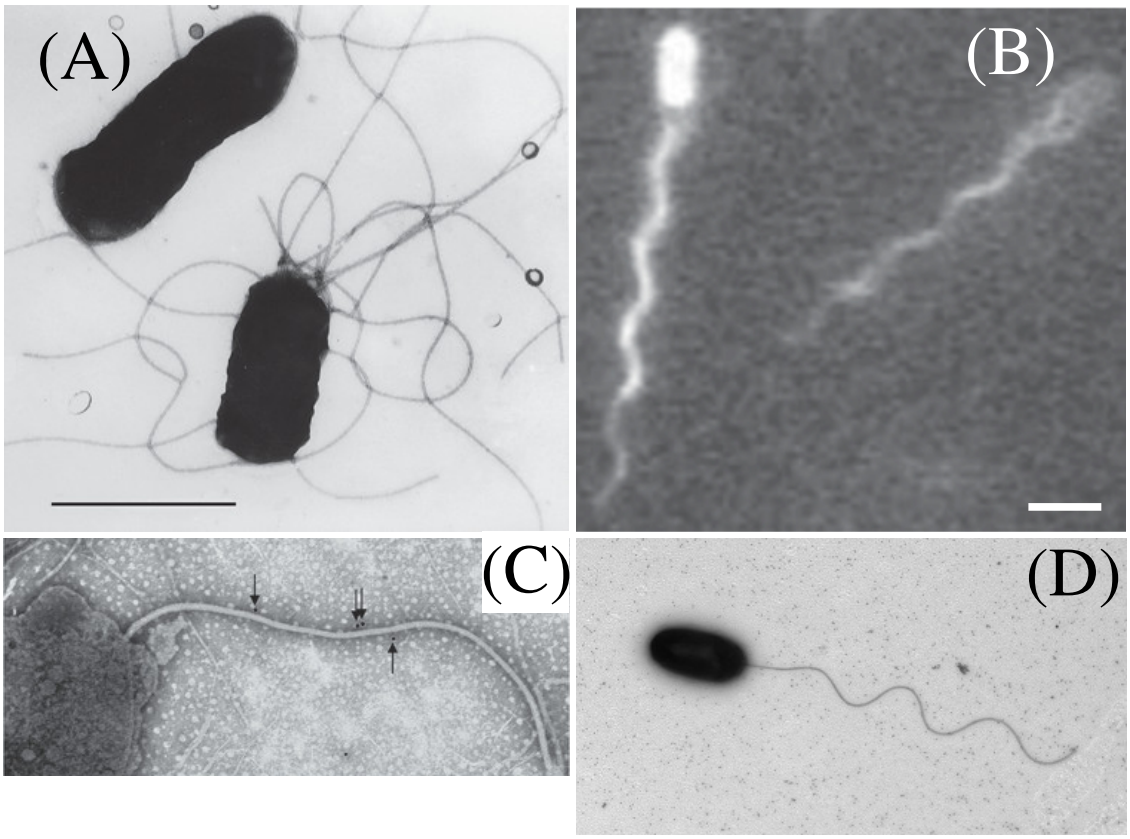

Figure 1: Flagella of *E. coli* and *V. alginolyticus*. (A) An electron microscope image of intact cell of *E. coli* K12 strain RP487. The bar represents 1.0 μm. (B) A real-time fluorescent image of flagellar bundles of *E. coli*. The bar represents 2.0 μm. (C) An immunogold electron microscope image of *V. alginolyticus*. (D) A phase contrast microscope image of *V. alginolyticus* bacterium [Kwangmin Son, CEE, MIT]. Here, (A) is from Figure 2 (A) of Ref. [1], (B) is from Figure 4 (A) of Ref. [2], and (C) is from Ref. [3].

brane [12]. The flagellar motor is akin to an electric motor and is one of the largest cellular machines, about 45 nm in diameter [9]. Powered by H^+ (*E. coli*) or Na^+ (*V. alginolyticus*) ion fluxes, they can rotate with the frequency around a few to several hundreds of hertz at a low load [13]. The record of highest speed of motor rotation is 1700 Hz, measured from the Na^+-driven motor of *V. alginolyticus* at 37°C [14].

1.1.2 Bacterial motility patterns

V. alginolyticus and *E. coli*'s motors can rotate bi-directionally. When the motor of *V. alginolyticus* rotates in counterclockwise (CCW, observed from a filament to a motor) direction, the flagellum will push cell body forward, and the corresponding swimming interval is named as a run interval. When the motor reverses its direction to clockwise (CW) direction, the cell moves backward, which is called a reverse interval. Because of cells swimming at low Reynolds numbers, the reverse backtracks the run interval. However, this is not the case for the run interval; upon a motor reversal from CW to CCW rotation, the compressive force transiently causes the flagellum to bend [4], deflecting the cell to a new random direction. So at the end of the reverse interval, there is a randomization process which is termed as a flick.

For *E. coli*, multiple flagella can bundle together, forming a left-handed helix when all motors rotate in CCW direction. The bundle pushes cell forward, which is termed as a run interval. If at least one motor reverses its direction to CW direction, the bundle falls apart, and the cell randomizes its direction, which is termed as a tumble. The bacterial motility patterns are based on these motor properties.

In summary, an *E. coli* bacterium swims in a fluid by run (CCW motors interval) and tumble (CW motor interval) as depicted in Fig. 2 (A). After many run-tumble (2-step) cycles, the bacterial track resembles a random walk. In comparison, a marine bacterium, such as *V. alginolyticus*, uses a single polar flagellum to navigate in seawater. Its motility pattern is 3-step cycles of run-reverse-flick as depicted in Fig. 2 (B). During the run (reverse) interval, the polar flagellar motor turns in the CCW (CW) direction. After several run-reverse-flick cycles, the trajectory of the marine bacterium also resembles a random walk.

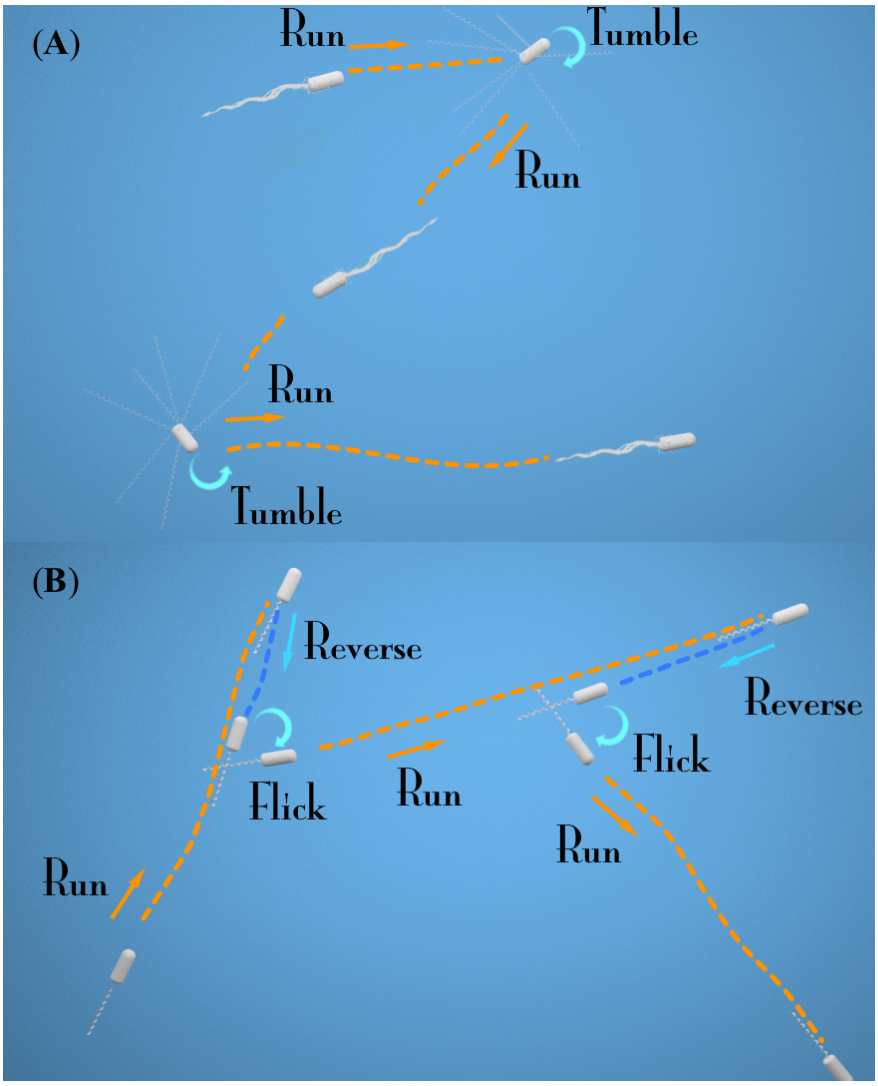

Figure 2: Bacterial motility patterns. The motility patterns of *E. coli* is a sequence of run and tumble intervals, which is a 2-step motility pattern. In comparison, wild-type *V. alginolyticus* uses a single polar flagellum to navigate in seawater. Its motility pattern is 3-step cycles of run-reverse-flick as depicted in (B). During the run (reverse) interval, the polar flagellar motor turns in the CCW (CW) direction. Because of swimming at low Reynolds numbers, the reverse backtracks the run interval. However, this is not the case for the run interval; upon a motor reversal from CW to CCW rotation, the compressive force transiently causes the flagellum to bend [4], deflecting the cell to a new random direction. After several run-reverse-flick cycles, the trajectory of the marine bacterium also resembles a random walk.

1.1.3 Chemotaxis

In a homogeneous motility buffer, bacteria move randomly in unbiased run-tumble or run-reverse-flick motility patterns. When a buffer is added with a chemoattractant or chemorepellent that forms a chemical gradient, a bacterium can do biased locomotion by adjusting its motility patterns to approach or keep away from the chemical source. This function of bacteria is known as chemotaxis. Bacteria detect the chemicals by temporal sensing rather than comparing chemical gradient in space due to its small size [15], which means that bacteria perform temporal comparisons to decide the gradient along swimming trajectories. In Chapter 2, we studied the bacterial exploration and exploitation behaviors for both *E. coli* and *V. alginolyticus* in chemotaxis.

1.1.4 Biosafety

It has been reported that some wild-type *V. alginolyticus* can cause wound infection, so special care is needed for a person with an abrasion or minor cut when dealing with them in the wild [16]. The strain YM4 used in our lab is subjected to the same lab safety requirements of *E. coli*.

1.2 BROWNIAN MOTION

1.2.1 Langevin equation

Because of the close similarity of Brownian motions and bacterial chemotactic swimming, for the convenience of a later discussion, let's first familiarize ourselves with Brownian dynamics. Brownian motion is named after British botanist Robert Brown who discovered it in 1827 [17]. He found that tiny flower pollens on water surface moved randomly under his microscope but failed to find out the reason. In 1906, Albert Einstein used kinetic molecular theory to explain why Brownian particles moved in this way [18] and started the understanding that random motion is due to thermal movements of surrounding water molecules.

Langevin equation is used to describe a Brownian motion particle, which is governed by the Newton's law of motion. Suppose the mass of the Brownian particle is m and it experiences a Stokes friction force $-\gamma\vec{v}$, where $\gamma > 0$ is a constant friction coefficient, the equation of motion is

$$m\frac{\mathrm{d}}{\mathrm{d}t}\vec{v}(t) = -\gamma\vec{v}(t) + \sqrt{2q}\vec{\eta}(t), \tag{1.1}$$

$$\frac{\mathrm{d}}{\mathrm{d}t}\vec{r}(t) = \vec{v}(t), \tag{1.2}$$

with $\vec{r}$ and $\vec{v}$ being the position and velocity of the particle, respectively.

The final term on the right-hand side in equation 1.1 characterizes the random force applied to the particle, which is due to the stochastic impacts of the liquid molecules. q characterizes the strength of random noise. The Cartesian components of $\vec{\eta}$(t) has a Gaussian distribution which satisfies

$$\langle\eta_i(t)\rangle = 0,\ \langle\eta_i(t)\eta_j(t')\rangle = \delta_{ij}\delta(t-t'). \tag{1.3}$$

After the integration we have

$$\vec{v}(t) = e^{-t/\tau}\left(\vec{v}_0 + \frac{\sqrt{2q}}{m}\int_0^t \mathrm{d}t'\vec{\eta}(t')e^{t'/\tau}\right), \tag{1.4}$$

where $\tau = m/\gamma$.

With Eq. 1.3 and 1.4, velocity autocorrelation function can be calculated,

$$\langle\vec{v}(t)\cdot\vec{v}(t')\rangle = e^{-(t+t')/\tau}\vec{v}_0^2 + \frac{dq}{\gamma m}\left(e^{-|t-t'|/\tau} - e^{-(t+t')/\tau}\right), \tag{1.5}$$

where d is dimension number, and the mean squared displacement (MSD) is,

$$\begin{aligned}\langle[\vec{r}(t)-\vec{r}(0)]^2\rangle &= \left\langle\left[\int_0^t \mathrm{d}t'\vec{v}(t')\right]\cdot\left[\int_0^t \mathrm{d}t''\vec{v}(t'')\right]\right\rangle \\ &= \int_0^t \mathrm{d}t'\int_0^t \mathrm{d}t''\langle\vec{v}(t')\cdot\vec{v}(t'')\rangle \\ &= \left(\vec{v}_0^2 - \frac{dq}{\gamma m}\right)\left(\tau - \tau e^{-t/\tau}\right)^2 + \frac{2dq\tau}{\gamma^2}\left(\frac{t}{\tau} - 1 + e^{-t/\tau}\right).\end{aligned} \tag{1.6}$$

The strength of noise q can be calculated from equipartition theorem. Suppose the equilibrium temperature of system is T, we have,

$$\frac{m}{2}\langle\vec{v}^2(t)\rangle = d\frac{k_BT}{2}, \tag{1.7}$$

where k_B is the Boltzmann constant. We can find that $q = \gamma k_B T$. Thus the coefficient of the first term in Eq. 1.6, $(\vec{v}_0^2 - \frac{dq}{\gamma m})$ becomes zero, and the MSD of the Brownian particle is simplified into

$$\langle[\vec{r}(t) - \vec{r}(0)]^2\rangle = \frac{2dq\tau}{\gamma^2}\left(\frac{t}{\tau} - 1 + e^{-t/\tau}\right). \tag{1.8}$$

In Chapter 2, we will see that the mathematical form of *E. coli*'s MSD (Eq. 2.8) is the same as the Brownian motion except for the time scale difference, where the time scale of Brownian motion and the motility pattern of *E. coli* are τ and τ_{ccw}, respectively. This indicates that for a long time, the behavior of *E. coli*'s motility pattern resembles a Brownian motion. In Chapter 2, the MSDs of *E. coli* and *V. alginolyticus* will be the tools to analyze the ability of bacteria seeking food.

1.2.2 Brownian motion in a harmonic potential

In Chapter 3, when we analyze the motility patterns of bacteria swimming in polymer solutions, we found that the viscosity and elasticity of polymer solutions cause bacterial swimming to behave like a damped harmonic oscillator. We believe that the oscillation is a result of flagellar motor that executes cycles. By adjusting the concentrations of polymer, we are able to observe a "resonance-like" state when the concentration of polymer solutions is close to the overlapping concentration, where polymer coils start to touch each other. The polymer property will be discussed in detail in Chapter 3. In this section, I prepare the mathematical tool describing particles moving in harmonic potential with the help of a Langevin equation. For this purpose, Eq. 1.1 is modified by adding a restoring force $-k\vec{r}(t)$,

$$\frac{\mathrm{d}}{\mathrm{d}t}\vec{v}(t) = -\omega_0^2\vec{r}(t) - \frac{\gamma}{m}\vec{v}(t) + \frac{\sqrt{2\gamma k_BT}}{m}\vec{\eta}(t), \tag{1.9}$$

where $\omega_0 = \sqrt{\frac{k}{m}}$, and we keep the noise as a Gaussian noise.

For simplicity, we make our derivation in one dimension,

$$\frac{\mathrm{d}}{\mathrm{d}t}v(t) = -\omega_0^2 r(t) - \frac{\gamma}{m}v(t) + \frac{\sqrt{2\gamma k_B T}}{m}\eta(t), \tag{1.10}$$

and results for higher spatial dimensions can be readily generalized. We can use a Fourier transform to analyze the stochastic differential equation. Here the forward and backward transformation is defined as $\tilde{X}(\omega) = \int_{-\infty}^{\infty} X(t)e^{-i\omega t}\,\mathrm{d}t$ and $X(t) = \int_{-\infty}^{\infty} \tilde{X}(\omega)e^{i\omega t}\frac{\mathrm{d}\omega}{2\pi}$.

In the Fourier space, $i\omega\tilde{r}(\omega) = \tilde{v}(\omega)$ and from Eq. 1.10 we have

$$i\omega\tilde{v}(\omega) = -\omega_0^2\tilde{r}(\omega) - \frac{\gamma}{m}\tilde{v}(\omega) + \frac{\sqrt{2\gamma k_B T}}{m}\tilde{\eta}(\omega). \tag{1.11}$$

The solutions for Eq. 1.11 are therefore

$$\tilde{r}(\omega) = \frac{\frac{\sqrt{2\gamma k_B T}}{m}\tilde{\eta}(\omega)}{i(\omega^2 - \omega_0^2) + \frac{\gamma}{m}\omega}, \tag{1.12}$$

and

$$\tilde{v}(\omega) = \frac{\frac{\sqrt{2\gamma k_B T}}{m}\tilde{\eta}(\omega)\omega}{i(\omega^2 - \omega_0^2) + \frac{\gamma}{m}\omega}. \tag{1.13}$$

We can find the power spectrum for position and velocity with the result

$$\tilde{S}_r(\omega) = |\tilde{r}(\omega)|^2 = \frac{\frac{2\gamma k_B T}{m^2}}{(\omega^2 - \omega_0^2)^2 + (\frac{\gamma}{m}\omega)^2}, \tag{1.14}$$

and

$$\tilde{S}_v(\omega) = |\tilde{v}(\omega)|^2 = \frac{\frac{2\gamma k_B T}{m^2}\omega^2}{(\omega^2 - \omega_0^2)^2 + (\frac{\gamma}{m}\omega)^2}. \tag{1.15}$$

An inverse Fourier transform of power spectrum leads to the autocorrelation functions for both position and velocity

$$C_r(t) = \int_{-\infty}^{+\infty} \tilde{S}_r(\omega)e^{i\omega t}\frac{\mathrm{d}\omega}{2\pi} = \frac{k_B T}{m\omega_0^2}e^{-\frac{\gamma}{2m}t}\left[\cos(\omega_0' t) + \frac{\gamma}{2m\omega_0'}\sin(\omega_0' t)\right], \tag{1.16}$$

and

$$C_v(t) = \int_{-\infty}^{+\infty} \tilde{S}_v(\omega)e^{i\omega t}\frac{\mathrm{d}\omega}{2\pi} = \frac{k_B T}{m}e^{-\frac{\gamma}{2m}t}\left[\cos(\omega_0' t) - \frac{\gamma}{2m\omega_0'}\sin(\omega_0' t)\right], \tag{1.17}$$

where $\omega_0' = \sqrt{\omega_0^2 - \gamma^2/4m^2}$. The autocorrelation function for velocity will be used to understand data collected in the experiment of bacteria swimming in polymer solutions in Chapter 3.

1.3 RESISTIVE-FORCE THEORY

1.3.1 The Navier-Stokes equation

Motility patterns of bacteria are affected by thermal fluctuations of a medium, but unlike powerless Brownian particles, they are also driven by flagellar motors. The hydrodynamics of flagellar propulsion reveals the other side of what influences bacterial motility. In this section, we seek help from the Navier-Stokes equation, which is Newton's second law of *fluid motion*, determining the motion of the medium where the microorganisms live. The Navier-Stokes equation of an incompressible Newtonian fluid is in the form

$$\rho\left(\frac{\partial \vec{u}}{\partial t} + \vec{u}\cdot\nabla\vec{u}\right) = -\nabla p + \eta\nabla^2\vec{u} + \vec{f}, \tag{1.18}$$

where ρ is the fluid density, η is the shear viscosity, and $\vec{f}$ is any external applied force per volume. The motion of the medium is indicated by a pressure field $p(\vec{r},t)$ and a velocity field $\vec{u}(\vec{r},t)$, with $\vec{r}(t)$ being the space point at time t [19][20].

1.3.2 Life at low Reynolds number

The Reynolds number is defined as the ratio of inertial force to viscous force, $Re = \rho a v/\eta$ [21], where v and a are typical velocity and length scales of a test object moving in the fluid. In the world of microorganisms, with the value of $\rho \approx 10^3\,\mathrm{kg/m^3}$, $\eta \approx 10^{-3}\,\mathrm{Pa\cdot s}$ (water), a swimming speed $v \approx 10\,\mu\mathrm{m/s}$, and a characteristic cell length scale $a \approx 1\,\mu\mathrm{m}$ (*E. coli*), the typical value of Re is $10^{-5} \ll 1$, which means that the inertia force in the Navier-Stokes equations can be neglected. So the left-hand side term in Eq. 1.18 is zero for inertialess case [19] and for the system without any external forces, we get the Stokes equation

$$-\nabla p + \eta\nabla^2\vec{u} = 0. \tag{1.19}$$

For incompressible medium, the mass continuity equation can also be simplified into

$$\nabla\cdot\vec{u} = -\frac{1}{\rho}\frac{\partial\rho}{\partial t} = 0. \tag{1.20}$$

Then, we have

$$\nabla^2 p = 0 \text{ and } \nabla^4 \vec{u} = 0. \tag{1.21}$$

Next, we try to calculate fluid motion induced by force distributions on a flagellum. For that purpose, we start by calculating the effect of a point force $\vec{F}\delta(\vec{r})$ which is located at the position of $\vec{r}$ following Ref. [19]. Eq. 1.19 becomes

$$-\nabla p + \eta \nabla^2 \vec{u} + \vec{F}\delta(\vec{r}) = 0, \tag{1.22}$$

and by applying $(\nabla\cdot)$ on both sides, we have

$$-\nabla^2 p + \nabla \cdot \left(\vec{F}\delta(\vec{r}) \right) = 0. \tag{1.23}$$

From the knowledge of $\nabla^2\left(\frac{1}{4\pi r}\right) = -\delta(\vec{r})$, we find the solution to the Stokes equation due to the point force

$$p = -\nabla \cdot \left[\frac{\vec{F}}{4\pi r} \right]. \tag{1.24}$$

Given a particular force field $\vec{F} = (F, 0, 0)$, its corresponding pressure field is

$$p = \frac{Fx}{4\pi r^3}, \tag{1.25}$$

and based on Eq. 1.19, the velocity field satisfies

$$\nabla^2 \vec{u} = \frac{1}{\eta}\nabla p = \frac{F}{4\pi\eta}\left(\frac{1}{r^3} - \frac{3x^2}{r^5}, \frac{-3xy}{r^5}, \frac{-3xz}{r^5} \right). \tag{1.26}$$

Eventually, we have the solution of $\vec{u}$ as follows

$$\begin{aligned} \vec{u} &= -\frac{1}{6} r^2 \left[\frac{F}{4\pi\eta} \nabla \frac{x}{r^3} \right] \\ &= \frac{F}{8\pi\eta}\left(\frac{x^2 + r^2}{r^3}, \frac{xy}{r^3}, \frac{xz}{r^3} \right). \end{aligned} \tag{1.27}$$

The values of $\vec{u}$ in radial and tangential directions are useful and they are given by

$$u_r = \frac{\vec{r}\cdot\vec{u}}{r} = \frac{F}{8\pi\eta}\left(\frac{2\cos\theta}{r} \right), \tag{1.28}$$

$$\tag{1.29}$$

and

$$u_\theta = \frac{F}{8\pi\eta}\left(\frac{-\sin\theta}{r}\right). \tag{1.30}$$

The velocity field described by Eq. 1.27 is the effect of a stokeslet of strength $(F, 0, 0)$ and is named as the stokeslet velocity field.

On the other hand, any velocity field $\vec{u} = \nabla\phi$ (where $\nabla^2\phi = 0$) satisfies the Stokes equation Eq. 1.19 and the mass continuity equation Eq. 1.20, where ϕ is called a *velocity potential*. By choosing a dipole velocity potential $\phi = -\nabla\cdot\left(\frac{\vec{G}}{4\pi r}\right) = \frac{Gx}{4\pi r^3}$, where $\vec{G} = (G, 0, 0)$ is the vector strength of the dipole, we can find that the corresponding velocity and pressure field become

$$\vec{u} = \frac{G}{4\pi}\left(\frac{1}{r^3} - \frac{3x^2}{r^5}, -\frac{3xy}{r^5}, -\frac{3xz}{r^5}\right), \tag{1.31}$$

$$p = 0. \tag{1.32}$$

The radial and tangential directions of $\vec{u}$ are

$$u_r = -\frac{G}{4\pi}\frac{2\cos\theta}{r^3}, \tag{1.33}$$

$$u_\theta = -\frac{G}{4\pi}\frac{\sin\theta}{r^3}. \tag{1.34}$$

This velocity field involves no external force on the fluid. It is called a dipole velocity field of strength $(G, 0, 0)$ or a *source-doublet*.

The stokeslet and dipole velocity field will be used to not only satisfy boundary conditions but also capture the velocity field of certain force distributions.

1.3.3 The normal motion of a circular cylinder section

We can use the results above to study the flagellum propulsion [19]. We want to see what the flow field would be given a line distribution of singular forces and the source-doublets. Assuming that the singular force is distributed in the range of $[-b, c]$ of z axis (see Fig. 3), the total strength of the force $\vec{F}$ is related to the force distribution with the result $\vec{F} = \int_{-b}^{c} f\hat{x}\,\mathrm{d}z$, where the unit force $(f\,\mathrm{d}z, 0, 0)$ is located in $(z, z + \mathrm{d}z)$.

We hope to see the velocity field on the cylinder $x^2 + y^2 = a^2$, where $a \ll b$ and $a \ll c$. With Eq. 1.27, an approximated velocity field on $x^2 + y^2 = a^2$, and $z = 0$ is

$$\vec{u} = \frac{f}{8\pi\eta}\left(\frac{2x^2}{a^2} + \log\frac{4cb}{a^2}, \frac{2xy}{a^2}, 0\right). \tag{1.35}$$

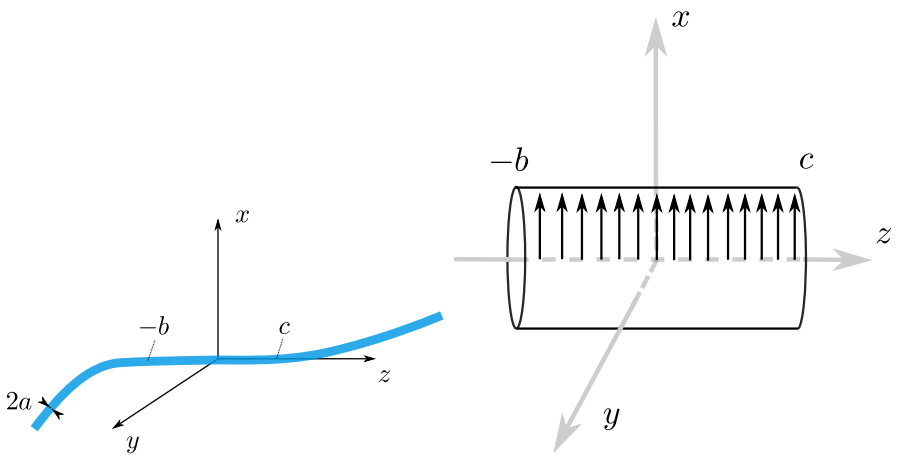

Figure 3: A line distribution of singularities on a cylinder segment in its normal direction. The left figure represents a segment of a flagellum with a diameter $2a$ and the right figure shows one section that we want to analyze, with the length $b + c$. The direction of the unit force follows the normal direction of the circular cylinder section, which is in x-axis here.

The velocity field varies around the circle on the surface of the cylinder, but it is possible to remove the variation with a similar configuration of source-doublets. For the velocity field due to the source-doublets with the same space configuration, we have

$$\vec{u} = \frac{g}{4\pi}\left(\frac{2}{a^2} - \frac{4x^2}{a^4}, -\frac{4xy}{a^4}, 0\right). \tag{1.36}$$

By choosing $g = \frac{fa^2}{4\eta}$, the sum of above two fields gives

$$\vec{u} = \frac{f}{8\pi\eta}\left(1 + \log\frac{4cb}{a^2}, 0, 0\right). \tag{1.37}$$

This result means that a section of a circular cylinder with geometry $2\pi a^2 \times (b+c)$ moves with the velocity in Eq. 1.37 when a uniform force $(f, 0, 0)$ is applied to the cylinder per unit length.

1.3.4 The tangential motion of the circular cylinder section

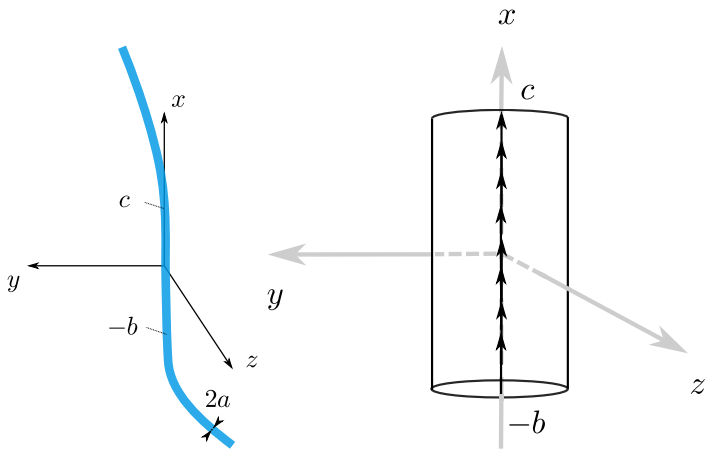

Figure 4: A line distribution of singularities on a cylinder segment in its tangential direction. Unlike Fig. 3, the direction of the forces follows the tangential direction of the circular cylinder section.

Similarly, the velocity field can be calculated given a force distributed along the tangential direction of the circular cylinder section. Following the setup in Fig. 4, the forces are in x-axis, in the range of $[-b, c]$. The corresponding velocity field is

$$\vec{u} = \frac{f}{8\pi\eta}\left(-2 + 2\log\frac{4cb}{a^2}, 0, 0\right). \tag{1.38}$$

This means that a line distributed tangential singular force generates the velocity field in Eq. 1.38. Combining the Eq. 1.37 and Eq. 1.38, we can find that given same net force f applied in tangential and normal direction of cylinder, the magnitude of velocity field for

the former is almost twice as fast as that of latter. We define the normal and tangential resistance coefficient as follows,

$$k_n = f_n/u = \frac{8\pi\eta}{1+\log\frac{4cb}{a^2}}, \tag{1.39}$$

$$k_t = f_t/u = \frac{4\pi\eta}{-1+\log\frac{4cb}{a^2}}. \tag{1.40}$$

These two coefficients will be used in the next section and Chapter 3.

1.3.5 Resistive-force theory of the flagella

In this section, we follow Lighthill's way to calculate the thrust force and torque generated by flagella based on previous section's results [19]. For a flagellum, the length of which is l when stretched straight, we set up a coordinate system in Fig. 5 (A) to describe it. The left-handed helix pointing backwards along x axis can be described as

$$\vec{r}(s) = (x, y, z) = (x(s), y(s), z(s)), \tag{1.41}$$

where s is curvilinear distance from the bare of the flagellum (see Fig. 5 (A)). Λ is the wavelength along the curved flagellum and $\Lambda\cos\psi = \Lambda\alpha = \lambda$, in which ψ is the helix angle, $\cos\psi = \alpha$, and λ is the pitch of the helix.

In the frame of cell body (see Fig. 5 (B)), when the flagellum rotates counterclockwise with the angular velocity ω, one test point moves with a tangential velocity c, which has been labelled as a red vector. The corresponding phase speed of the helical wave thus propagates upwards with the velocity $\vec{v} = v\hat{x} = \alpha c\hat{x}$, relative to the cell body.

For the bacterium, assuming that the swimming velocity in the fluid is $\vec{u} = -u\hat{x}$, so the velocity of the wave relative to the fluid is $(v-u)\hat{x}$. We can find the tangential velocity of flagellum relative to the fluid

$$(v-u)\hat{x}\cdot\hat{t}\hat{t} - c\hat{t} = (v-u)\cos\psi\hat{t} - c\hat{t} = [(v-u)\cos\psi - c]\hat{t}, \tag{1.42}$$

where $\hat{t}$ indicates the unit tangential vector along the increasing s direction. The normal velocity relative to the fluid is $(v-u)\hat{x}\cdot\hat{n}\hat{n} = (v-u)\sin\psi\hat{n}$.

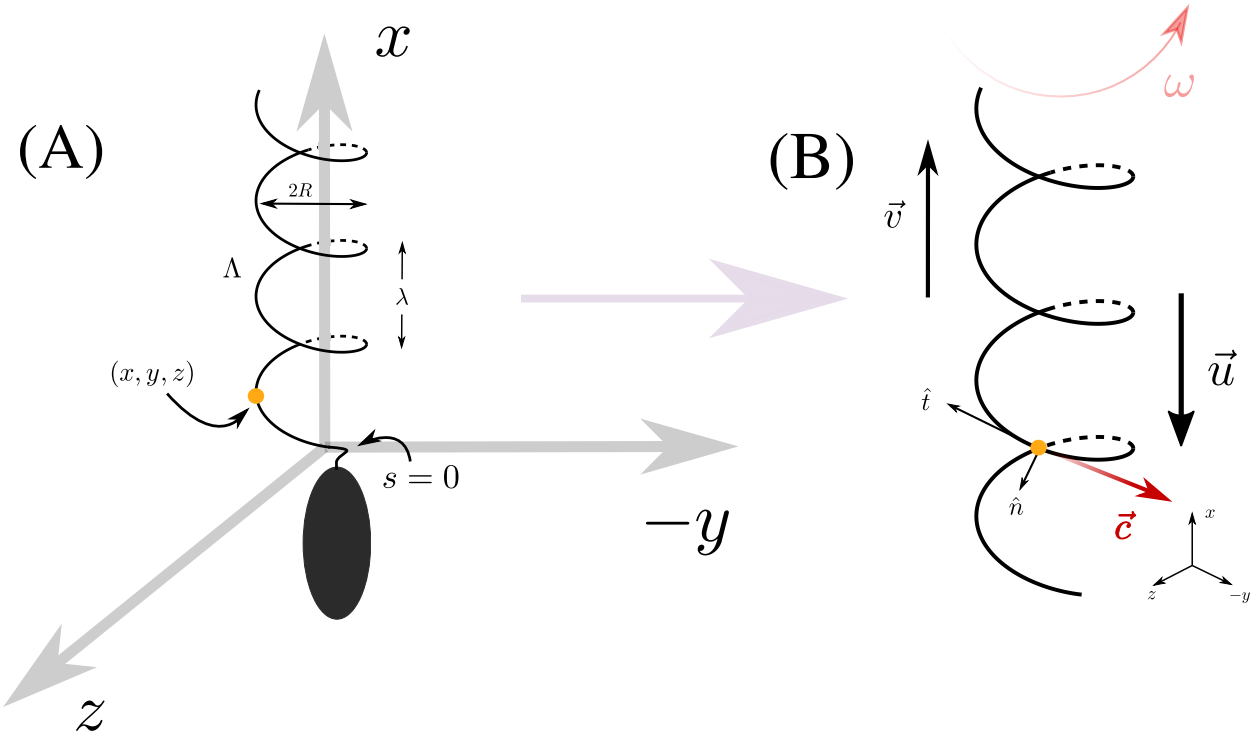

Figure 5: Flagellum details for resistive-force theory derivation. In (A), a schematic cell is placed along x-axis and a test point on the flagellum has been labeled with yellow color. R is the radius of the helix, Λ characterizes the wavelength along the curved flagellum, and λ is the pitch of the helix. In (B), the flagellum from (A) is shown and represents the cell body frame. The flagellum rotate in CCW direction with angular velocity ω and $\vec{v}$ is the phase velocity of the helical wave. For the yellow test point, its tangential velocity $\vec{c}$ has been marked with red color. $\hat{t}$ and $\hat{n}$ are the tangential and normal direction at this point, respectively. The velocity $\vec{u}$ is the cell swimming velocity relative to fluid.

With the tangential resistance coefficient k_t and normal resistance coefficient k_n obtained previously, we can find the trust force F_f by integrating over the whole flagellum,

$$F_f = \int_0^l \left\{ k_t \Big[(v-u)\cos\psi - c \Big] \cos\psi + k_n (v-u) \Big[1 - \cos^2\psi \Big] \right\} \mathrm{d}s. \tag{1.43}$$

We know that

$$\int_0^l \cos\psi \, \mathrm{d}s = \alpha l, \tag{1.44}$$

and

$$\int_0^l \cos^2\psi \, \mathrm{d}s = \beta l, \tag{1.45}$$

where $\beta = \cos^2\psi$.

After integration, the thrust force is given by

$$\begin{aligned} F_f &= k_t l \Big[(v-u)\beta - v \Big] + k_n l \Big[(v-u)(1-\beta) \Big] \\ &= lv \Big[k_t(\beta - 1) + (1-\beta)k_n \Big] - lu \Big[\beta k_t + (1-\beta)k_n \Big]. \end{aligned} \tag{1.46}$$

The torque N_f can be calculated by using the component of $\mathrm{d}F_f$ normal to the helical axis multiplied by the lever arm, which is the helix radius R,

$$\mathrm{d}N_f = \left\{ -Rk_t \Big[(v-u)\cos\psi - c \Big] \sin\psi + Rk_n (v-u) \sin\psi \cos\psi \right\} \mathrm{d}s. \tag{1.47}$$

The total torque is

$$\begin{aligned} N_f &= \int_0^l \left\{ -Rk_t \Big[(v-u)\cos\psi - c \Big] \sin\psi + Rk_n (v-u) \sin\psi \cos\psi \right\} \mathrm{d}s \\ &= -Rk_t \left[(v-u) l \cos\psi \sin\psi - \frac{vl}{\cos\psi} \sin\psi \right] + Rk_n (v-u) l \sin\psi \cos\psi \\ &= vRl(-k_t \cos\psi \sin\psi + k_t \tan\psi + k_n \sin\psi \cos\psi) - Rlu(-k_t \sin\psi \cos\psi + k_n \sin\psi \cos\psi) \\ &= vRl(-k_t \alpha \sqrt{1-\beta} + k_t \frac{\sqrt{1-\beta}}{\alpha} + k_n \alpha \sqrt{1-\beta}) - Rlu(k_n + k_t)\alpha\sqrt{1-\beta}). \end{aligned} \tag{1.48}$$

The thrust force and torque can be expressed in the following concise way,

$$\begin{bmatrix} -F_f \\ N_f \end{bmatrix} = \begin{bmatrix} A & -B \\ -B & D \end{bmatrix} \cdot \begin{bmatrix} u \\ \omega \end{bmatrix}, \tag{1.49}$$

where $\omega = \frac{2\pi v}{\lambda}$ is the flagellum rotation angular velocity.

We can find that the matrix elements A, B and D are

$$A = k_n l(1-\beta)\big(1+\gamma_k \frac{\beta}{1-\beta}\big), \tag{1.50}$$

$$B = k_n l(\frac{\lambda}{2\pi})(1-\beta)\big(1-\gamma_k\big), \tag{1.51}$$

and

$$D = k_n l(\frac{\lambda}{2\pi})^2(1-\beta)\big(1+\gamma_k \frac{1-\beta}{\beta}\big), \tag{1.52}$$

where $\gamma_k = k_t/k_n$.

It is due to this thrust force and torque that the flagellum can push or drag a bacterium in a liquid environment. These results give a propulsion matrix, from which we can calculate the thrust force and torque if we know the velocity and angular velocity of the flagellum. We will discuss this in detail in Chapter 3.

The purpose for me to write down the derivation in detail here is that I hope to document the theoretical background. When I tried to tackle the research problem, I explored for a long time to figure out which part of theory is essential and effective to capture experimental results. So I think this is instructional if anyone will do similar experiments.

2.0 A NON-POISSON FLAGELLAR MOTOR SWITCH INCREASE BACTERIAL CHEMOTAXIS POTENTIAL

2.1 INTRODUCTION

This chapter is about the performance of different bacterial searching strategies for scarcely distributed chemical traces in a fluctuating environment. This is the situation a bacterium encounters in a pelagic micro-habitat where nutrients released from, say, marine snows or lysed planktons are quickly dispersed by turbulent fluid flows. Turbulent action stretches and folds nutrients into thin striations and significantly enhances their dispersal in water. To sequester these ephemeral nutrient patches, microorganisms develop different niches to gain advantage over their competitors. Surveys of coastal water samples have revealed that the majority of motile bacteria are polar flagellated, and they swim rapidly with a speed of ≈ 100 times of their body lengths per second [22]. The most documented motility pattern of marine bacteria is run-and-reverse, which is consistent with their flagellation pattern. The fact that peritrichously flagellated bacteria were rarely found in such environment suggests that the run-tumble motility pattern of *E. coli,* which is by far the best studied, is not adopted by marine species. We recently found that marine bacterium *V. alginolyticus,* and possibly others such as *Pseudoalteromonas haloplanktis,* incorporate a randomization step in their motility patterns; namely these bacteria whirl their flagellum at the end of the reverse interval causing the cell body to deflect in a new random direction before resuming forward swimming [6]. This characteristic movement, which we termed a flick, makes a sharp kink in the bacterial trajectory and signals the beginning of each run-reverse-flick cycle (see Fig. 2 (B)). Using fluorescence video microscopy and optical trapping, we found that the flick is very brief $\sim 50\,\text{ms}$ and is a part of the forward run [6]. A recent study by Son et al.

demonstrated that the flick movement results from an elastic instability of the flagellar hook when it is compressed by the propulsive force when the motor switches from clockwise (CW, reverse) to counter clockwise (CCW, run) rotation [4].

As illustrated in Fig. 2, the fundamental difference between the run-tumble and run-reverse-flick motility patterns is that the latter is able to backtrack, revisiting spaces that have been covered in the previous run interval. This type of motility pattern is adopted by many motile marine bacteria, suggesting its usefulness. In the present work we examine how different motility patterns contribute to chemotaxis via the important characteristics of bacterial diffusivity [23, 24]. Since the motility patterns are regulated by the interval distributions $P_x(\Delta_x)$, where Δ_x is the dwell time for the motor state x, our work will examine different distributions of Δ_x and how these distributions affect chemotaxis. For *E. coli*, it is well documented that both the run Δ_{ccw} and tumble Δ_{cw} intervals are exponentially distributed, $P_x(\Delta_x) = \exp(-\Delta_x/\tau_x)/\tau_x$ with τ_x being the mean and $x =$ (CCW, CW) [25]. However, for *V. alginolyticus*, our measurements show that both forward Δ_f and backward Δ_b swimming interval distributions are strongly peaked at finite times, and it is only in long times that the distributions are exponential [6]. The short-time ($\Delta_x/\tau_x \ll 1$) inhibition is very strong, suggesting that the motor has a refractory period shortly after a reversal, where $x = (f, b)$. This behavior is very different from *E. coli*, showing that this marine bacterium does not regulate its motor switch using a Poisson process. Our research presented herein demonstrated that there may be a good biophysical reason for this phenotype, i.e., the marine microorganisms can use reversibility enforced by the short-time inhibition to enhance their exploitative behavior.

A quantitative measure of a bacterium's chemotactic potential, namely its ability to explore and exploit a natural habitat, is the bacterial diffusivity $D(\tau)$, which measures the space covered by the microorganism in a given time τ. In this chapter, we first present experimental measurements of $D(\tau)$ for the marine bacterium *V. alginolyticus* YM4 in different chemical environments and compare these measurements with commonly studied *E. coli* strain RP437. We then developed a mathematical model that allows the time-dependent $D(\tau)$ to be calculated based on microscopic motility patterns with an *arbitrary* interval distribution $P_x(\Delta_x)$. Our work demonstrates that even though the 3-step motility pattern can

significantly reduce bacterial diffusivity in a long time, its short-time explorative potential is significantly enhanced by employing a non-Poisson regulation scheme for the flagellar motor switch.

2.2 RESULTS AND DISCUSSIONS

2.2.1 Experimental observations

While detailed bacterial culture conditions and measurement techniques are discussed in Appendix C, here a brief description is provided. The bacteria *E. coli* RP437 and *V. alginolyticus* YM4 were grown to a mid-exponential phase in M9 and VPG media, respectively, and were transferred to their corresponding motility buffers. Both bacteria were incubated in their corresponding motility buffer for > 30 minutes before transferred to an observation chamber. Two sets of measurements were conducted for RP437: (i) in the homogeneous motility buffer (MB) and (ii) in the presence of a small source of a chemoattractant, serine. Three different sets of measurements were conducted for YM4: (i) in the homogeneous motility (TMN) buffer, (ii) in TMN with a uniform repellent phenol, and (iii) in the presence of a small source of serine as above. In all cases individual bacteria were followed by video microscopy in a phase contrast mode, and the image plane was set at $\sim 100\,\mu$m away from the surface to minimize distortion of swimming trajectories [26]. The bacterial trajectories were digitized using ImageJ and a home-developed software package. Each bacterium was followed for as long as possible, typically a few seconds to as long as 20 s, before it swam out of view. This yields a time series $\vec{r_i} = (x_i(t_i),\, y_i(t_i))$ with the successive time points t_i determined by the standard video rate of 30 fps or $\Delta t = 33$ ms. For each bacterial trajectory, the mean-squared displacement (MSD) $\vec{r}^2(\tau) = \sum_{i=1}^{N-n} \left((x_{i+n} - x_i)^2 + (y_{i+n} - y_i)^2\right)/(N-n)$ can be calculated and after averaging over many bacteria, one finds the population averaged value $\mathrm{MSD}(\tau) = \langle \vec{r}^2(\tau) \rangle$, where $\tau = n\Delta t$ with n being an integer, and N is the length of the trajectory.

Figure 6 displays MSDs for *E. coli* (A) and *V. alginolyticus* (B) in the uniform buffers.

One observes that for *E. coli*, there exist two regimes; for short times ($\tau < 1.5\,\mathrm{s}$), $\mathrm{MSD}(\tau) \propto \tau^2$, suggesting a "ballistic-like" motion, and for long times ($\tau > 1.5\,\mathrm{s}$), $\mathrm{MSD}(\tau) \propto \tau$, which is normal diffusion. The slope of this latter regime yields the long-time diffusion coefficient $D_0 = 95 \pm 7\,\mu\mathrm{m}^2/\mathrm{s}$. By comparison, we found that MSD for *V. alginolyticus* is significantly different; it consists of three regimes. For $\tau < 0.5\,\mathrm{s}$, the MSD increases as τ^2 as in the case of *E. coli*, and it is followed by a rapid, quasi linear dependence on τ. Unlike *E. coli*, this rapid increase in MSD does not persist but is interrupted by a much slower linear τ dependence for $\tau \geq 1.2\,\mathrm{s}$. For *V. alginolyticus,* the long-time diffusivity $D_0 = 102 \pm 9\,\mu\mathrm{m}^2/\mathrm{s}$ is therefore comparable to that of *E. coli,* but its maximum instantaneous diffusivity $D_{max}\left[\equiv \frac{d}{d\tau}\mathrm{MSD}(\tau)/4\right] = 166 \pm 8\mu\mathrm{m}^2/\mathrm{s}$ ($0.5 \leq \tau \leq 1.2\,\mathrm{s}$) is considerably greater. We next investigate the diffusivity of YM4 subject to 10 mM phenol in TMN buffer. Previous studies have shown that phenol elicits a chemorepellent response in *V. alginolyticus*, and the bacterium is not adapted to this chemical [27]. Observations show that the bacteria alter their swimming directions rapidly with the typical dwell times in both swimming directions being shorter than those in TMN. These characteristics are clearly displayed in Fig. 6 (C) in which we found that overall MSD is smaller with $D_0 = 23 \pm 3\,\mu\mathrm{m}^2/\mathrm{s}$ and $D_{max} = 94 \pm 5\,\mu\mathrm{m}^2/\mathrm{s}$; both are significantly less than those measured in TMN without phenol.

Figure 6 (D) displays the MSD vs. τ measured for YM4 in the presence of a localized chemoattractant created from a micropipette filled with 1 mM serine. The chemical is distributed over a small radius $\sim 10\,\mu\mathrm{m}$ [5]. We found that the measured curve in this case still consists of three regimes as those in Figs. 6 (B, C) without a chemical gradient. Specifically, we found that the early time regimes are greatly expanded and the long-time diffusion is reduced. The latter indicates that the bacteria spend most of the time near the source. Using the same analysis as above, we found $D_0 = 48 \pm 8\,\mu\mathrm{m}^2/\mathrm{s}$ and $D_{max} = 565 \pm 9\,\mu\mathrm{m}^2/\mathrm{s}$. The latter value is ~ 3.4 times greater than measured in homogeneous TMN. Despite very different time scales in the measurements presented in Figs. 6 (B-D), we noticed that the functional forms for all of them are similar, but they are very different from *E. coli*. This similarity is due to the fact that the marine bacterium uses the same motility pattern to navigate regardless whether a chemical signal is present or not. Moreover it suggests that the swimming interval control in the marine bacterium, characterized by the dwell-time

distribution, must be similar as well in all cases.

As a comparison, we also performed the MSD measurement for RP437 in the presence of a localized serine as above. The data is displayed by the purple dots in Fig. 6 (D). The MSD displays the short-time ballistic regime and the long-time diffusive regime similar to Fig. 6 (A) when no chemical gradient is present. The overall MSD is greater in the presence of serine than in its absence as illustrated by plotting the two measurements (green and purple curves) together in Fig. 6 (E). Unlike *V. alginolyticus*' case, where the presence of the small source causes strong localization as indicated by a reduction of D_0 from its steady-state value, *E. coli* forms a loose aggregate near the small source [6]. The long-time diffusivity $D_0 = 200 \pm 9\,\mu\text{m}^2/s$ of *E. coli* actually increases by nearly a factor of two when compared to its steady-state value (see inset of Fig. 6 (F)). Observation under the microscope shows that in the neighborhood of the micropipette tip, individual *E. coli* cells swim in more-or-less straight lines, and the average swimming distance ℓ is comparable to the size of the aggregate. Since $D_0 \propto v\ell$ and the swimming speed v is essentially unaffected by serine, the increased MSD and D_0 are a result of increasing ℓ when *E. coli* cells are positively stimulated and unable to adapt quickly.

The emerging physical picture based on the above experiments is the following: (i) the basic functional forms of MSD vs. τ , or for that matter $D(\tau)$ vs. τ, is largely determined by bacterial motility patterns, and they are weakly or unaffected by the presence of chemoeffectors; (ii) the ability for a cell to localize depends critically on how fast it can response to a local environment by adaptation; and (iii) backtracking is essential for enhancing short-time diffusion while suppressing long-time diffusion. Below we will incorporate some of these features in mathematical models that allow MSD(τ) and $D(\tau)$ to be calculated and compared with the experiment.

2.2.2 Theory

In what follows we delineate the steps that allow us to calculate the MSD, $\langle \vec{r}^2(\tau) \rangle$, and the time-dependent diffusivity, $D(\tau)$, for different motility patterns. Our formulation is general enough to take into account temporal correlations between forward and backward

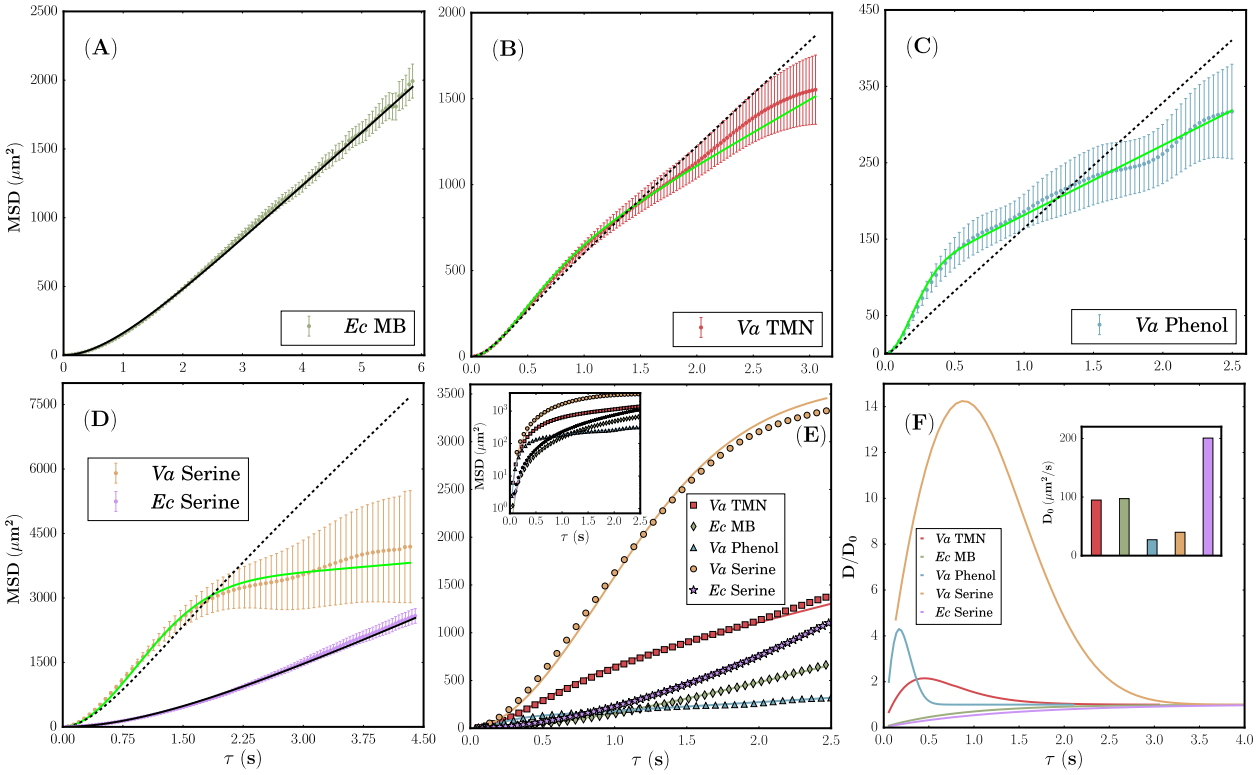

Figure 6: Mean-Squared Displacement (MSD) as a function of time τ. In (A-B), the measured MSD(τ) vs. time τ are plotted respectively for *E. coli* (green dots) and *V. alginolyticus* (red dots) in the homogeneous motility buffers. In (C) the same measurements are presented for YM4 in 10 mM of phenol. The fast motor reversals of the bacterium greatly reduces its translational motion as compared to the data in (B). In (D), MSD of YM4 in the presence of a point-like serine source; 1 mM of serine released from a micropipette tip in the background of TMN. The steady-state serine profile covers approximately a volume $\sim 20 \times 20 \times 20$ μm^3 [5]. Compared to (B-C), the positive chemical stimulus significantly alters the MSD. In all the plots, the error bars are standard errors of the means. The solid black and green lines in (A-D) are fits to the theoretical models presented in the main text. An excellent fit to the *E. coli* data using exponential distribution for the CCW intervals is demonstrated by the black lines in (A) and (D). Similarly good fits using the inverse Gaussian distributions are obtained for *V. alginolyticus* as shown by the solid green lines in (B-*D*). The experimental data for YM4 cannot be fitted by the exponential distributions as delineated by the dashed black lines. For comparisons between different measurements, all data and the fitting curves in (A-D) are replotted on the linear-linear scale in (E) and on the semi-log scale in the inset. In (F), the reduced bacterial diffusivity D/D_0 for all cases are plotted using the same colors as in (E), where different D are calculated based on the fitting curves, $D \equiv \frac{\mathrm{d}}{\mathrm{d}\tau}\mathrm{MSD}(\tau)/4$, and D_0 are their corresponding asymptotic values.

intervals and arbitrary dwell-time distributions for these intervals. We start by calculating the velocity-velocity autocorrelation $F(\tau) \equiv \langle \vec{v}(t) \cdot \vec{v}(t+\tau) \rangle / d$, where the angular brackets indicate both the time and the angular average, and d indicates the spatial dimension [28, 29]. In our experiment, since only those bacteria that swim more-or-less in the focal plane of the microscope were included in our ensemble we will treat the problem as two-dimensional, $d = 2$. It follows,

$$F(\tau) \equiv \frac{1}{2dT} \int_{-T}^{T} \mathrm{d}t \frac{1}{2\pi} \int_{2\pi} \mathrm{d}\Omega \, \vec{v}(t) \cdot \vec{v}(t+\tau) = \frac{1}{2dT} \int_{-T}^{T} \mathrm{d}t \overline{\vec{v}(t) \cdot \vec{v}(t+\tau)}, \tag{2.1}$$

where the over-bar stands for the angular average. Ignoring thermal fluctuations, one expects that for τ less than one swimming cycle $\Delta_f + \Delta_b$, $\vec{v}(t)$ and $\vec{v}(t+\tau)$ are completely correlated, but for τ greater than $\Delta_f + \Delta_b$, they are uncorrelated, or $\overline{\vec{v}(t) \cdot \vec{v}(t+\tau)} = 0$. This stems from the fact that after a flick, the new swimming direction, specified by $\vec{v}_f$, is completely randomized [6]. This approximation is reasonable since the rotational-diffusion time ($3-4\,\mathrm{s}$) is longer than $\langle \Delta_f \rangle + \langle \Delta_b \rangle \simeq 1\,\mathrm{s}$, and direction randomization is essentially carried out by the flick at the end of the backward interval [6]. The above analysis motivates us to break the time integration into a sum of individual swimming cycles indexed by $i = 1, 2, ...M$ for a given trajectory,

$$F(\tau) = \frac{1}{\left(\langle \Delta_f \rangle + \langle \Delta_b \rangle\right) M d} \sum_{i=1}^{M} \int_{0}^{(\Delta_f + \Delta_b)_i} \mathrm{d}t \, \overline{\vec{v}_i(t) \cdot \vec{v}_i(t+\tau)}, \tag{2.2}$$

where $\vec{v}_i(t) \cdot \vec{v}_i(t+\tau)$ is the inner product of the velocity pair in the ith cycle, and $M \simeq 2T / \left(\langle \Delta_f \rangle + \langle \Delta_b \rangle\right)$. The autocorrelation within a swimming cycle itself is a random variable, which, aside from being a function of t and τ, depends on the swimming intervals Δ_f and Δ_b. Thus, the sum in Eq. 2.2 can be viewed as the average over the intervals Δ_f and Δ_b,

$$\frac{1}{M} \sum ... = \int_{0}^{\infty} \mathrm{d}\Delta_f P_f(\Delta_f) \int_{0}^{\infty} \mathrm{d}\Delta_b P_b(\Delta_b) .... \tag{2.3}$$

As an exercise, let's examine the simpler case of *E. coli* swimming, which can be classified as a 2-step swimmer. It is known that for *E. coli* both CCW (run) and CW (tumble) interval distributions are exponential, but since CCW interval is about ten times as long as the CW

interval [30], the latter may be ignored. In this case the only meaningful correlation is when $\Delta_{ccw} > \tau$ and $\Delta_{ccw} \geq t + \tau$. Putting these conditions as a constraint, we have

$$\overline{\vec{v}_i(t) \cdot \vec{v}_i(t+\tau)} = v_{ccw}^2 H(\Delta_{ccw} - \tau) H(\Delta_{ccw} - t - \tau), \tag{2.4}$$

where v_{ccw} is the swimming velocity of the bacterium, and $H(t)$ is the Heaviside function. Using Eq. 2.4, we find,

$$\int_0^{\Delta_{ccw}} \mathrm{d}t\, \overline{\vec{v}_i(t) \cdot \vec{v}_i(t+\tau)} = v_{ccw}^2 (\Delta_{ccw} - \tau) H(\Delta_{ccw} - \tau). \tag{2.5}$$

Note that the more general case can be derived using the result of a 3-step swimmer (see below) by setting $v_{cw} = 0$ but keeping $\tau_{cw} (\equiv \langle \Delta_{cw} \rangle)$ finite. Using $P_{ccw}(\Delta_{ccw}) = \exp(-\Delta_{ccw}/\tau_{ccw})/\tau_{ccw}$ and integrating over all possible Δ_{ccw}, we arrive at the velocity-velocity autocorrelation function for *E. coli*,

$$F(\tau) = \frac{v_{ccw}^2 \phi_{ccw}}{d} \exp\left(-\frac{\tau}{\tau_{ccw}}\right), \tag{2.6}$$

where $\phi_{ccw} = \tau_{ccw}/(\tau_{ccw} + \tau_{cw})$ is the CCW bias. It follows from Appendix A, the time dependent bacterial diffusivity for *E. coli* is given by,

$$D_2(\tau) = \int_0^{\tau} F(\tau')\, \mathrm{d}\tau' = \frac{v_{ccw}^2 \tau_{ccw}}{d} \phi_{ccw} \left[1 - \exp\left(-\frac{\tau}{\tau_{ccw}}\right)\right]. \tag{2.7}$$

This shows that for short times $\tau/\tau_{ccw} \ll 1$, bacterial diffusivity is $D_2(\tau) \simeq D_{02}\tau/\tau_{ccw}$, and for long times $\tau/\tau_{ccw} \gg 1$, $D_2 \to D_{02} = \frac{v_{ccw}^2 \tau_{ccw}}{d} \phi_{ccw}$, where the subscript 2 stands for the 2-step swimmer. We note that for this type of bacteria, $D_2(\tau)$ approaches the long-time behavior monotonically, $A_2(\tau)\,(\equiv D_2(\tau)/D_{02}) = 1 - \exp(-\tau/\tau_{ccw})$, indicating that the maximum diffusivity D_{max} is reached only when $\tau \to \infty$. Using the velocity-velocity autocorrelation function we are also able to calculate *E. coli*'s MSD (see Appendix A),

$$\begin{aligned} \langle \vec{r}(\tau)^2 \rangle &= 2d \int_0^{\tau} \mathrm{d}\tau' (\tau - \tau') F(\tau') \\ &= 2 v_{ccw}^2 \tau_{ccw}^2 \phi_{ccw} \left[\frac{\tau}{\tau_{ccw}} - 1 + \exp\left(-\frac{\tau}{\tau_{ccw}}\right)\right]. \end{aligned} \tag{2.8}$$

Equation 2.8 yields the expected ballistic motion $\langle \vec{r}(\tau)^2 \rangle \to v_{ccw}^2 \phi_{ccw} \tau^2$ for $\tau/\tau_{ccw} \ll 1$, and the diffusive motion $\langle \vec{r}(\tau)^2 \rangle \to 2dD_{02}\tau$ for $\tau/\tau_{ccw} \gg 1$. As shown in Fig. 6 (A), this equation fits remarkably well to the experimental data despite the approximation $\tau_{cw} = 0$ made.

The calculation for 3-step swimmers is more tedious, and we leave the details to Appendix B. Despite the complication, for interval distributions that are exponential functions and uncorrelated between swimming cycles, the velocity-velocity autocorrelation can still be calculated analytically with the result,

$$\begin{aligned} F(\tau) = \frac{1}{d(\tau_f^2 - \tau_b^2)} \Big[& v_f^2 \tau_f \left(\tau_f - \tau_b\right) \exp(-\frac{\tau}{\tau_f}) \\ & + v_b^2 \tau_b \left(\tau_f - \tau_b\right) \exp(-\frac{\tau}{\tau_b}) - v_f v_b \tau_f \tau_b \left(\exp(-\frac{\tau}{\tau_f}) - \exp(-\frac{\tau}{\tau_b}) \right) \Big] . \end{aligned} \tag{2.9}$$

It should be noted that in the limit $v_b \to 0$, this equation converges to the 2-step case as it should be. Using Eq. 2.9, we obtained the time dependent bacterial diffusivity for the 3-step swimmer,

$$\begin{aligned} D_3(\tau) = \frac{1}{d(\tau_f^2 - \tau_b^2)} \big[& v_f \tau_f^2 \left(v_f(\tau_f - \tau_b) - v_b \tau_b \right) G_f(\tau) \\ & + v_b \tau_b^2 \left(v_b(\tau_f - \tau_b) + v_f \tau_f \right) G_b(\tau) \big] , \end{aligned} \tag{2.10}$$

where $G_x(\tau) \equiv 1 - \exp(-\tau/\tau_x)$ with $x = (f, b)$. In our experiment, since τ_f is somewhat greater than τ_b, $G_f(\tau)$ relaxes slower than $G_b(\tau)$. Moreover, since the amplitude of $G_f(\tau)$ is negative and the amplitude of $G_b(\tau)$ is positive, it follows that $D_3(\tau)$ peaks at a finite τ before leveling off to a constant value $D_{03} = \left((v_f \tau_f - v_b \tau_b)^2 + v_f v_b \tau_f \tau_b \right) / d(\tau_f + \tau_b) = \frac{v_f^2 \tau_f}{d} \phi_f \left((1 - \alpha\beta)^2 + \alpha\beta \right)$ in long times, where $\phi_f = \tau_f/(\tau_f + \tau_b)$, $\alpha = v_b/v_f$, and $\beta = \tau_b/\tau_f$. We note that for a symmetric 3-step swimmer, i.e., $\alpha = \beta \to 1$, D_{03} attains a simple form $D_{03} = \frac{v_f^2 \tau_f}{d} \phi_f$ that is identical to the 2-step counterpart with $D_{02} = \frac{v_{ccw}^2 \tau_{ccw}}{d} \phi_{ccw}$. This suggests that if hypothetical 2-step and 3-step (symmetric) swimmers are constructed such that they are identical in all aspects, i.e. $v_{ccw} = v_f = v_b$ and $\tau_{ccw} = \tau_f = \tau_b$, with the only exception that their motility patterns is different, $D_{03} = D_{02}/2$, where $\phi_{ccw} \simeq 1$ (since $\tau_{cw} \ll \tau_{ccw}$) and $\phi_f = 1/2$. In a more realistic situation when $\phi_{ccw} \simeq 90\%$, the above conclusion is still qualitatively valid. This implies that the hypothetical 3-step swimmer can localize better near a small source than its 2-step counterpart [24]. To attain a minimal diffusivity in long times, the 3-step swimmer can coordinate its forward and backward movements in such

a way $\alpha\beta = 0.5$, which leads to $(D_{03})_{min} = \frac{3}{4}\frac{v_f^2\tau_f}{d}\phi_f$, where ϕ_f is assumed to be approximately a constant. The existence of such minimum diffusion is illustrated in the inset of Fig. 7.

To characterize how $D_3(t)$ approaches its steady-state value, we define $A_3(\tau)$ similarly to the 2-step case,

$$A_3(\tau)\left(\equiv\frac{D_3(\tau)}{D_{03}}\right)=\frac{v_f\tau_f^2\left(v_f(\tau_f-\tau_b)-v_b\tau_b\right)G_f(\tau)+v_b\tau_b^2\left(v_b(\tau_f-\tau_b)+v_f\tau_f\right)G_b(\tau)}{(\tau_f-\tau_b)\left((v_f\tau_f-v_b\tau_b)^2+v_fv_b\tau_f\tau_b\right)}. \tag{2.11}$$

This function is significantly different from $A_2(\tau)$ and will be discussed shortly. To compare with our experimental measurements, we also calculate MSD by integrating $D(t)$ one more time, yielding

$$\begin{aligned}\langle\vec{r}(\tau)^2\rangle &= 2d\int_0^\tau \mathrm{d}\tau' D(\tau')\\ &= \frac{2}{\tau_f^2-\tau_b^2}\left[v_f\tau_f^3\left(v_f(\tau_f-\tau_b)-v_b\tau_b\right)\Phi_f(\tau)\right.\\ &\quad\left.+v_b\tau_b^3\left(v_b(\tau_f-\tau_b)+v_f\tau_f\right)\Phi_b(\tau)\right],\end{aligned} \tag{2.12}$$

where $\Phi_x(\tau)\equiv\frac{\tau}{\tau_x}-1+\exp\left(-\frac{\tau}{\tau_x}\right)$ with $x=(f,\,b)$. The equation is somewhat simplified with $\langle\vec{r}(\tau)^2\rangle=\tau_0^2\left((v_f-v_b)^2\Phi_0(\tau)+v_fv_b\frac{\tau}{\tau_0}\left(1-\exp\left(-\frac{\tau}{\tau_0}\right)\right)\right)$ when $\tau_f\to\tau_b=\tau_0$, and it gives the correct long-time limit $\langle\vec{r}(\tau)^2\rangle=v_0^2\tau_0\tau$ when $v_f\to v_b=v_0$.

A major difference between the 2-step and 3-step bacterial chemotaxis is that while $D(\tau)$ increases monotonically with τ for the former, it does not for the latter. Figure 7 displays reduced diffusivity $A_2(\tau)$ and $A_3(\tau)$, and it shows that A_3 is peaked when forward and backward swimming behaves similarly with $v_f\simeq v_b$ and $\tau_f\simeq\tau_b$. The peaking in $D(\tau)$ is a result of backtracking, and our observation shows that the more statistically similar the two intervals are, the higher the peak is. Biologically, the backtracking may be interpreted as a microorganism's means of explorative-exploitative behavior in chemotaxis. In essence, it allows the microorganism to overshoot a target in searching for a greener pasture, but if this fails it can backtrack, returning to the original position. When nutrients are sparsely distributed and subject to convective mixing, this (run-reverse-flick) chemotactic strategy can be more effective than the run-tumble strategy in searching for the nutrients (see Conclusion). The quantity $A(\tau)$ defined above therefore provides a quantitative measure of a microorganism's potential for chemotaxis; the taller the peak or the larger D_{max} is,

the more explorative potential the microorganism has since the searching area scales as $D_{max}\tau_{max}$, where τ_{max} maximizes $D(\tau)$. And the smaller the D_0 is, the better the bacterium can localize or more exploitative. In this light, we see that the marine bacterium's motility pattern is well suited for exploration in short times and for exploitation (localization) in long times. The relative height at the peak, D_{max}/D_0, is therefore a dimensionless measure of bacterial chemotaxis potential. Using the exponential distribution for Δ_f and Δ_b, we found that the peak height never exceeds $D_{max}/D_{03} - 1 \sim 15\%$, which is inconsistent with the MSD measured in *V. alginolyticus*. Indeed using Eq. 2.12, we found that the theoretically predicted form hardly fits the experimental data (dashed black lines in Figs. 6 (B-D)). As we shall see below by employing a non-Poissonian motor regulation, D_{max}/D_0 can be significantly increased, and it agrees much better with our experiments.

Failure in the above fitting procedure suggests that the Poisson process for motor regulation is not stringent enough to enforce backtracking. Indeed, we found that *V. alginolyticus* regulates its motor switch by a non-Poisson process [6], and such behavior has been seen in other bacteria as well [31]. As will be shown below, for *V. alginolyticus* the swimming intervals can be described satisfactorily by the inverse Gaussian distribution,

$$P_x(\Delta_x) \equiv \left(\frac{\tau_{Dx}}{2\pi\Delta_x^3}\right)^{1/2} \exp\left[-\frac{\left(1-\Delta_x/\tau_{Px}\right)^2}{2\left(\Delta_x/\tau_{Dx}\right)}\right], \tag{2.13}$$

where $x = (f, b)$. To put this model in perspective, we note that this distribution is the solution of the first-passage problem of a dispersion wave that propagates in a one-dimensional domain of size L, and it may mimic the conformational spread of the flagellar motor switch of the marine bacterium [32]. For a wave packet that travels with velocity V_w and broadens with a diffusivity D_w, the relevant time scales in Eq. 2.13 are given by $\tau_P = L/V_w$ and $\tau_D = L^2/2D_w$. Thus, if the conformational spread in the motor switch has a low dispersion, i.e. a small D_w, the diffusion time τ_D will be large and correspondingly a narrow $P_x(\Delta_x)$. For convenience of a later discussion, it is useful to delineate some mathematical features of Eq. 2.13: First, the distribution is peaked at $\Delta_{max} = (\tau_P/2)\left(\sqrt{(3\gamma)^2+4} - 3\gamma\right)$, and it has the mean $\langle\Delta\rangle = \tau_P$ and the standard deviation $\sigma_\Delta = \gamma^{1/2}\tau_P$, where $\gamma = \tau_P/\tau_D$. Second, for small times, $\Delta \ll \tau_P$, the distribution cuts off sharply as $\sim \exp(-\tau_D/(2\Delta))$ and for large times, $\Delta \gg \tau_P$, the distribution is approximately exponential, $\sim \exp(-\tau_D\Delta/(2\tau_P^2))$. Hence,

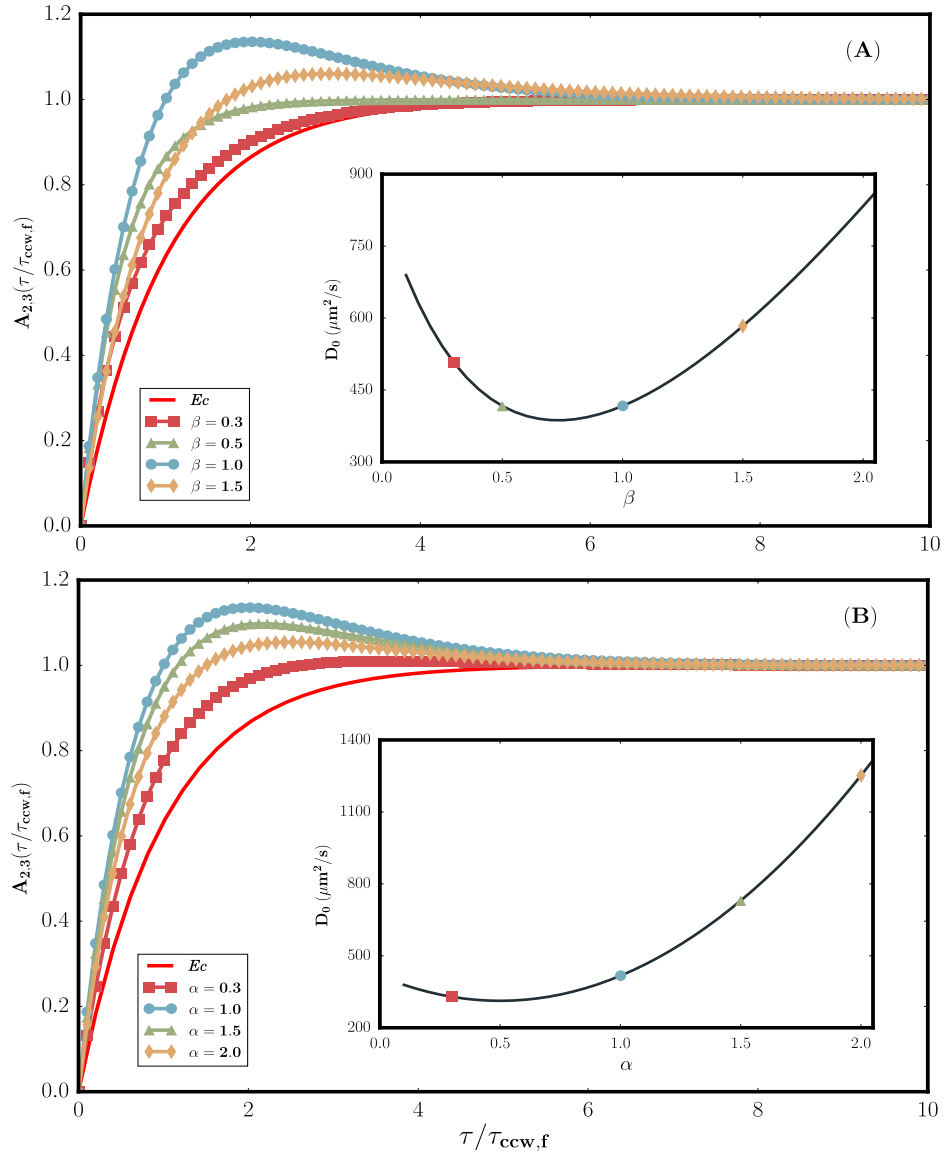

Figure 7: Normalized time-dependent diffusivity $A_{2,3}(\tau) \equiv D_{2,3}/D_0$ calculated using the exponentially distributed dwell-time distributions. The bacterial motor switches in these plots are assumed to be governed by a Poisson process. The solid red lines in both (A) and (B) are for the 2-step swimmer or *E. coli* (Ec). It shows that $A_2(\tau/\tau_{ccw})$ is a monotonically increasing function of time τ, and it eventually levels off to unity. The other colored lines in (A) and (B) are for the 3-step swimmer or *V. alginolyticus*. In (A), $\alpha = v_b/v_f = 1$ is fixed but $\beta = \tau_b/\tau_f$ is varied from 0.3-1.5. As can be seen, $A_3(\tau/\tau_f)$ has a peak, and it attains its maximum value when $\beta \simeq 1$. In (B), $\beta = 1$ is fixed but α is varied from 0.3-2. Again, we found that the maximum peak occurs at $\alpha \simeq 1$. The long-time diffusion coefficients D_0 are plotted in the insets for different values of β (A) and α (B), where colored symbols correspond to the $A_3(\tau/\tau_f)$ vs. τ/τ_f curves in the main figures. It is seen that D_0 attains its minimal value when $\alpha = 1$ and $\beta \simeq 0.5$, corresponding to $v_b = v_f$ and $\tau_f \simeq 2\tau_b$ in (A), or when $\alpha = 0.5$ and $\beta = 1$, corresponding to $v_f = 2v_b$ and $\tau_f = \tau_b$ in (B). We note that for wild-type (wt) *V. alginolyticus* YM4 and without chemical stimulation, $v_f/v_b \simeq 0.9$ and $\tau_f/\tau_b \simeq 1$, indicating that swimming of *V. alginolyticus* is approximately symmetric in the forward and backward directions, and the bacterial diffusivity is close but not equal to the minimum value of D_0.

the short-time inhibition of motor switching sets this distribution apart from the exponential ones [6].

We calculated numerically $D_3(\tau)$ for different parameters τ_{Pf}, τ_{Pb}, τ_{Df}, and τ_{Db}, and the results are displayed in Fig. 8. For simplicity, v_f and v_b are assumed to be identical and are set at $v_0 = 50\,\mu$m/s. We furthermore keep the time scale associated with the forward interval fixed, $\tau_{Pf} = 0.5\,$s and $\tau_{Df} = 1.5\,$s, and only varied the time scale associated with the backward interval, τ_{Pb} and τ_{Db}. Specifically, by keeping $\tau_{Db} = 1.5\,$s fixed, in Fig. 8 (A) we examine how a change in τ_{Pb} affects $A_3(\tau)$. We found that $A_3(\tau)$ is a monotonically increasing function of τ for $\tau_{Pb} \ll \tau_{Pf}$, but becomes peaked when τ_{Pb} is comparable to τ_{Pf}. Also as shown in the inset, in the neighborhood of τ_{Pf}, the long-time diffusivity D_0 is a concave function of τ_{Pb}, indicating that to localize near a source the mean dwell times, $\langle\Delta_f\rangle \equiv \tau_{Pf}$ and $\langle\Delta_b\rangle \equiv \tau_{Pb}$, have to be coordinated. Likewise, by keeping $\tau_{Pb} = 0.5\,$s fixed, in Fig. 8 (B) we examine how τ_{Db}, which determines the dispersion of the dwell-time distribution, affects $A_3(\tau)$. Here we again found that for small $\tau_{Db}(\ll \tau_{Pb}= 0.5\,$s), or a large dispersion, $A_3(\tau)$ increases monotonically with τ. A peak develops only when τ_{Db} becomes comparable to τ_{Pb}. Moreover, the peak height grows rapidly as τ_{Db} becomes large, and it is accompanied by a relatively slow decrease in D_0 (see the inset), indicating that in order to localize, the dispersion in the dwell-time distribution needs to be small. As shown by the thin red lines in Fig. 8 (A,B), wt *V. alginolyticus* YM4 in TMN operates at a nearly optimal parameter range as indicated by their prominent peaks.

The above analysis shows that by introducing the non-Poissonian switching process, the peaks in $D_3(\tau)$ are much more pronounced than those generated by the Poisson process. In fact if one sets $\tau_{Pf} \simeq \tau_{Pb}$ and reduces the dispersion by letting $\tau_{Pf}/\tau_{Df} \simeq \tau_{Pb}/\tau_{Db} \ll 1$, the dimensionless peak height D_{max}/D_{03} can be arbitrarily large. The large range by which the peak height of $D_3(\tau)$ can be tuned by varying τ_{Pf} and τ_{Pb} provides an opportunity for robust adaptation of a microorganism to different environments.

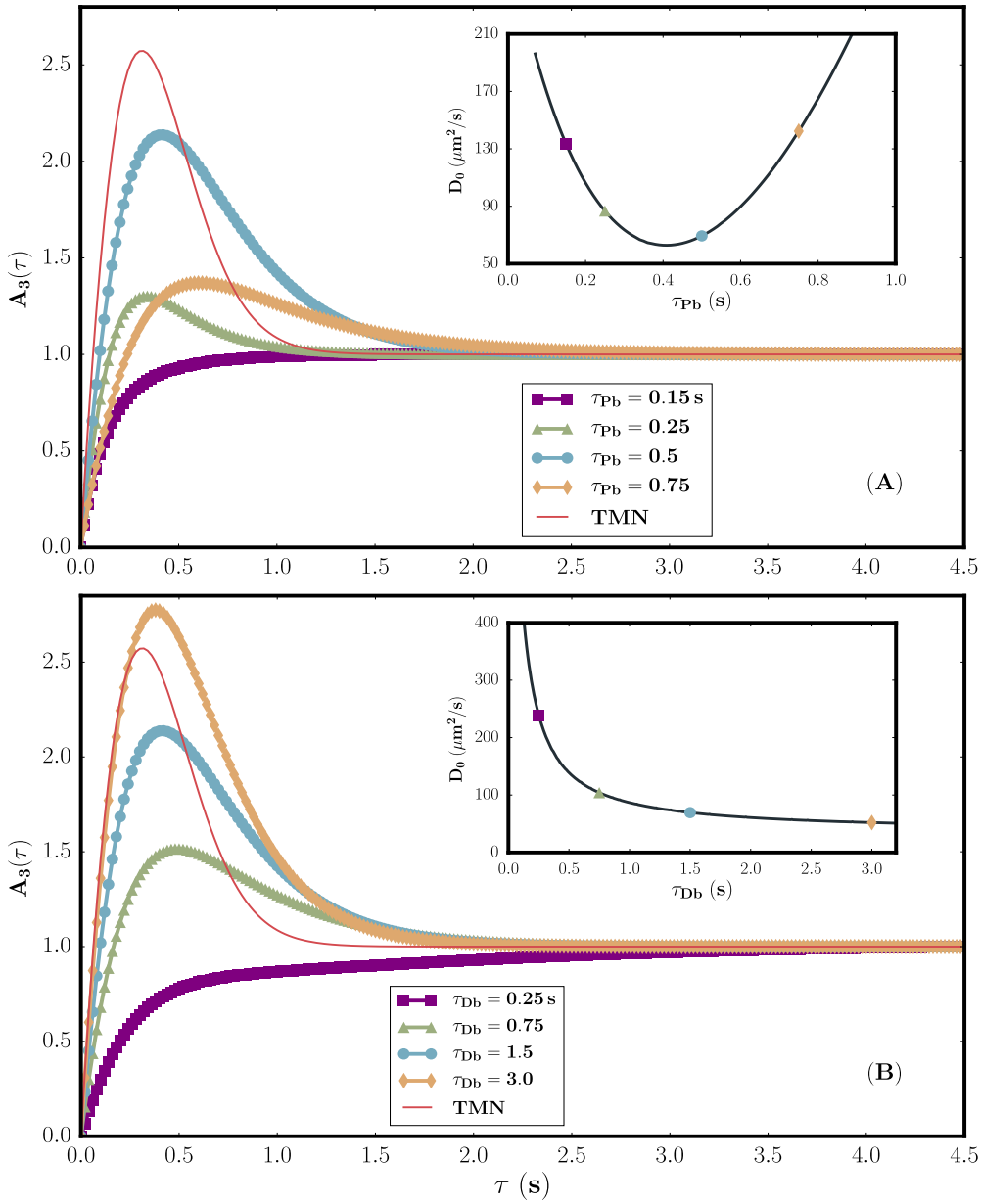

Figure 8: Normalized time-dependent diffusivity $A_3(\tau) \equiv D_3(\tau)/D_0$ normalized time-dependent diffusivity $A_3(\tau) \equiv D_3(\tau)/D_0$ calculated using the inverse-Gaussian distribution: (A) $v_f = v_b = 50\,\mu$m/s, $\tau_{Df} = \tau_{Db} = 1.5$ s, and $\tau_{Pf} = 0.5$ s are fixed, but τ_{Pb} is varied with $\tau_{Pb} = 0.15$ (purple squares), 0.25 (green triangles), 0.5 (blue circles), 0.75 s (brown diamonds). The inset is the plot of D_0 vs. τ_{Pb}. (B) $v_f = v_b = 50\,\mu$m/s, $\tau_{Pf} = \tau_{Pb} = 0.5$ s, and $\tau_{Df} = 1.5$ s are fixed, but τ_{Db} is varied with $\tau_{Db} = 0.25$ (purple squares), 0.75 (green triangles), 1.5 (blue circles), and 3 s (brown diamonds). The inset is the plot of D_0 vs. τ_{Db}. The thin red lines in (A) and (B) are calculated based on the observation of YM4 in TMN buffer. The colored symbols in the insets match those in the main figures.

2.2.3 Interpretation of experimental observations

Using numerical integration, we are able to perform non-linear least square fits to our measured MSDs for YM4, which are displayed in Figs. 6 (B-D). As can be seen by the solid green lines, the quality of these fits is good, much better than when the exponential distributions (dashed black lines) were used. For convenience, the fitting results for the three cases are detailed in Table 1. We noticed that when phenol, to which *V. alginolyticus* cannot adapt, is present in TMN, the average time in a swimming cycle, $\langle\Delta_f\rangle+\langle\Delta_b\rangle$, becomes shorter and the reduction is mainly in the backward intervals. The situation is different when a point source of serine is present. In this case, the mean time in a swimming cycle increases significantly from 1.2 s to 2.8 s, and the increment is contributed by both forward $\langle\Delta_f\rangle$ and backward $\langle\Delta_b\rangle$ intervals. Most interestingly the forward and backward swimming intervals become more symmetrical $\langle\Delta_f\rangle \simeq \langle\Delta_b\rangle$, and the interval time dispersion is significantly reduced, from $\sigma_{\Delta_f}/\langle\Delta_f\rangle \simeq \sigma_{\Delta_b}/\langle\Delta_b\rangle \simeq 0.55$ when no serine is present to ~ 0.2 when it is present. This indicates that around a small patch of chemoattractant, the marine bacterium does not differentiate forward and backward swimming directions, and the cell is strongly localized; or in other words, the net displacement in a swimming interval, $\ell\,(\equiv v_f\Delta_f - v_b\Delta_b)$, is small.

We also noticed that our fitting results are consistent with our previous findings [6]. Specifically, in our previous experiment for YM4 in TMN, $\langle\Delta_f\rangle \simeq 0.4$ s and $\langle\Delta_b\rangle \simeq 0.5$ s. Both are in reasonable agreement with the corresponding values in Table 1. For a more stringent check, we determined the swimming intervals of those bacterial trajectories that were used for calculating the MSD in Fig. 6 (B). Altogether there are 354 forward and 418 backward intervals, and they allow us to construct the dwell-time PDFs, which are displayed in Fig. 9. As delineated by the pink lines, these PDFs can be adequately described by the inverse Gaussian distribution (Eq. 2.13), and the fitting procedure yields $\tau_{Pf} = 0.56 \pm 0.02$ s, $\tau_{Df} = 1.5\,^{+0.5}_{-0.1}$ s, $\tau_{Pb} = 0.53\,^{+0.06}_{-0.02}$ s, and $\tau_{Db} = 2.3 \pm 0.4$ s. These parameters are not identical to those obtained by fitting the MSD data in Fig. 6 (B) (see Table 1), but they are sufficiently close as judged by the χ^2 [33] analysis presented in Fig. 9 (C). Here, the red dot represents the best fits to $P(\Delta_f)$ and $P(\Delta_b)$. Its value, $\chi^2 \simeq 0.85$, is sufficiently close to unity, indicating that (i) the uncertainties in the measurements are correctly presented and (ii) the inverse

Gaussian distribution is appropriate for the PDFs. In generating the surface plot in the figure, we fixed $\tau_{Df} = 1.5\,\mathrm{s}$ and $\tau_{Db} = 2.3\,\mathrm{s}$, since they are less sensitive in the nonlinear regression, and varied the remaining parameters τ_{Pf} and τ_{Pb}. The constant contours in the plot correspond to integer multiple of the standard deviation $n\sigma$. Using the parameters $\tau_{Pf} = 0.59\,\mathrm{s}$ and $\tau_{Pb} = 0.56\,\mathrm{s}$ from fitting to the MSD data, we also evaluated χ^2 and plotted the point ($\chi^2 \simeq 1.0$) as the yellow dot in Fig. 9 (C). As shown the two χ^2 values are well within one standard deviation, and it gives us much confidence that our model has captured essential features of bacterial diffusivity in *V. alginolyticus.*

Finally, it is useful to compare our measurements for different bacteria and under different chemical conditions. In Fig. 6 (E) we plotted the MSD data along with their fitting curves for the five studied cases. It shows that while MSD increases slowly but steadily with time for *E. coli* (green and purple curves), the same quantity increases rapidly and appears to level off in long times for *V. alginolyticus* (red, blue, and brown curves). To view the earlier behavior more clearly, the same set of data is also plotted on the semi-logarithmic scale in the inset. The most striking feature is when $D(\tau)/D_0$ is calculated based on the fitting curves by taking its time derivative as displayed in Fig. 6 (F). One observes that while the *E. coli* (green and purple) curves are monotonic in time, the curves for *V. alginolyticus* (red, blue, and brown) are strongly peaked. Interestingly, the peak height $(D/D_0)_{max}$ depends on the environment: when no chemoeffector is present (red), $(D/D_0)_{max} \simeq 2.1$ but when it is present $(D/D_0)_{max}$ increases remarkably, e.g. 4.3 for phenol (blue) and 14 for serine (brown). Moreover, the localized chemoattractant (serine) not only induces a taller peak, it also causes the peak to broaden considerably and move to a large time. This remarkable behavior indicates that the marine bacterium makes long excursions but the net displacement ℓ in a swimming cycle (forward+backward) is small due to backtracking.

2.3 CONCLUSION

It is generally expected that the ability for a bacterium to localize comes at a cost of lowering its explorative potential. When we first observed that the marine bacterium *V. alginolyticus*'

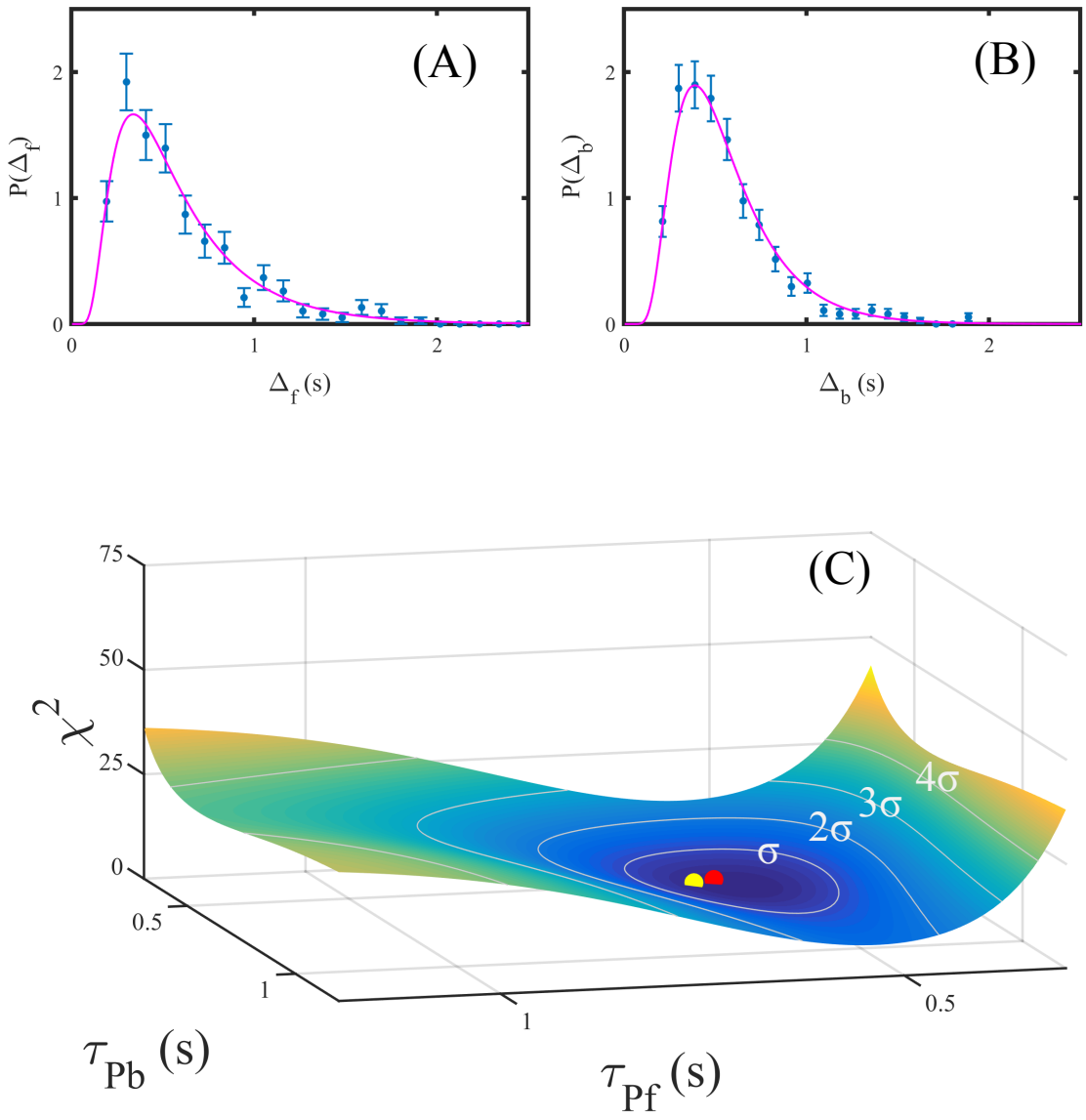

Figure 9: Dwell-time PDFs of YM4 in TMN. In (A) and (B), the blue dots represent the measured forward and backward swimming interval distributions, $P(\Delta_f)$ and $P(\Delta_b)$. These dwell-time intervals were collected from the bacterial trajectories that were used for calculating MSD in Fig. 6 (B). The pink lines are fits using the inverse Gaussian distribution, Eq. 2.13. The quality of the fit is presented in (C), where χ^2 is plotted against two sensitive parameters, τ_{Pb} and τ_{Pf}, in the inverse Gaussain distribution. The red dot with $\chi^2 \simeq 0.85$ is located at the valley of the χ^2 plot, representing the optimal fit to the dwell-time PDFs in (A-B), and the yellow dot represents the optimal fit to the MSD data in Fig. 6 (B). The constant contours correspond to integer multiple of the standard deviation σ.

	$\langle\Delta_f\rangle \equiv \tau_{Pf}$ (s)	τ_{Df} (s)	σ_{Δ_f} (s)	$\langle\Delta_b\rangle \equiv \tau_{Pb}$ (s)	τ_{Db} (s)	σ_{Δ_b} (s)
TMN	0.59 ± 0.03	1.5 ± 0.9	0.37	0.56± 0.03	2.3 ± 0.9	0.28
10 mM phenol	0.34 ± 0.01	5.2 ± 0.9	0.09	0.22 ± 0.01	8.5 ± 0.9	0.04
1 mM serine	1.4 ± 0.1	30 ± 9	0.29	1.4 ± 0.1	28 ± 9	0.32

Table 1: Fitting parameters for the inverse Gaussian dwell time distribution for *V. alginolyticus* YM4. Using the MSD data in Figs. 6 (B-D), which correspond to YM4 in uniform TMN, in TMN supplemented with phenol, and near a point source of serine in TMN, a non-linear least square fitting routine is conducted. The fitting results are displayed by the green lines in Figs. 6 (B-D) and in the table above.

motor switch is not regulated in a Poissonian fashion, it was a surprise as well as a big puzzle [6]. Here we believe that we may have the answer: The short-time inhibition of the flagellar motor switch can significantly improve the bacterium's explorative behavior by increasing its search radius in short times. This gives rise to a large peak D_{max} in the time-dependent diffusivity $D(\tau)$. However, if a search turns out to be in the wrong direction, the backtracking can readily bring the bacterium back to its more favorable location. By canceling out the advance made in the searching step, the backtracking step is exploitative and can significantly reduce the net displacement ℓ in a swimming cycle. This gives rise to a small D_0, which is the long-time limit of $D(\tau)$. The dimensionless ratio, D_{max}/D_0, therefore provides a simple, quantitative measure of a bacterium's ability for chemotaxis.

In an ocean environment, inhomogeneities of nutrients are created and dispersed rapidly by ocean currents. The distribution of these inhomogeneities obeys the law of turbulent mixing and is typically in the forms of small patches and fine striations. To follow and become localized near these spatial structures could be a major problem for marine bacteria, and our experiment provides a close glimpse of how one of them, *V. alginolyticus*, deals with such challenge. When the environment is homogeneous, the bacterium has a typical motor switching time of $\sim 0.5\,\mathrm{s}$, suggesting that it cannot cover a large area. However, when a chemical cue is present, it can swim over a large distance and can backtrack to localize when

the source is small. In comparison, enteric bacterium *E. coli* fares much worse under the same environment due to its long adaptation time and inability to backtrack.

2.4 APPENDIXES

2.4.1 Appendix A: The relationship between MSD and the velocity autocorrelation function

Relationship Between Velocity-Velocity Autocorrelation Function $F(t)$, Time-Dependent Diffusivity $D(t)$, and Mean-Squared Displacement $\langle \vec{r}(t)^2 \rangle$. Since $\vec{r}(\tau) = \int_0^\tau \vec{v}(t')\,\mathrm{d}t'$, the mean-squared displacement is given by,

$$\langle \vec{r}(\tau)^2 \rangle \equiv \int_0^\tau \mathrm{d}t'' \int_0^\tau \mathrm{d}t' \langle \vec{v}(t'') \cdot \vec{v}(t') \rangle = d \int_0^\tau \mathrm{d}t'' \int_0^\tau \mathrm{d}t' F(t'' - t'), \tag{2.14}$$

where d indicates the spatial dimension, and $F(t)$ defines the one-dimensional velocity-velocity auto-correlation function,

$$F(t'' - t') = \frac{1}{d} \langle \vec{v}(t'') \cdot \vec{v}(t') \rangle. \tag{2.15}$$

Because of the symmetry in t' and t'', it is expected that $F(t'' - t') = F(t' - t'')$ or in other words, the time difference should be $|t'' - t'|$. This allows us to rewrite the integration in Eq. 2.14,

$$\langle \vec{r}(\tau)^2 \rangle = d \int_0^\tau \mathrm{d}t'' \int_0^{t''} \mathrm{d}t' F(t'' - t') = 2d \int_0^\tau \mathrm{d}t'' \int_0^{t'} \mathrm{d}t' F(t'). \tag{2.16}$$

Finally, integration by parts yields,

$$\langle \vec{r}(\tau)^2 \rangle = 2d \int_0^\tau \mathrm{d}t' (\tau - t') F(t'). \tag{2.17}$$

Useful physical information can be extracted from this equation. First of all, if the mean-squared displacement is found experimentally, its time derivative immediately gives the time-dependent diffusivity,

$$D(\tau) = \frac{1}{2d} \frac{\mathrm{d}}{\mathrm{d}\tau} \langle \vec{r}(\tau)^2 \rangle. \tag{2.18}$$

Second, if the velocity-velocity autocorrelation function $F(\tau)$ is known, by calculation or by measurements, the diffusivity can be obtained by integration in time,

$$D(\tau) = \int_0^\tau \mathrm{d}t' F(t'), \tag{2.19}$$

which yields the long-time diffusion constant D_0 when $\tau \to \infty$.

2.4.2 Appendix B: Velocity autocorrelation functions resulting from exponential and inverse Gaussian distributions

For a given τ, there are four possibilities that are relevant for the calculation. These possibilities along with the velocity-velocity autocorrelation functions $\overline{\vec{v}_i(t) \cdot \vec{v}_i(t+\tau)}$ for a given ith swimming interval are given as follows:

(i) $\Delta_f \geq \tau$ and $\Delta_b \geq \tau$:

$$H(\Delta_f - \tau)H(\Delta_b - \tau)\left[v_f^2 H(\Delta_f - t - \tau) - v_f v_b H(t + \tau - \Delta_f)H(\Delta_f - t) + v_b^2 H(t - \Delta_f)H(\Delta_f + \Delta_b - t - \tau)\right];$$

(ii) $\Delta_f \geq \tau$ and $\Delta_b \leq \tau$:

$$H(\Delta_f - \tau)H(\tau - \Delta_b)\left[v_f^2 H(\Delta_f - t - \tau) - v_f v_b H(t + \tau - \Delta_f)H(\Delta_f + \Delta_b - t - \tau)\right];$$

(iii) $\Delta_f \leq \tau$ and $\Delta_b \geq \tau$:

$$H(\tau - \Delta_f)H(\Delta_b - \tau)\left[-v_f v_b H(\Delta_f - t) + v_b^2 H(t - \Delta_f)H(\Delta_f + \Delta_b - t - \tau)\right];$$

(iv) $\Delta_f \leq \tau$, $\Delta_b \leq \tau$ but $\Delta_f + \Delta_b \geq \tau$:

$$H(\tau - \Delta_f)H(\tau - \Delta_b)H(\Delta_f + \Delta_b - \tau)\left[-v_f v_b H(\Delta_f + \Delta_b - t - \tau)\right].$$

The possibility, $\Delta_f \leq \tau$, $\Delta_b \leq \tau$, but $\Delta_f + \Delta_b \leq \tau$, should be excluded since velocities are uncorrelated between swimming cycles, and it is consistent with the way the integral in Eq. 2.2 is broken into individual cycles.

Integrating over t, $\int_0^{\Delta_f + \Delta_b} \mathrm{d}t\, \overline{\vec{v}_i(t) \cdot \vec{v}_i(t+\tau)}$, we find that the above four possibilities give the expressions:

(i) $H(\Delta_f - \tau)H(\Delta_b - \tau)\left[v_f^2(\Delta_f - \tau) - v_f v_b \tau + v_b^2(\Delta_b - \tau)\right]$;

(ii) $H(\Delta_f - \tau)H(\tau - \Delta_b)\left[v_f^2(\Delta_f - \tau) - v_f v_b \Delta_b\right]$;

(iii) $H(\tau - \Delta_f)H(\Delta_b - \tau)\left[-v_f v_b \Delta_f + v_b^2(\Delta_b - \tau)\right]$;

(iv) $H(\tau - \Delta_f)H(\tau - \Delta_b)H(\Delta_f + \Delta_b - \tau)\left[-v_f v_b(\Delta_f + \Delta_b - \tau)\right]$.

We next perform averages for these four possibilities according to the dwell distribution functions $P(\Delta_f)$ and $P(\Delta_b)$. For simplicity we assume that $P_x(\Delta_x)$ is exponential, $P_x(\Delta_x) \equiv \frac{1}{\tau_x}\exp\left(-\frac{\Delta_x}{\tau_x}\right)$, where τ_x is the mean dwell time and $x = (f,\, b)$. For this simple case, the integration for the four possibilities can be carried out analytically with the result,

$$\begin{aligned} F_1(\tau) &= \int_\tau^\infty \mathrm{d}\Delta_f P_f(\Delta_f) \int_\tau^\infty \mathrm{d}\Delta_b P_b(\Delta_b) \left[v_f^2(\Delta_f - \tau) - v_f v_b \tau + v_b^2(\Delta_b - \tau)\right] \\ &= \exp\left[-\left(\frac{1}{\tau_f} + \frac{1}{\tau_b}\right)\tau\right]\left(v_f^2\tau_f + v_b^2\tau_b - v_f v_b \tau\right), \end{aligned} \tag{2.20}$$

$$\begin{aligned} F_2(\tau) &= \int_\tau^\infty \mathrm{d}\Delta_f P_f(\Delta_f) \int_0^\tau \mathrm{d}\Delta_b P_b(\Delta_b) \left[v_f^2(\Delta_f - \tau) - v_f v_b \Delta_b\right] \\ &= \exp\left[-\left(\frac{1}{\tau_f} + \frac{1}{\tau_b}\right)\tau\right] v_f \left[v_b\left(\tau - \tau_b\left(\exp\left(\frac{\tau}{\tau_b}\right) - 1\right)\right)\right. \\ &\quad \left. + v_f\tau_f\left(\exp\left(\frac{\tau}{\tau_b}\right) - 1\right)\right], \end{aligned} \tag{2.21}$$

$$\begin{aligned} F_3(\tau) &= \int_0^\tau \mathrm{d}\Delta_f P_f(\Delta_f) \int_\tau^\infty \mathrm{d}\Delta_b P_b(\Delta_b) \left[-v_f v_b \Delta_f + v_b^2\left(\Delta_b - \tau\right)\right] \\ &= \exp\left[-\left(\frac{1}{\tau_f} + \frac{1}{\tau_b}\right)\tau\right] v_b \left[v_b\tau_b\left(\exp\left(\frac{\tau}{\tau_f}\right) - 1\right)\right. \\ &\quad \left. + v_f\left(\tau - \tau_f\left(\exp\left(\frac{\tau}{\tau_f}\right) - 1\right)\right)\right], \end{aligned} \tag{2.22}$$

$$\begin{aligned} F_4(\tau) &= \int_0^\tau \mathrm{d}\Delta_f P_f(\Delta_f) \int_{\tau-\Delta_f}^\tau \mathrm{d}\Delta_b P_b(\Delta_b) \left[-v_f v_b\left(\Delta_f + \Delta_b - \tau\right)\right] \\ &= \frac{\exp\left[-\left(\frac{1}{\tau_f} + \frac{1}{\tau_b}\right)\tau\right]}{\tau_b - \tau_f} v_f v_b \left[-\tau_b\tau + \tau_b^2\left(\exp\left(\frac{\tau}{\tau_b}\right) - 1\right)\right. \\ &\quad \left. + \tau_f\left(\tau - \tau_f\left(\exp\left(\frac{\tau}{\tau_f}\right) - 1\right)\right)\right]. \end{aligned} \tag{2.23}$$

The velocity autocorrelation function is defined as,

$$\begin{aligned} F(\tau) &= \frac{1}{d(\tau_f + \tau_b)}\left[F_1(\tau) + F_2(\tau) + F_3(\tau) + F_4(\tau)\right] \\ &= \frac{1}{d(\tau_b^2 - \tau_f^2)}\exp\left[-\left(\frac{1}{\tau_f} + \frac{1}{\tau_b}\right)\tau\right]\left[v_f v_b \tau_f \tau_b\left(\exp\left(\frac{\tau}{\tau_b}\right) - \exp\left(\frac{\tau}{\tau_f}\right)\right)\right. \\ &\quad \left. + v_f^2\tau_f(\tau_b - \tau_f)\exp\left(\frac{\tau}{\tau_b}\right) + v_b^2\tau_b(\tau_b - \tau_f)\exp\left(\frac{\tau}{\tau_f}\right)\right]. \end{aligned} \tag{2.24}$$

As shown in the main text, however, the exponential distributions are inadequate to fit our experimental data. The function that fits our measured dwell-time distribution functions is the inverse-Gaussian [24],

$$P_x(\Delta_x) \equiv \left(\frac{\tau_{Dx}}{2\pi\Delta_x^3}\right)^{1/2} \exp\left[-\frac{(1-\Delta_x/\tau_{Px})^2}{2\,(\Delta_x/\tau_{Dx})}\right], \tag{2.25}$$

that exhibits short-time inhibition $P_x(\Delta_x \to 0) \to 0$ and long-time exponential decay $P_x(\Delta_x \to \infty) \propto \exp\left(-\frac{\tau_{Dx}}{2\tau_{Px}^2}\Delta_x\right)$, where $x = (f,\, b)$. Unfortunately, this mathematical form makes it impossible to calculate $F_1(\tau)$, $F_2(\tau)$, $F_3(\tau)$, and $F_4(\tau)$ analytically. We therefore resort to numerically integrate these functions. The velocity autocorrelation function in this case is given by $F(\tau) = \frac{1}{d(\tau_{Pf}+\tau_{Pb})}\left(F_1(\tau) + F_2(\tau) + F_3(\tau) + F_4(\tau)\right)$, where $\tau_{Pf} \equiv \langle\Delta_f\rangle$ and $\tau_{Pb} \equiv \langle\Delta_b\rangle$. The codes are optimized so that it is efficient enough to allow non-linear least square fit to be implemented.

2.4.3 Appendix C: Bacterial cultures and measurement techniques

2.4.3.1 Bacterial cultures *E. coli* RP437 were grown overnight (ON) in M9 medium (0.6% Na_2HPO_4, 0.3% KH_2PO_4, 0.1% NH_4Cl, 0.05% NaCl, 1 mM $MgSO_4$, 0.2% lactose, 0.1% casamino acids, 5×10^{-5} % thiamine) at 30 °C with shaking at 200 rpm. The ON was diluted 1:100 in fresh M9+lactose and grown to O.D.600 $\sim$ 0.2. The cells were washed once in the motility buffer (10 mM potassium phosphates, 10 mM sodium lactate, 0.1 mM EDTA, 1uM L-methionine, pH=7.0), and then incubated in the motility buffer with shaking at 200 rpm for more than 30 min at room temperature before measurement.

V. alginolyticus were grown overnight in the VC medium (5 g polypeptone, 5 g yeast extract, 4 g K_2HPO_4, 30 g NaCl, 2 g glucose, and 10^3 mL H_2O) at 30 °C with shaking at 200 rpm. The ON is inoculated at 1:100 in VPG (10 g polypeptone, 4 g K_2HPO_4, 30 g NaCl, 5 g glycerol, and 10^3 mL H_2O) and grown to O.D.600 $\sim$ 0.2. Before the measurements, the cells were inoculated at 1:100 to TMN buffer (50 mM Tris-HCl (pH 7.5), 5 mM $MgCl_2$, 5 mM glucose, 30 mM NaCl, and 270 mM KCl) and incubated with shaking at room temperature for more than 30 min. The growth protocol follows Ref. [34].

2.4.3.2 Imaging and bacterial tracking To obtain bacterial swimming trajectories, a sample chamber was made by sandwiching a 1.2 mm thick silicon gasket between two coverslips. In the case of point stimulation using serine, an open chamber was used. The chamber was filled with bacteria in a motility buffer and observed under an inverted microscope (Nikon, TE-300) equipped with a 20x (n.a. 0.45) and a 60x (n.a. 0.70) objective. The image plane was $\sim$ 100 μm away from surfaces, which significantly reduced distortion of bacterial swimming trajectories near the surface. The typical time between filling the sample and the measurements was about 5-10 minutes. We noticed that a few minutes after the bacteria were introduced, the motility patterns and their associated parameters were not changed discernibly in the open and closed chambers, indicating that oxygen stress was not a problem in our measurements. Videos were taken at 30 fps by a charge couple device camera (Hamamatsu, C9100). We used ImageJ (Particle Tracker plug-in) to analyze video images and customized MATLAB programs to perform calculations.

In all measurements, bacterial concentrations were very low. For example, in the open chamber, there was only a few bacteria in the field of the view when there was no chemical gradient present. A steady chemical gradient was established by slow ejection of 1 mM serine in the motility buffer from a micropipette situated at the center of the field of view; more details about this setup can be found in Ref. [5]. For YM4, we started video capturing as soon as a cell was detected within the region of interest (ROI) defined as a 100 μm radius centered at the tip of the micropipette. Video capturing was stopped when the ROI was overly crowded, i.e. more than 5-6 cells in the area. In the ROI, we followed every trajectory that stayed focused sufficiently long to have multiple forward-backward swimming cycles. For the data presented in Fig. 6 (D), we captured three videos and followed 42 trajectories with varying lengths, ranging from 1.7 to 22 s. Similar or better statistics were collected for other runs and their corresponding uncertainties in the measured MSD are presented by the error bars in Fig. 6.

3.0 BACTERIAL MOTILITY PATTERNS IN POLYMER SOLUTIONS

3.1 INTRODUCTION

Flagellar propulsion of bacteria is one of the most important forms of microorganisms' motility, the studies of which help to solve puzzles in bacterial motility-related topics, such as an early phase of infection [35], bacterial spreading [36], and biodegradation of organic material [37]. Most of the time, the environments where bacteria live are not purely liquid but contain macromolecules, such as polymers. These biopolymers form so-called complex fluids and influence motility of bacteria significantly. The most famous example of microorganisms swimming in complex fluids might be the locomotion of sperm cells in the mucus environments (cervical fluid) [38]. The mucus in human's upper respiratory tract being the barrier to prevent the bacterial infection is also well-known. *Helicobacter pylori* causing peptic ulcer disease can even control the elasticity of fluid in the gastrointestinal tract to overcome the mucus barrier of the stomach [39].

From a physics point of view, adding polymers into the fluids is to add fluid viscoelasticity. How viscoelasticity influences the swimming of cells remains to a puzzle [40]. For example, regarding swimming speed, experimental results show that both enhancing and retarding effects can be found in viscoelastic environments for different species of microorganisms. *Borrelia burgdorferi* has a higher swimming speed in methylcellulose solutions than in buffers with same viscosity [41]. Mouse sperm cells swim slower in the fluid with extra elastic effect [42]. However, *E. coli* shows a non-monotonic relationship of swimming speed and polymer concentrations when the polymer solutions display a non-Newtonian effect [43]. In our measurement, we find that the flicking events of *V. alginolyticus* are suppressed when polymers are added in solution, and the swimming speed decreases with an increasing poly-

mer concentration, which is not consistent with the earlier measurement of *E. coli* [43]. However, this suggests that by adjusting a small amount of polymers in a fluid environment we can control the spreading of *V. alginolyticus*. During the study, the velocity autocorrelation function $\langle \vec{v}(t) \cdot \vec{v}(0) \rangle$ has been chosen to quantify bacterial motility patterns, from which we observe non-Poissonian behaviors of *V. alginolyticus* again. Velocity autocorrelation function provides more fundamental information than MSD, which is present in Chapter 2, because MSD is the integral of the velocity autocorrelation function. A stochastic model has been developed to quantify the suppression effects. In the meantime, we unexpectedly discover a "resonance-like" effect of the swimming directional autocorrelation functions of bacteria when the polymer concentration is close to the overlapping concentration of polymer solutions, ϕ^*, where polymer coils start to touch each other. This effect can be explained by a harmonic oscillator model, which could be a tool to quantify the coupling of bacterial motors fluctuations and the viscoelasticity of polymer environments. The biological relevance of this effect is possible that in the marine habitat of *V. alginolyticus*, although sea water is mainly a viscous medium, viscoelastic environments are rare but exist. *V. alginolyticus* has different strategies to deal with these two different environments. It has been reported that *V. alginolyticus* can infect white shrimp and gilt-head sea bream [44][45]. During the process of infection, bacteria have to locate the targets and overcome the barrier of mucus-like surfaces of marine shrimps and fishes. The "resonance-like" effect could possibly be the response of *V. alginolyticus* to lock the target. Suppression of flicking is beneficial to locate bacteria on the marine animal skin to keep persistent infection.

In the final section of this chapter, with the resistive force theory, swimming velocities vs. viscosity of polymer solutions has been obtained, and the results imply that the viscosity felt by bacteria is lower than the bulk viscosity.

3.1.1 Experimental details

The Fig. 10 shows the experimental platform we used. During measurements, we gently mixed each concentration of polymer solutions with bacterial suspensions in a cylinder chamber (diameter 1.1 cm and depth 1.2 mm, respectively). The chamber had a sandwich

structure, with two cover slips covering a 1.2-mm-thick silicon gasket. After mixing, the sample was observed under an inverted microscope (Nikon, TE-300). The focal plane of the microscope was adjusted away from the surface of the top and bottom glass surfaces (distance $\sim 600\ \mu$m), avoiding the boundary effect. Multiple 3000-frame videos were recorded with the CCD camera (Hamamatsu, EM-CCD C9100) with the frame rate set to 35 fps. The magnification of the microscope (20X, 40X and 60X objectives were used in the measurements) were adjusted based on cell swimming speed to guarantee high efficiency of trajectories tracking and sufficient spatiotemporal resolution. The recorded videos were handled by MosaicSuite of Fiji (National Institutes of Health) and MATLAB to extract trajectories. In order to get sufficient statistics, we randomly selected ten different places in the chamber to record videos and repeated this procedure three times. In total, we have 30 parallel measurements for a single polymer concentration. Eventually, we can track $3000 \sim 6000$ cells for each concentration. Since sizes of video files were large and USB transferring of data was too slow, we migrated data directly via the network from the experiment-control computer to a data-processing computer. Shell scripts and Fiji plugins were integrated to automate data transferring, image processing, and trajectory tracking procedure, enhancing the efficiency of data processing significantly.

The data from this 1st round of processing were still mixed with false-positive trajectories. A machine learning program was then used to distinguish false-positive trajectories from real ones. The program is based on Andrew Ng's online course. All the program used in this chapter can be downloaded from https://github.com/sudoyang.

3.1.2 Polymer property

The polymer we used is Fluka Polyvinylpyrrolidone (PVP) K-90, which has a number averaged molecular weight of $M_n = 360$ kDa and a weight-averaged molecular weight of $M_w \approx 10^6$ Da [43]. This corresponds to a polydispersity $M_w/M_n \approx 2.8$. PVP is a single-chain polymer with the chemical formula of monomer C_6H_9NO. Its linear dimension, estimated by the carbon-carbon bond distance is $a \approx 0.31$ nm. In a good solvent, assuming a random walk of a polymer chain, we estimate the radius of gyration to be $r_g\ (\equiv aN^{\nu}) \approx 39$ nm , where

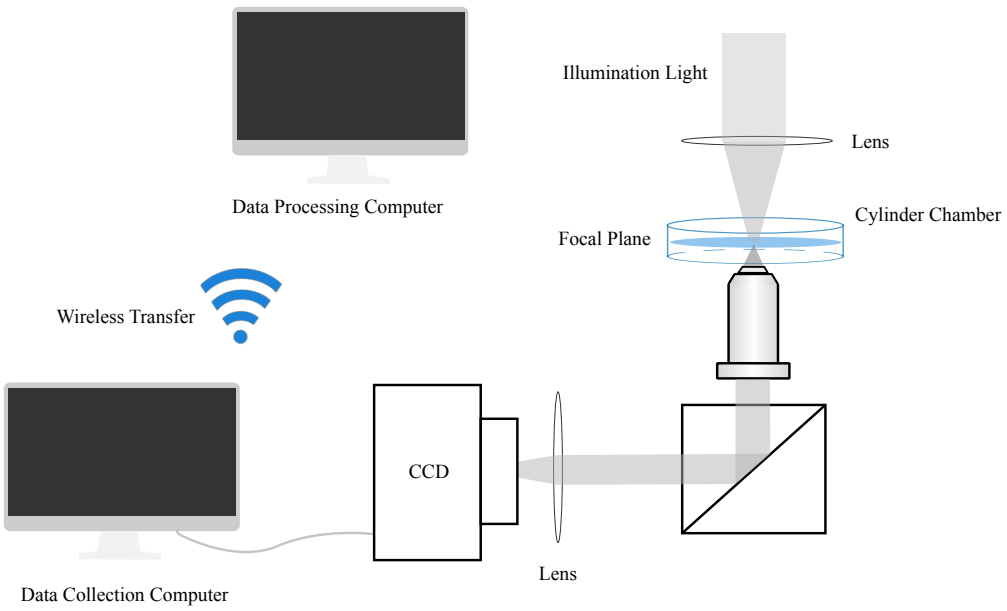

Figure 10: The experimental setup. We used a phase-contrast microscope technique. The sample in the chamber is illuminated by a focused beam of light and the transmitted light, which carries the refractive index difference information, passes through the objective and is collected by the CCD camera. Videos were taken and stored in the data collection computer and then transferred to a separated data processing computer.

$N = 3.2 \times 10^3$ is the average number of monomers in a random walk chain, and $\nu \approx 0.6$ is the exponent for a self-avoidance random walk of a polymer chain [46]. An overlapping concentration can be obtained as $\phi^* = M_w n_C / \rho N_A \approx 1.01\%$, where $n_C = \frac{1}{r_g^3}$ is the closed packing concentration, ρ is the density of solution, and N_A is the Avogadro constant. The measured overlapping concentration is $\phi^* = 0.55 \pm 0.01\%$ and radius of gyration $r_g = 56$ nm according to Ref. [43]. Two kinds of PVP solutions were used: normal and dialyzed solutions. Dialysis tubing we used is from Fisher Scientific with the molecular weight cutoff (MWCO) at 12-14 kDa. The purpose to use the dialyzed solutions is that based on the report [43], bacteria may consume small polymer pieces, which can influence swimming velocities. But from our measurement, we did not find this effect.

We initially used the polymer Methylcellulose (MC) for the experiment, but the time for this polymer to dissolve is too long to be effectively used. Even after dissolution, the solution was heterogeneous when viewed under the microscope, which influenced the measurement significantly. We decided to switch to PVP, which was easy to dissolve and the solution was homogeneous.

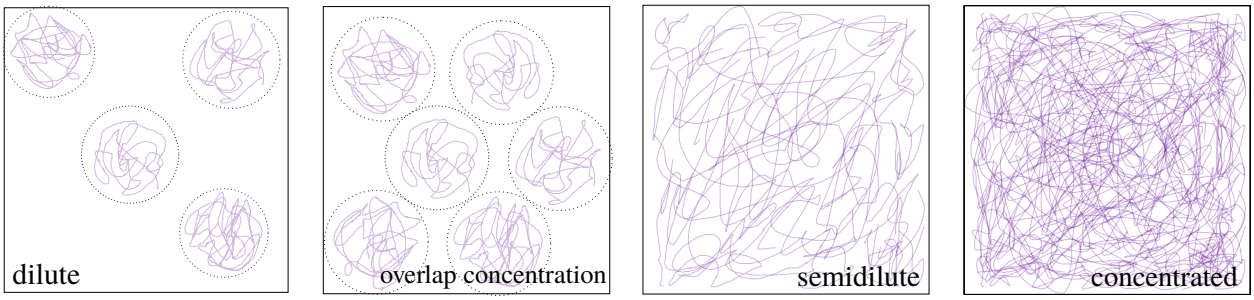

Figure 11: PVP polymer concentration regimes in good solvent: dilute, semidilute,and concentrated. Between dilute and semidilute regimes, there is a critical concentration ϕ^*, at which the overlap of polymer coils starts.

In our experiments, the whole range of polymer solutions not only covers a broad span of concentrations but also contains fine increments at low concentrations ($< 10\%$): $\phi = 0$, 0.25, 1, 2.25, 2.5, 5, 7.5, 10, 12.5, 15, 20, 25, and 30%. Roughly speaking, the concentrations 0% and 0.25% belong to a dilute regime. The concentrations 2.25%, 2.5%, and 5% are falling into a semidilute regime. For concentrations higher than 5%, they belong to a concentrated

regime. The critical concentration is 1%, which is the overlap concentration. The behaviors of polymers in micro-scale are illustrated schematically in Fig. 11.

3.2 THE EXPERIMENTAL RESULTS

As mentioned in Chapter 1, the single-flagellum marine bacterium *V. alginolyticus* performs a run-reverse-flick motility pattern in the swimming buffer; a sample trajectory is shown in Fig. 12 (A). However, when polymers are added to the swimming buffers, the flick events are found to be suppressed. The motility pattern becomes a sequence of several run-reverse intervals connected by flick events. We show this in Fig. 12 (B). This swimming behavior can be modeled effectively by a stochastic model described in the following section. What surprised me is that I did not expect that in our highest polymer concentration bacteria could still swim, but they do except with a reduced swimming velocity.

3.2.1 The velocity autocorrelation functions measured in the experiments

We used velocity autocorrelation function (ACF) to quantify changes in motility patterns in different polymer concentrations. The velocity ACF is defined as,

$$\langle \vec{v}(t) \cdot \vec{v}(0) \rangle = \langle \vec{v}_n \cdot \vec{v}_1 \rangle = \frac{1}{N-n} \sum_{i=1}^{N-n} \vec{v}_{i+n} \cdot \vec{v}_i, \tag{3.1}$$

where the subscripts indicate the frame numbers, and $t = n\Delta t$ with Δt being the interval between video frames. N is the total frame number of certain trajectory.

We realized that the fluctuations in the swimming speed and the swimming directions happen in different time scales, so they can be approximated as

$$\langle \vec{v}(t) \cdot \vec{v}(0) \rangle = \langle v(t)v(0) \rangle \langle \hat{a}(t) \cdot \hat{a}(0) \rangle. \tag{3.2}$$

In frame indices n, Eq. 3.2 is

$$\langle \vec{v}_n \cdot \vec{v}_1 \rangle = \langle v_n v_1 \rangle \langle \hat{a}_n \cdot \hat{a}_1 \rangle, \tag{3.3}$$

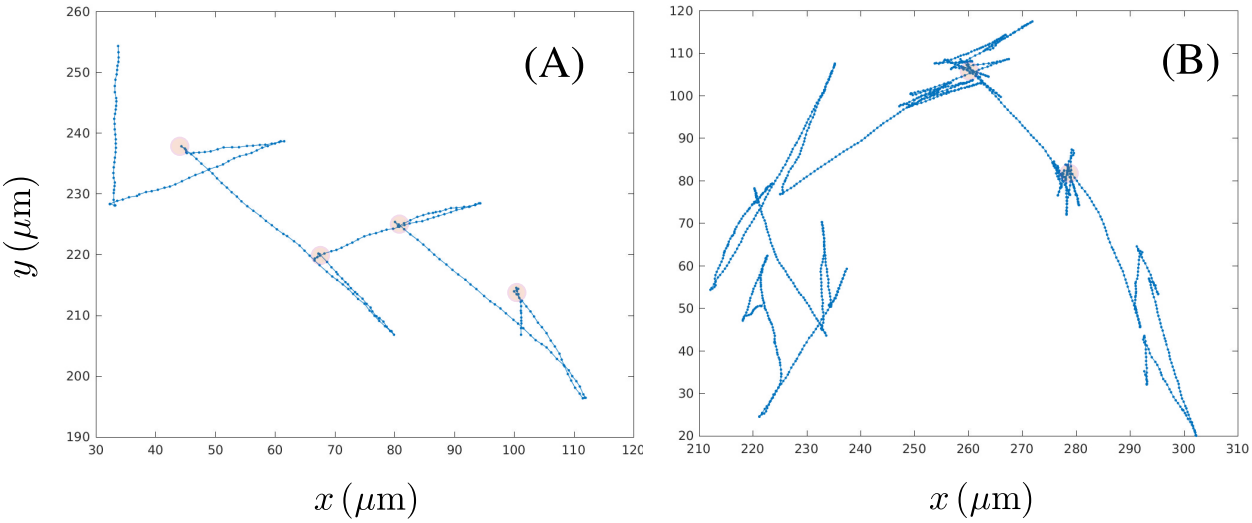

Figure 12: Typical *V. alginolyticus* motility patterns in buffer (A) and in a polymer solution (B). In (A), we can see a standard three-step motility pattern of *V. alginolyticus* and in (B) it is noticed that the flicking events are suppressed. A a sequence of run and reverse intervals are connected and interrupted by a rare flicking event. Some sample flicking events have been circled with red color.

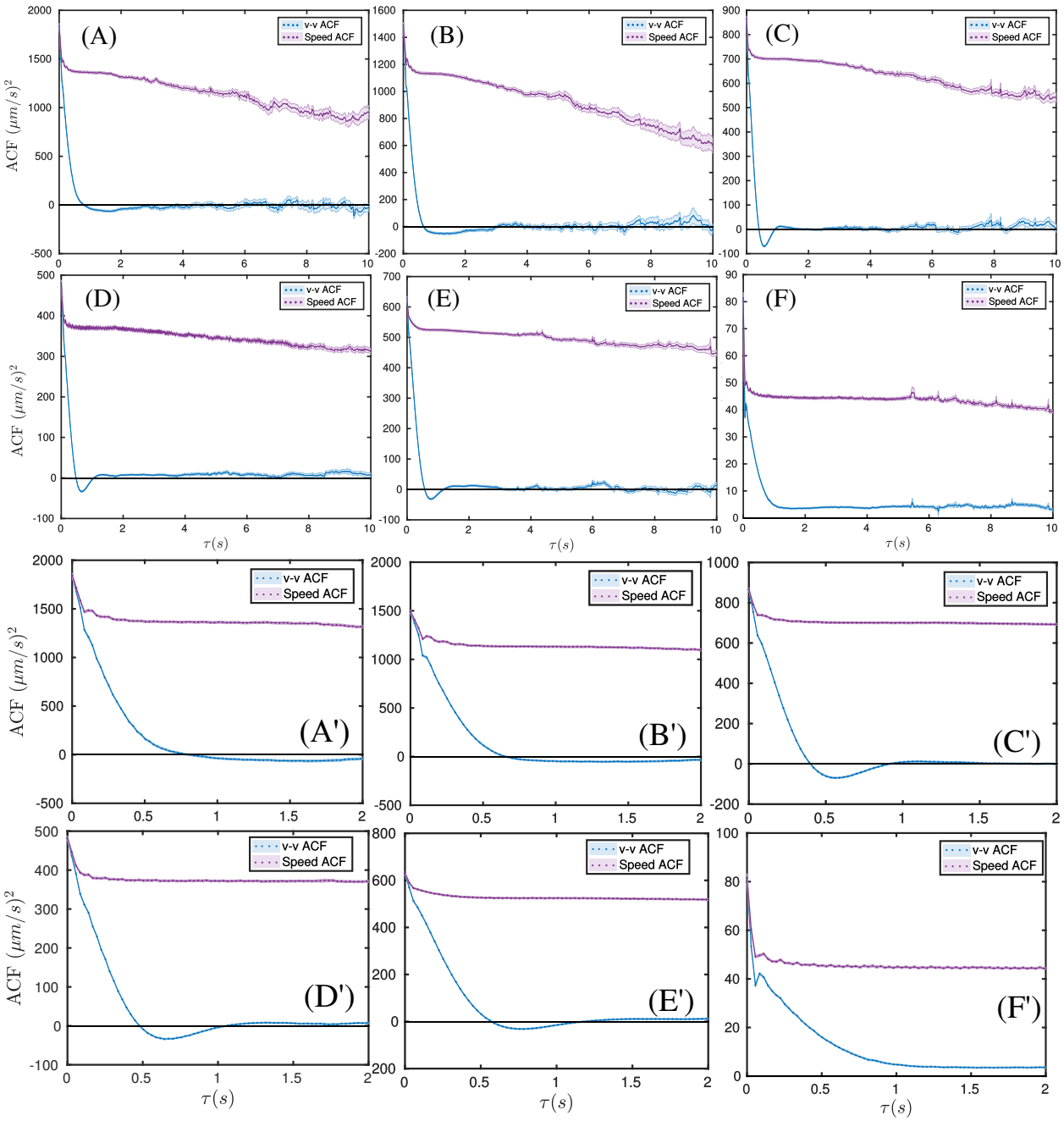

Figure 13: Measured velocity and speed ACFs for *V. alginolyticus*. (A-F) display results from 0%, 0.25%, 1%, 2.25%, 2.5% and 5% polymer solutions. The purple and blue lines are for the speed and velocity ACFs, respectively. (A'-F') are re-plotted from (A-F), with a shorter time span of 2 seconds. It can be noticed that velocity and speed ACFs has similar fluctuations behaviors in very short time.

where $\langle v_n v_1 \rangle$ and $\langle \hat{a}_n \cdot \hat{a}_1 \rangle$ indicate speed and directional ACFs, respectively. We note that since the marine bacterium alters its swimming direction on a time scale of a second, the short-time decay of velocity ACF in Fig. 13 must be due to swimming speed fluctuations. In our previous experiment, we showed that *V. alginolyticus*' swimming speeds in the run and reverse intervals, to within $\sim 10\%$, are identical. The experimental results support the argument of timescale separation after we plot velocity and speed ACFs (see Fig. 13), in which we can find a drop of the function $\langle v_n v_1 \rangle$ at the beginning three to four frames, and the same behavior can also be noticed in velocity ACF, $\langle \vec{v}_n \cdot \vec{v}_1 \rangle$. Then we use the speed ACF to normalize the velocity ACF and plot the results in Fig. 14. The ACFs of velocity directions $\langle \hat{a}_n \cdot \hat{a}_1 \rangle$ would be our objectives to tackle with.

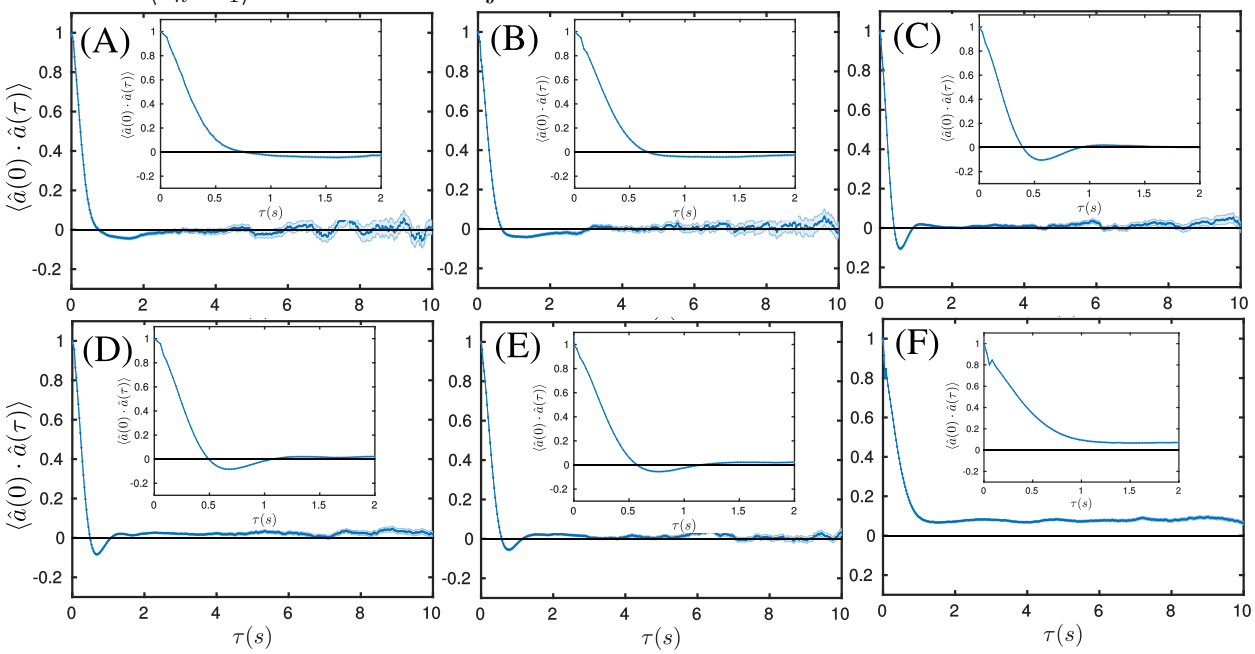

Figure 14: Swimming directional ACFs of *V. alginolyticus*. (A-F) show results with polymer concentrations of 0%, 0.25%, 1%, 2.25%, 2.5%, and 5% polymer solutions, respectively. The insets are the same data, which only show the beginning 2 seconds and the rounded tops at the beginning of curves indicate a non-Poissonian property of *V. alginolyticus* motility patterns.

There is a slow decay of the speed ACFs for t in the range of 5 to 10 seconds. The first impression we have is that long trajectories in the ensemble of all collected data are

due to slow swimmers. However, Fig. 15 shows that this is not the case; no correlations between trajectory length and bacterial speed is found here. So the decay of speed as a function of time is an intrinsic effect rather than a bias in data collection. This should be consistent with our expectation. The speed ACFs for all polymer concentrations contain a fast component and a slow component. The speed fluctuations are due to the following effects: (i) A swimming trajectory is intrinsically curved, and local curvatures change from moment to moment. When sampled by discrete points by video microscopy, it naturally leads to speed fluctuations. (ii) Rotation of the flagellar motor is unsteady and can fluctuate on different time scales. Short-time fluctuations along with effect in (i) contribute to the fast decay in speed ACFs, and long-time fluctuations, which become most prominent when motor reverses, contribute to slow decay in speed ACFs. We take the crossover point between the short- and long-time as the average swimming speed, which turns out to be in a qualitative agreement with direct calculations using the time series. Moreover, after a normalization of plateau regimes in speed ACFs to one, Fig. 16 shows a collapse of the speed ACFs for all concentrations except the highest one, 5%.

3.3 STOCHASTIC MODELS

To explain our experimental observation, theoretical models are constructed. Our calculation starts with the classical analysis of Lovely et al. [29] and a recent calculation by Taktikos et al. [23] for *E. coli*. Important extensions of the current work for *V. alginolyticus* are the CCW and CW swimming intervals (i) being non-Poissonian, (ii) obeying different dwell time distributions (PDFs), and (iii) having different mean-dwell times, $\bar{t}_1$ and $\bar{t}_2$, where $\bar{t}_1$ is for CCW and $\bar{t}_2$ is for CW intervals.

3.3.1 A Poisson model for motility patterns of *E. coli*

As mentioned in Chapter 1, *E. coli* follows a run-tumble motility pattern. In the calculation of Lovely and Taktikos, two features are crucial for modeling: 1. The run time of *E. coli*

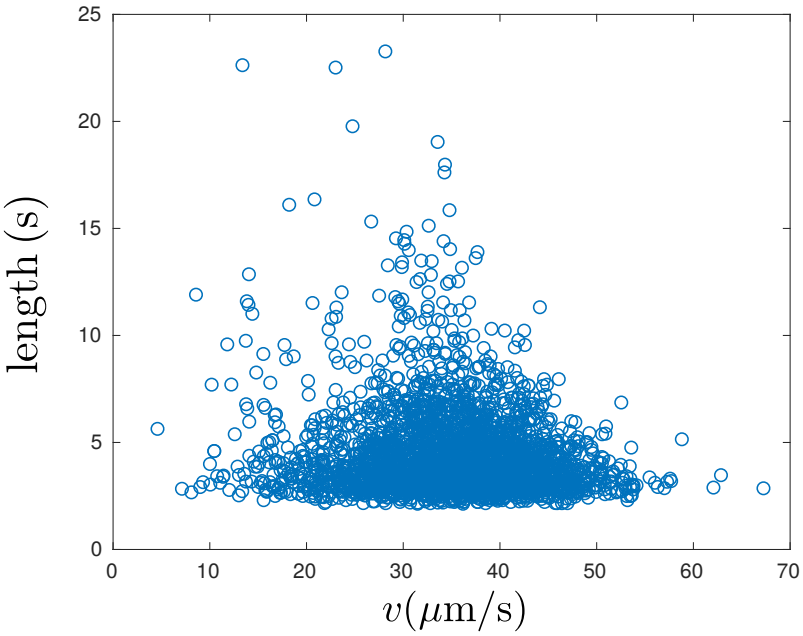

Figure 15: Scatter plot of trajectory lengths vs. speeds. All trajectories that are shorter than 3 seconds have been eliminated. The figure shows an unbiased, uncorrelated scatter plot.

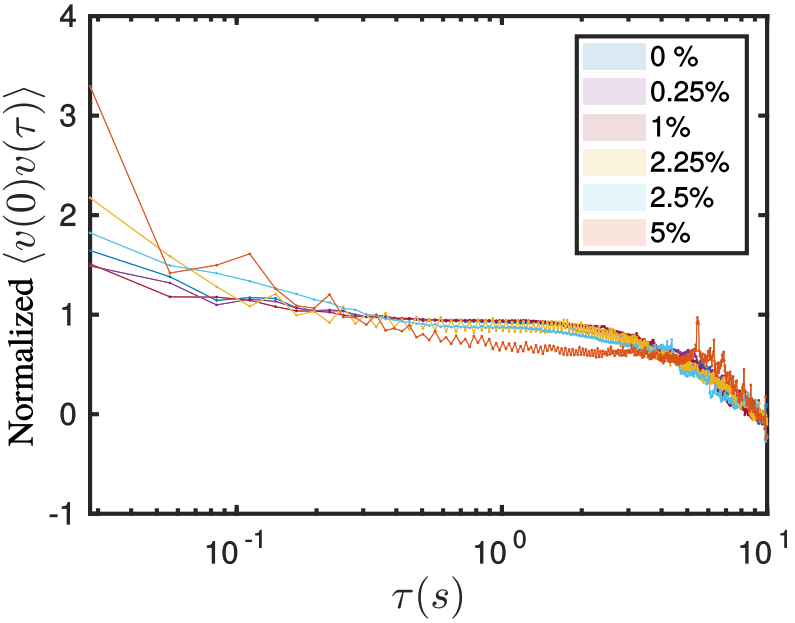

Figure 16: Normalized speed ACFs. The speed ACFs of all concentrations, but 5%, can be collapsed into a same curve.

is a random variable, which follows an exponential distribution with the mean run time 1 s [25][30]. So the motility of *E. coli* follows a Poisson process. 2. The tumbling angle of *E. coli* also follows a distribution with a mean tumbling angle of $\theta = 70°$ [47]. The parameter $\alpha = \langle \cos\theta \rangle$, which is the mean cosine of the angle between two adjacent run segments, characterizes the persistence of motion. For *E. coli*, α is approximately equal to 0.33.

I try to re-derive Lovely's results here. A unit vector $\hat{a}(t)$ is used to indicate the direction of motion of a swimming bacterium at time t, and the directional ACF follows the definition in [29], which is

$$C(t) = \langle \hat{a}(0) \cdot \hat{a}(t) \rangle. \tag{3.4}$$

In a time interval $[0, t]$, suppose that a cell tumbles n times, so the trajectory of the cell contains $n+1$ run intervals, with the directions of the corresponding run intervals being $\hat{a}_0$, $\hat{a}_1$, ..., $\hat{a}_{n-1}$, and $\hat{a}_n$, which are shown in Fig. 17. The correlations between two adjacent run intervals can be noted as $\langle \hat{a}_0 \cdot \hat{a}_1 \rangle = \alpha$, $\langle \hat{a}_1 \cdot \hat{a}_2 \rangle = \alpha$, ..., and $\langle \hat{a}_{n-1} \cdot \hat{a}_n \rangle = \alpha$. For the whole trajectory, the averaging process goes from the initial direction $\hat{a}(0)$ to all the following unit vectors up to $\hat{a}(t)$,

$$\langle \hat{a}(0) \cdot \hat{a}(t) \rangle = \langle \hat{a}_0 \cdot \hat{a}_n \rangle = \alpha \cdot \alpha ... \alpha = \alpha^n. \tag{3.5}$$

Next, we need to average the number of tumbling events during 0 and t. The probability distribution of numbers of tumble follows a Poisson distribution P_n, which has the form

$$P_n = \frac{(t/\tau)^n}{n!} e^{-t/\tau}, \tag{3.6}$$

where τ is the mean run time of *E. coli*.

In time t, the bacterium can experience just one tumble, two tumbles, and up to $n = \infty$. Taking all these possibilities into account, we obtained,

$$\begin{aligned} \langle \hat{a}(0) \cdot \hat{a}(t) \rangle &= P_0\alpha^0 + P_1\alpha^1 + ... + P_n\alpha^n + ... \\ &= \sum_{n=0}^{\infty} \frac{(\alpha t/\tau)^n}{n!} e^{-t/\tau} = e^{\alpha t/\tau} e^{-t/\tau} = e^{-(1-\alpha)t/\tau} = e^{-t/\tau_c}, \end{aligned} \tag{3.7}$$

where τ_c is the correlation time given by $\tau_c = \frac{\tau}{1-\alpha}$. When a bacterium keeps moving in a straight line with $\alpha \to 1$, $\tau_c \to \infty$, which means the correlation always exists. However, if $\alpha \to 0$, which means for each tumble the bacterium completely randomizes its direction, the correlation time will be just mean swimming time τ.

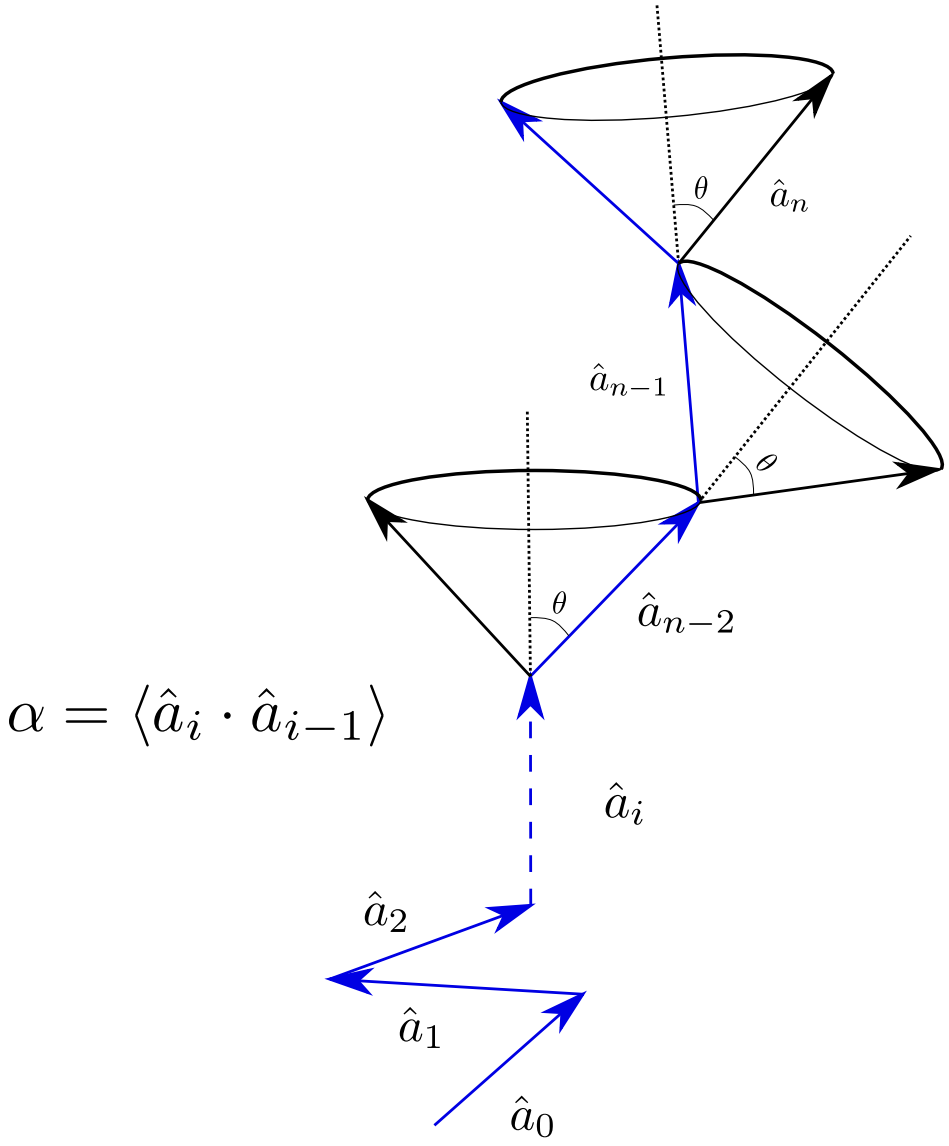

Figure 17: The interpretation of directional ACF calculation of *E. coli* motility patterns. In the time period of $[0, t]$, there are $n + 1$ run intervals, the directions of which are labeled with $\hat{a}_i$ $(i = 0, 1, ..., n)$. With tumbling angles fixed as their mean value, $\hat{a}_i$ can rotate freely around $\hat{a}_{i-1}$ on the surface of a cone of half angle θ, so the average correlation between ith and $(i + 1)$th intervals is α. The average along the whole trajectory is α^n.

3.3.2 A generalized Poisson model for motility patterns of *V. alginolyticus*

3.3.2.1 A Poisson model with finite number of swimming cycles before randomization. In this section, we would like to consider a more general model that fits *V. alginolyticus*'s motility patterns in polymer solutions. First, to capture the essential features of motility patterns in the swimming buffer, which is a three-step process, we need to introduce α and β being the mean cosine angles between flagellar motor reversals (Fig. 18 (B)), as what we have done in *E. coli*'s case with a single mean cosine of the tumbling angle α. Here, $\alpha = \langle \cos\theta_1 \rangle$ and $\beta = \langle \cos\theta_2 \rangle$ indicate the angle between the run and reverse intervals and the angle between the reverse and run intervals, respectively. We again assume that the random processes of run and reverse intervals follow the Poisson processes with different mean dwelling times. Thus the swimming intervals obey the exponential distributions, $f_i(t) = k_i e^{-k_i t}$, and $F_i(t) \equiv 1 - \int_0^t \mathrm{d}t' f_i(t') = e^{-k_i t}$ is the survival probability of the exponential distributions, with $i = 1$ (run) and 2 (reverse). The mean dwelling times of swimming intervals of run and reverse $\bar{t}_1$ and $\bar{t}_2$ are reciprocals of k_1 and k_2, respectively. The directional ACF can be expressed in the following form,

$$
\begin{aligned}
C(t) \equiv \langle \hat{a}(t) \cdot \hat{a}(0) \rangle &= F_1(t) + \int_0^t \mathrm{d}t_1 f_1(t_1) \alpha F_2(t - t_1) + \int_0^t \mathrm{d}t_2 \int_0^{t_2} \mathrm{d}t_1 f_1(t_1) \alpha f_2(t_2 - t_1) \beta F_1(t - t_2) \\
&+ \int_0^t \mathrm{d}t_3 \int_0^{t_3} \mathrm{d}t_2 \int_0^{t_2} \mathrm{d}t_1 f_1(t_1) \alpha f_2(t_2 - t_1) \beta f_1(t_3 - t_2) \alpha F_2(t - t_3) + ... \\
&+ \int_0^t \mathrm{d}t_m \int_0^{t_m} \mathrm{d}t_{m-1} ... \int_0^{t_2} \mathrm{d}t_1 f_1(t_1) \alpha f_2(t_2 - t_1) \beta f_1(t_3 - t_2) ... \alpha F_2(t - t_m) + ... \\
&= F_1 + \alpha f_1 * F_2 + \alpha\beta f_1 * f_2 * F_1 + \alpha^2 \beta (f_1)^2 * f_2 * F_2 + \alpha^2 \beta^2 (f_1)^2 * (f_2)^2 * F_1 + ... + \\
&\alpha^m \beta^{m-1} (f_1)^m * (f_2)^{m-1} * F_2 + ...
\end{aligned}
\tag{3.8}
$$

In the above, "$*$" indicates the convolution, $(f * g)(t) = \int_0^t f(t') g(t - t') dt'$.

After the polymer is added, the flick events are suppressed, and the motility pattern becomes a sequence of serveral run-reverse intervals connected by flick events; namely, a cell does not randomize its swimming direction until it executes m-cycles of motor reversals. As long as there is a flick event, the infinite sum in Eq. 3.8 will be terminated since $\cos 90^\circ = 0$.

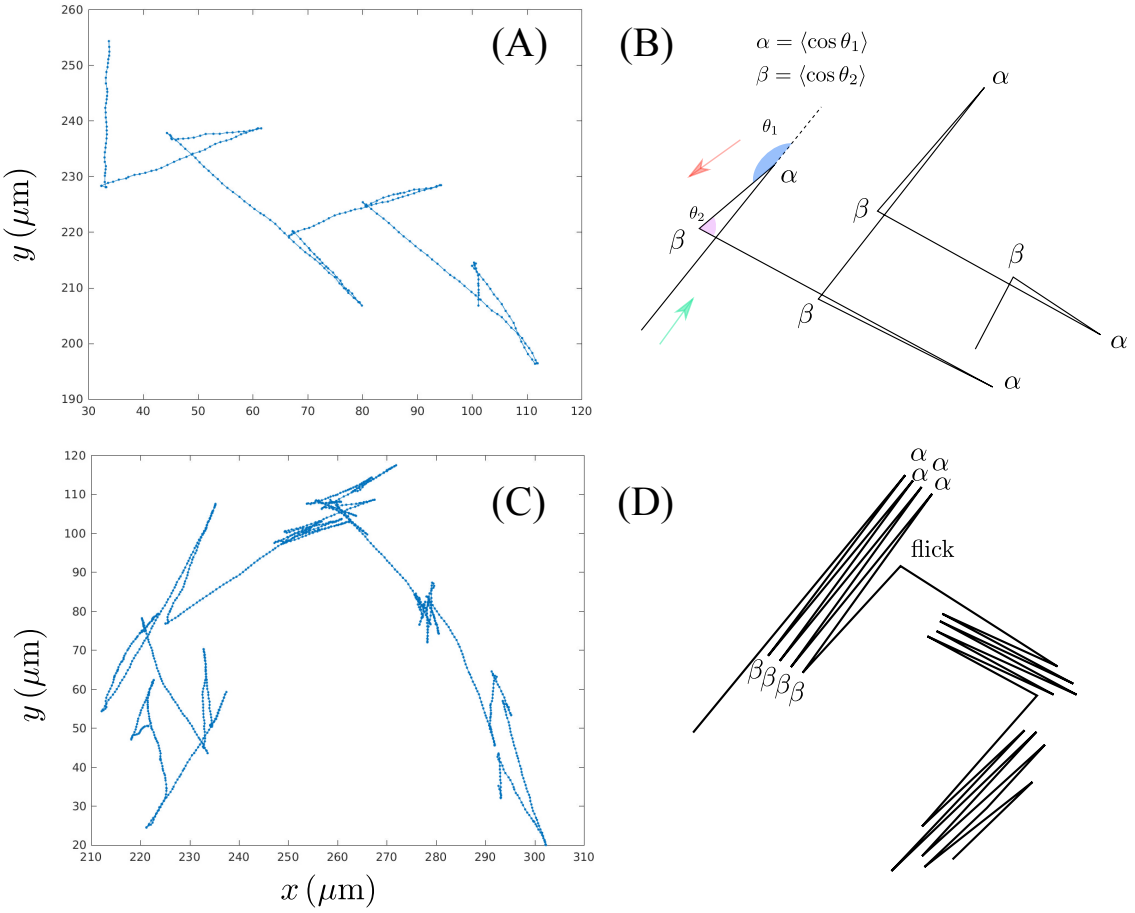

Figure 18: Figures (A) and (C) show the sample trajectories for *V. alginolyticus* swimming in the buffer and in the polymer solution, respectively. Their corresponding model trajectories with $m = 1$ and $m = 4$ are depicted in (B) and (D). m is the number of complete run-reverse cycle before a randomized flick.

A hypothetical trajectory with CCW-CW-CCW-CW-CCW-CW-CCW-CW-90° ($m = 4$) is delineated in Fig. 18 (D). In this case, there are only $2m$ terms left in Eq. 3.8, we can group all terms according to the individual swimming cycles, e.g. the first two terms in Eq. 3.9 corresponds to cycle $m = 1$, and the third and fourth terms corresponds to $m = 2$, and etc. Suppose the trajectory starts with a CCW interval, finish m swimming cycles and then is terminated with a randomized flicking event, which is illustrated in Fig. 19 with $m = 3$ as an example, we have,

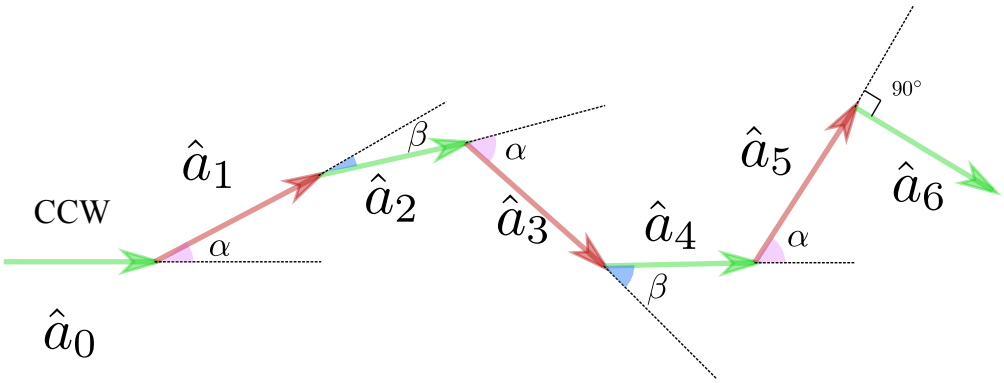

Figure 19: A sample trajectory starting with a CCW interval, which is labeled with a green arrow. Its corresponding turning angle's cosine value is α. It is followed by a red arrow indicating a CW interval and the corresponding turning angle's cosine value for the CW interval is β.

$$C_1(m,t) \equiv \langle \hat{a}(t) \cdot \hat{a}(0) \rangle = F_1 + \alpha f_1 * F_2 + \alpha\beta f_1 * f_2 * F_1 + \alpha^2\beta (f_1)^2 * f_2 * F_2 + \alpha^2\beta^2 (f_1)^2 * (f_2)^2 * F_1 + ... + \alpha^m \beta^{m-1} (f_1)^m * (f_2)^{m-1} * F_2. \tag{3.9}$$

In short, we have

$$C_1(m,t) = \sum_{q=1}^{m} c_1(q,t), \tag{3.10}$$

with

$$c_1(q,t) = (\alpha\beta)^{q-1} \left(f_1^{q-1} * f_2^{q-1} * F_1 + \alpha f_1^q * f_2^{q-1} * F_2 \right) = (\alpha\beta)^{q-1} (f_1 * f_2)^{q-1} * (F_1 + \alpha f_1 * F_2), \tag{3.11}$$

where multiplications of $f_i^p * f_j^q$ stand for $p+q$ folds of convolution and $C_1(m,t)$ should have $2m$ terms, with $m \geq 1$.

Since the experimental data are acquired from a mixed ensemble of cells, some trajectories start at CCW interval and others start at CW intervals, thus we need to take into account the second case delineated by Fig. 20, in which all trajectories starts with a CW interval. This yields

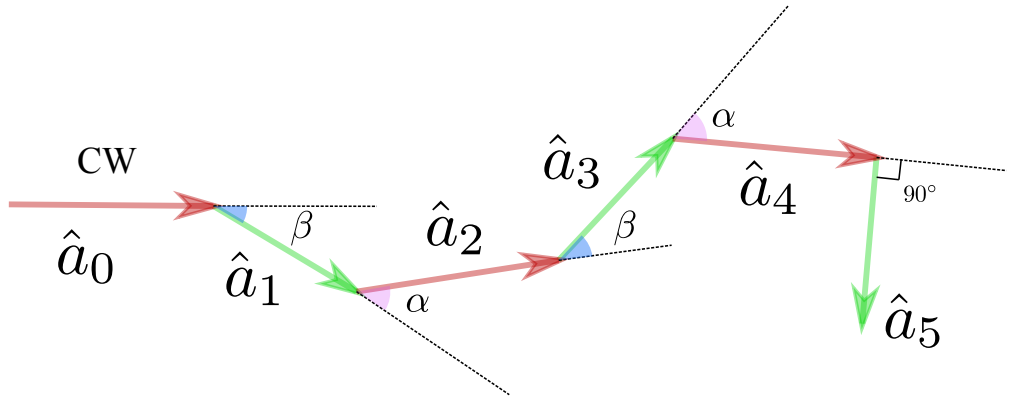

Figure 20: A sample trajectory starting with a CW interval.

$$
\begin{aligned}
C_2(m,t) \equiv \langle \hat{a}(t) \cdot \hat{a}(0) \rangle &= F_2(t) + \int_0^t \mathrm{d}t_1 f_2(t_1) \beta F_1(t-t_1) + \int_0^t \mathrm{d}t_2 \int_0^{t_2} \mathrm{d}t_1 f_2(t_1) \beta f_1(t_2-t_1) \alpha F_2(t-t_2) \\
&+ \int_0^t \mathrm{d}t_3 \int_0^{t_3} \mathrm{d}t_2 \int_0^{t_2} \mathrm{d}t_1 f_2(t_1) \beta f_1(t_2-t_1) \alpha f_2(t_3-t_2) \beta F_1(t-t_3) + \ldots \\
&+ \int_0^t \mathrm{d}t_m \int_0^{t_m} \mathrm{d}t_{m-1} \ldots \int_0^{t_2} \mathrm{d}t_1 f_2(t_1) \beta f_1(t_2-t_1) \alpha f_2(t_3-t_2) \ldots \beta F_1(t-t_m) \\
&= F_2 + \beta f_2 * F_1 + \alpha\beta f_2 * f_1 * F_2 + \alpha\beta^2 (f_2)^2 * f_1 * F_1 + \alpha^2\beta^2 (f_2)^2 * (f_1)^2 * F_2 + \ldots + \\
&\alpha^{m-1}\beta^{m-1} (f_2)^{m-1} * (f_1)^{m-1} * F_2.
\end{aligned}
\tag{3.12}
$$

Writing in terms of individual swimming intervals as above, we find,

$$
C_2(m,t) = \sum_{q=1}^{m} c_2(q,t), \tag{3.13}
$$

and

$$
\begin{aligned}
c_2(q=1,t) &= F_2, \\
c_2(q\geq 2,t) &= \alpha^{q-2}\beta^{q-1} f_1^{q-2} * f_2^{q-1} * \Big(F_1 + \alpha f_1 * F_2\Big),
\end{aligned}
\tag{3.14}
$$

where $C_2(m,t)$ has $2m-1$ terms.

The final results of $C(m,t)$ should take the ensemble average of $C_1(m,t)$ and $C_2(m,t)$ with their mean dwelling times as the weights,

$$
C(m,t) = \frac{1}{\bar{t}_1+\bar{t}_2}\Big(\bar{t}_1 C_1(m,t) + \bar{t}_2 C_2(m,t)\Big). \tag{3.15}
$$

Eq. 3.15 gives us the directional ACF with finite number of swimming cycles (m cycles).

3.3.2.2 Discussion of the Poisson model Below we would like to attempt some simple cases as they yield important insights about which parameters, such as $\bar{t}_1$, $\bar{t}_2$ and m, are important for describing the directional ACF. Eq. 3.15 reduces to the known result [48] when the dwell-time intervals are Poisson distributed. Moreover, a closed and analytical form of $C(m,t)$ is derived so that an infinite sum of swimming intervals, $m\to\infty$, is feasible.

For the special case of 3-step motility pattern, i.e. run-reverse-flick ($m=1$), we obtained,

$$
\begin{aligned}
C(1,t) &= \frac{1}{\bar{t}_1+\bar{t}_2}\Big(\bar{t}_1 C_1(1,t) + \bar{t}_2 C_2(1,t)\Big) \\
&= \frac{1}{\bar{t}_1+\bar{t}_2}\Big(\bar{t}_1 (F_1 + \alpha f_1 * F_2) + \bar{t}_2 F_2\Big).
\end{aligned}
\tag{3.16}
$$

It is easy to find that

$$
f_1 * F_2 = k_1 \int_0^t dt' e^{-k_1 t'} e^{-k_2(t-t')} = k_1 \frac{e^{-k_1 t} - e^{-k_2 t}}{k_2 - k_1}, \tag{3.17}
$$

we obtain,

$$
C_1(1,t) = e^{-k_1 t} + \frac{\alpha k_1}{k_2-k_1}(e^{-k_1 t} - e^{-k_2 t}). \tag{3.18}
$$

Since $C_2(1,t) = \exp(-k_2 t)$, and $\bar{t}_1 = k_1^{-1}$ and $\bar{t}_2 = k_2^{-1}$ for the Poisson process, application of Eq. (3.16) yields immediately,

$$
C(1,t) = \frac{1}{k_1+k_2}\left(k_2 e^{-k_1 t} + \frac{\alpha k_1 k_2}{k_2-k_1}(e^{-k_1 t} - e^{-k_2 t}) + k_1 e^{-k_2 t}\right). \tag{3.19}
$$

It is reassuring that this result is identical with Eq. (9) in Ref. [48].

It would be interesting to explore the large m limit. This can be best done using the Laplace transformation, which according to the convolution theorem yields,

$$\begin{aligned}\tilde{C}_1(\infty,s) = \tilde{F}_1 + (\alpha\tilde{f}_1)\tilde{F}_2 + (\alpha\tilde{f}_1)(\beta\tilde{f}_2)\tilde{F}_1 + (\alpha\tilde{f}_1)^2(\beta\tilde{f}_2)\tilde{F}_2 \\ + (\alpha\tilde{f}_1)^2(\beta\tilde{f}_2)^2\tilde{F}_1 + ... + (\alpha\tilde{f}_1)^m(\beta\tilde{f}_2)^{m-1}\tilde{F}_2 + ...,\end{aligned} \tag{3.20}$$

and

$$\begin{aligned}\tilde{C}_2(\infty,s) = \tilde{F}_2 + (\beta\tilde{f}_2)\tilde{F}_1 + (\beta\tilde{f}_2)(\alpha\tilde{f}_1)\tilde{F}_2 + (\beta\tilde{f}_2)^2(\alpha\tilde{f}_1)\tilde{F}_1 \\ + (\beta\tilde{f}_2)^2(\alpha\tilde{f}_1)^2\tilde{F}_2 + ... + (\beta\tilde{f}_2)^{m-1}(\alpha\tilde{f}_1)^{m-1}\tilde{F}_2 + ...,\end{aligned} \tag{3.21}$$

where $\tilde{F}_i = (s+k_i)^{-1}$ and $\tilde{f}_i = k_i(s+k_i)^{-1}$. For $m \to \infty$, the infinite sums above yields two simple equations,

$$\tilde{C}_1(\infty,s) = \frac{s + k_2 + \alpha k_1}{(s+k_1)(s+k_2) - \alpha\beta k_1 k_2}, \tag{3.22}$$

and

$$\tilde{C}_2(\infty,s) = \frac{s + k_1 + \beta k_2}{(s+k_1)(s+k_2) - \alpha\beta k_1 k_2}. \tag{3.23}$$

These two equations have the same simple poles with the result: $s_+ = -\bar{k} + \Delta s$ and $s_- = -\bar{k} - \Delta s$, where $\bar{k} = \frac{k_1+k_2}{2}$ and $\Delta s = \frac{1}{2}\sqrt{(k_2-k_1)^2 + 4\alpha\beta k_1 k_2}$. Note that when $(k_2-k_1)^2 + 4\alpha\beta k_1 k_2 \geq 0$, s_+ and s_- are real, and $C_1(\infty,t)$ and $C_2(\infty,t)$, are given by,

$$\tilde{C}_1(\infty,t) = \exp(-\bar{k}t)\left[\cosh(\Delta s t) + \frac{\Delta k + 2\alpha k_1}{2\Delta s}\sinh(\Delta s t)\right], \tag{3.24}$$

$$\tilde{C}_2(\infty,t) = \exp(-\bar{k}t)\left[\cosh(\Delta s t) - \frac{\Delta k - 2\beta k_2}{2\Delta s}\sinh(\Delta s t)\right], \tag{3.25}$$

and

$$\tilde{C}(\infty,t) = \exp(-\bar{k}t)\left[\cosh(\Delta s t) + \frac{\Delta k^2 + 2(\alpha+\beta)k_1 k_2}{2(k_1+k_2)\Delta s}\sinh(\Delta s t)\right], \tag{3.26}$$

where $\Delta k = k_2 - k_1$.

However, when $(k_2 - k_1)^2 + 4\alpha\beta k_1 k_2 < 0$, s_+ and s_- are complex, and $C_1(\infty, t)$ and $C_2(\infty, t)$ are oscillatory and damped with a time constant $\bar{k}^{-1}$. This takes place only when α and β have opposite signs. In this case, $\Delta s = \frac{i}{2}\sqrt{4|\alpha\beta|k_1 k_2 - (k_2 - k_1)^2}$ and the above equations are still valid with the simple replacements of cosh $\rightarrow$ cos and sinh $\rightarrow i\,$sin. The special case is $\alpha = -1$ and $\beta \geq 0$, which is relevant to our experiment. One may also take into account the case when the two roots are degenerate $s_+ = s_-$ or $\Delta s \rightarrow 0$. In this case we have the replacements $\cosh(\Delta s t) \rightarrow 1$ and $\sinh(\Delta s t)/\Delta s \rightarrow t$ as $\Delta s \rightarrow 0$.

Now let us consider a more challenging calculation for m being finite. With m being the number of swimming cycles, we need to keep the first $2m$ term in Eq. 3.20 and the first $2m - 1$ terms in Eq. 3.21, and the resulting sums can be expressed as,

$$\tilde{C}_1(m, s) = \tilde{C}_1(\infty, s)\Big[1 - (\alpha k_1 \tilde{F}_1)^m (\beta k_2 \tilde{F}_2)^m\Big], \tag{3.27}$$

and

$$\tilde{C}_2(m, s) = \tilde{C}_2(\infty, s) - (\alpha k_1 \tilde{F}_1)^{m-1} (\beta k_2 \tilde{F}_2)^m \tilde{C}_1(\infty, s). \tag{3.28}$$

In principle these equations can be inverted to the time domain by the Laplace inverse transformation, but technically it is difficult. As a result we resort to the more tedious but straightforward summation method described by Eq. 3.10 and 3.13. The simply feature of the Poisson process, i.e., $F_i(t) = \exp(-k_i t)$ and $f_i(t) = k_i F_i(t)$ with $i = 1$ and 2, makes it possible to calculate the kernels $c_1(q, t)$ and $c_2(q, t)$ with the result (see mathematical preparations in this section),

$$c_1(q, t) = \frac{(-\alpha\beta k_1 k_2)^{q-1}}{(k_2 - k_1)^{2(q-1)}} \cdot \frac{(2q-2)!}{(q-1)!(q-1)!} \cdot \Big(\exp(-k_1 t) F_1(q, t) - \exp(-k_2 t) F_2(q, t)\Big), \tag{3.29}$$

$$c_2(q, t) = \delta_{q,1} F_1(q, t) + (1 - \delta_{q,1}) \frac{(-\alpha k_1)^{q-2} (\beta k_2)^{q-1}}{(k_2 - k_1)^{2q-3}} \cdot \frac{(2q-4)!}{(q-2)!(q-2)!} \cdot \Big(\exp(-k_1 t) G_1(q, t) - \exp(-k_2 t) G_2(q, t)\Big), \tag{3.30}$$

where $F_i(q,t)$ and $G_i(q,t)$ can be expressed in terms of hypergeometric function ${}_1F_1$ with the result,

$$F_1(q,t) = {}_1F_1\Big(1-q,-2q+3,(k_1-k_2)t\Big) \times \frac{1}{2} + {}_1F_1\Big(1-q,-2q+2,(k_1-k_2)t\Big) \cdot \frac{\alpha k_1}{k_2-k_1}, \tag{3.31}$$

$$F_2(q,t) = {}_1F_1\Big(2-q,-2q+3,(k_2-k_1)t\Big) \times \left(\frac{1}{2} - \delta_{q,1}\right) + {}_1F_1\Big(1-q,-2q+2,(k_2-k_1)t\Big) \cdot \frac{\alpha k_1}{k_2-k_1}, \tag{3.32}$$

$$G_1(q,t) = {}_1F_1\Big(2-q,-2q+4,(k_1-k_2)t\Big) + {}_1F_1\Big(2-q,-2q+3,(k_1-k_2)t\Big) \cdot \frac{\alpha k_1}{k_2-k_1} \cdot \frac{2q-3}{q-1}, \tag{3.33}$$

and

$$G_2(q,t) = {}_1F_1\Big(2-q,-2q+4,(k_2-k_1)t\Big) + {}_1F_1\Big(1-q,-2q+3,(k_2-k_1)t\Big) \cdot \frac{\alpha k_1}{k_2-k_1} \cdot \frac{2q-3}{q-1}. \tag{3.34}$$

Again, with Eq. 3.10 and Eq. 3.13, $C_1(m,t)$ and $C_2(m,t)$ should be averaged using the mean dwelling times k_1^{-1} and k_2^{-1} to find $C(m,t)$, and based on Eq. 3.15 the total correlation function is,

$$C(m,t) = AC_1(m,t) + (1-A)C_2(m,t), \tag{3.35}$$

where $A = k_2/(k_1+k_2)$. This calculation allows us to see whether a finite number of repetitive swimming cycles before directional randomization will enhance anti-correlations and can be used to mimic the experimental observations. We found that when $\beta \geq 0$, the depth of the minimum of the correlation function is always smaller for m being finite as compared to when m is infinite. However, when $\beta < 0$, the depth of the minimum of the correlation function is slightly larger for m being finite as compared to when m be infinite. However, in all cases tested, we did not find that the correlation function can dip below -0.1 and hence we conclude that marine bacteria *V. alginolyticus* swimming is not a Poisson process, which is consistent with our dwell-time measurement reported earlier [48].

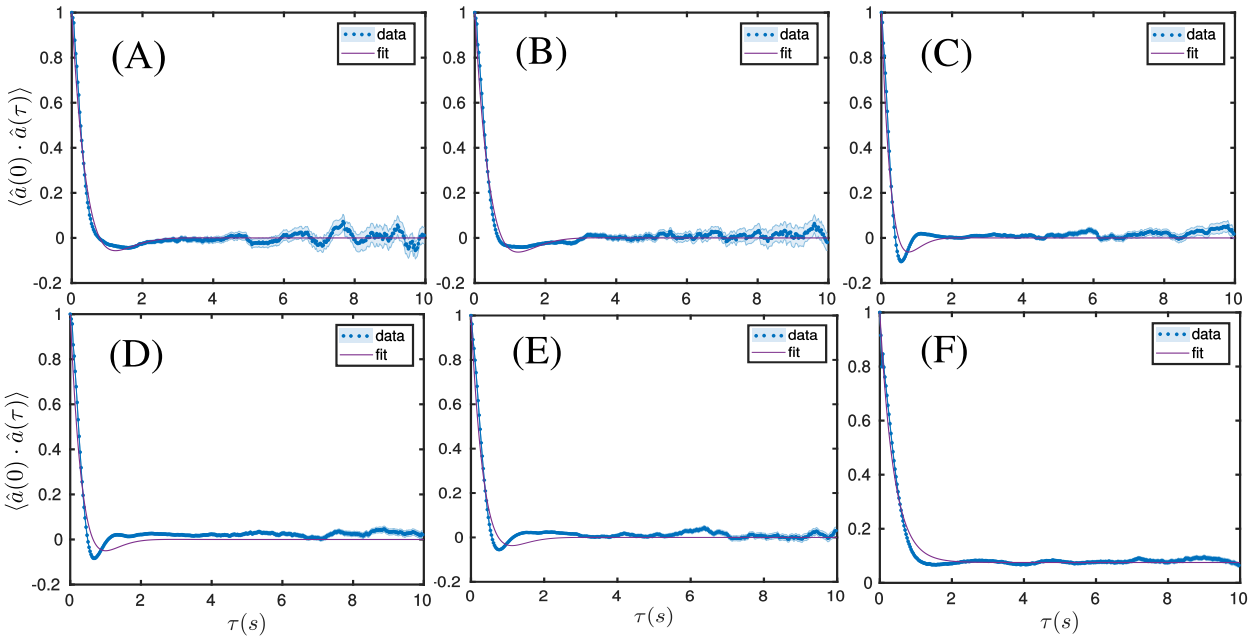

Figure 21: Fitting results of Poisson model, plotted in linear-x scale.

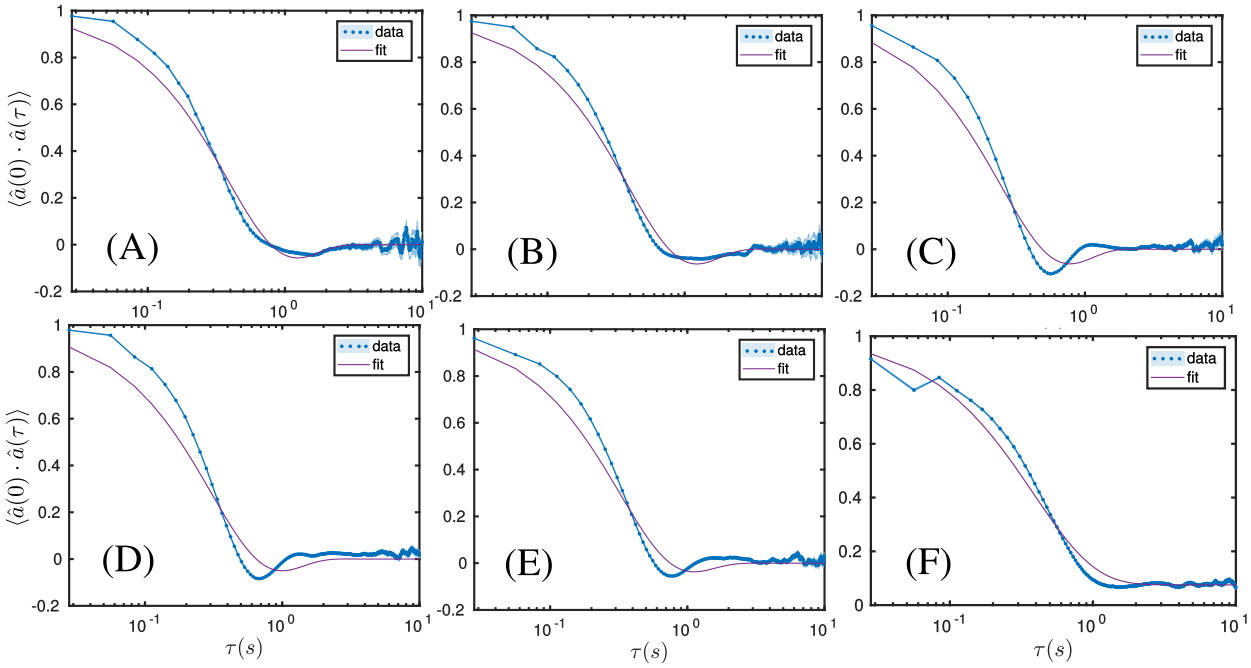

Figure 22: Fitting results of Poisson model, plotted in semilog-x scale.

We also used the model with the Poisson distribution to fit the directional autocorrelation data, which are shown in Fig. 21 and Fig. 22, where the results are plotted in a linear and a semilogx scale, respectively. From these fitting results, it is clearly that the Poisson model is unable to handle both short time scale dynamics and long time behaviors. For short time dynamics, the data shows a clearly flat region but the Poisson model predicts a finite slope for $t \to 0$. The mismatch demonstrates that *V. alginolyticus* adjust their swimming time intervals in a non-Poissonian fashion.

3.3.3 A model with a Gamma distribution

In our earlier experiment [6], we found that the swimming interval distributions of *V. alginolyticus* can be mimicked rather well by various distribution functions, such as inverse Gaussian, log-normal, and Gamma distributions. The essential feature of these distributions is the inhibition of motor reversal in a short time as delineated by Fig. 23. Since the Gamma distribution is mathematically simpler to handle, as the calculation above demonstrates, herein we will use this distribution to mimic our experimental data. Little difference is expected if other distribution functions are used. For a Gamma interval distribution characterized by the shape parameter n and a rate constant k, $f(n,k,t) = k\,(kt)^{n-1}\,\frac{e^{-kt}}{(n-1)!}$, the survival probability is given by

$$F(n,k,t) = 1 - \int_0^t \mathrm{d}t' f(n,k,t') = \exp(-kt) \sum_{j=1}^{n} \frac{(kt)^{n-j}}{(n-j)!}, \tag{3.36}$$

which by itself is a sum of Gamma functions of order $n-j+1$, i.e., $f(n-j+1,k,t)/k$. In our model, n is an integer, k is a rate parameter, and t is interval. n will be replace by μ (ν) to indicate the shape parameter of run (reverse) interval distributions. Following the same definition as for the Poissonian case, we find,

$$c_1(q,t) = \begin{cases} F(\mu,k_1,t), & \text{if } q = 1. \\ (\alpha\beta)^{q-1}\Big[\frac{1}{k_1}\sum_{s=1}^{\mu}\psi(q\mu-s+1,k_1;(q-1)\nu,k_2;t) & \\ +\frac{\alpha}{k_2}\sum_{s=1}^{\nu}\psi(q\mu,k_1;q\nu-s+1,k_2;t)\Big], & \text{for } q > 1. \end{cases} \tag{3.37}$$

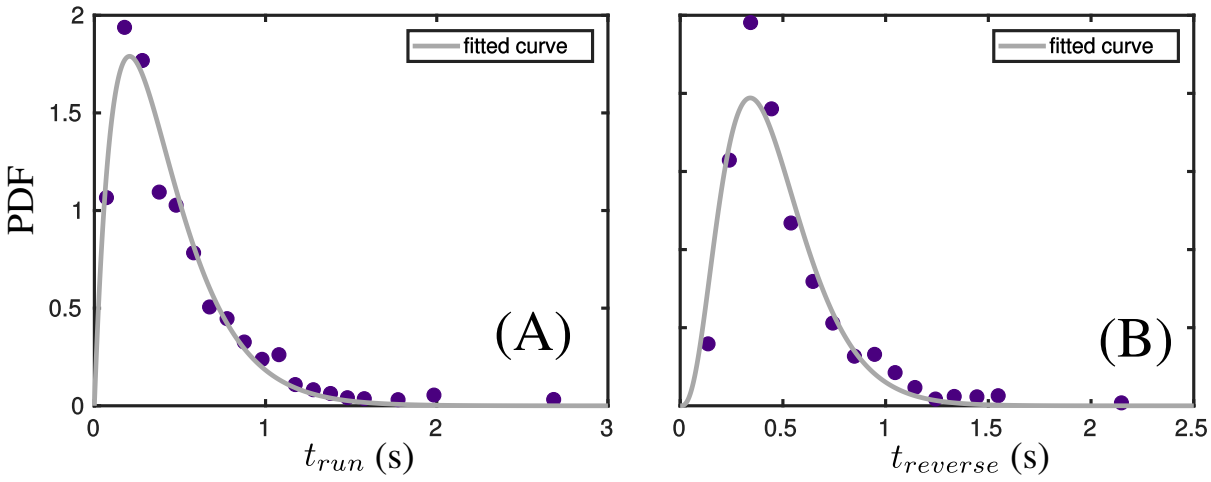

Figure 23: Use the Gamma function to fit the run and reverse time distributions for *V. alginolyticus*. The purple dots are data extracted from Xie's work [6], and the grey lines indicate the fitting results with the Gamma swimming interval distributions. (A) shows the time distribution for run interval. We fixed run shape parameter $\mu = 2$, and the fitting result shows rate constant $k_\mu = 4.8\,\mathrm{s}^{-1}$. The corresponding mean run time can be obtained as $t_\mu = \mu/k_\mu = 0.41\,\mathrm{s}$. Similarly, In (B), the reverse interval distribution has been fitted with its reversal shape parameter $\nu = 4$, and the corresponding rate constant $k_\nu = 8.7\,\mathrm{s}^{-1}$. The mean reversal time is $t_\nu = \nu/k_\nu = 0.46\,\mathrm{s}$.

and

$$c_2(q,t) = \begin{cases} F(\nu, k_2, t), & \text{if } q = 1. \\ (\alpha\beta)^{q-2}\beta\Big[\frac{1}{k_1}\sum_{s=1}^{\mu}\psi((q-1)\mu - s + 1, k_1; (q-1)\nu, k_2; t) & \\ +\frac{\alpha}{k_2}\sum_{s=1}^{\nu}\psi((q-1)\mu, k_1; q\nu - s + 1, k_2; t)\Big], & \text{for } q > 1. \end{cases} \tag{3.38}$$

where (μ, k_1) and (ν, k_2) are the set of parameters associated with the CCW and CW intervals, and $\psi(n_1, k_1; n_2, k_2; t)$ is the convolution of two Gamma functions, $f(n_1, k_1, t)$ and $f(n_2, k_2, t)$, defined in the section of mathematical preparations. For the case of m cycles before randomization, $C_1(m,t) = \sum_{q=1}^{m} c_1(q,t)$ and $C_2(m,t) = \sum_{q=1}^{m} c_2(q,t)$ and total correlation function is given by,

$$C(m,t) = AC_1(m,t) + (1-A)C_2(m,t), \tag{3.39}$$

where $A = \mu k_2/(\mu k_2 + \nu k_1)$.

An extra average is taken since our measurement is in a random ensemble, which means that the starting point can be in any one of the m cycles,

$$\bar{C}(m,t) = \frac{1}{m}\sum_{s=1}^{m}\left[\frac{\mu k_2}{\mu k_2 + \nu k_1}C_1(s,t) + \frac{\nu k_1}{\mu k_2 + \nu k_1}C_2(s,t)\right]. \tag{3.40}$$

Fig. 24 and Fig. 25 show the fitting results when the swimming intervals are modeled by the Gamma distributions. The short time behavior can be reasonably captured by the model, which is missed by the Poisson approximation. For the two starting concentrations, 0% and 0.25%, we observed that there is a mismatch between theory and experiment for the $2 \sim 4$ s interval, which is possibly due to heterogeneity of the cell populations.

Table 2 shows how the parameters change with different concentrations of polymer solutions. We see that $\alpha \approx -1$ for all concentrations, which indicates a purely reversal motion and the values of β are close to zero when $\phi = 0$ and 0.25%. The effect of polymer does not completely show for these two concentrations. Cells are still able to perform the normal run-reverse-flick motility pattern, which means m should be one and $\beta \sim 0$, indicating a randomization of swimming direction at the end of reverse intervals. We keep $m = 1$ for these two concentrations to fit data and the fitting result agrees with the observation. The mean

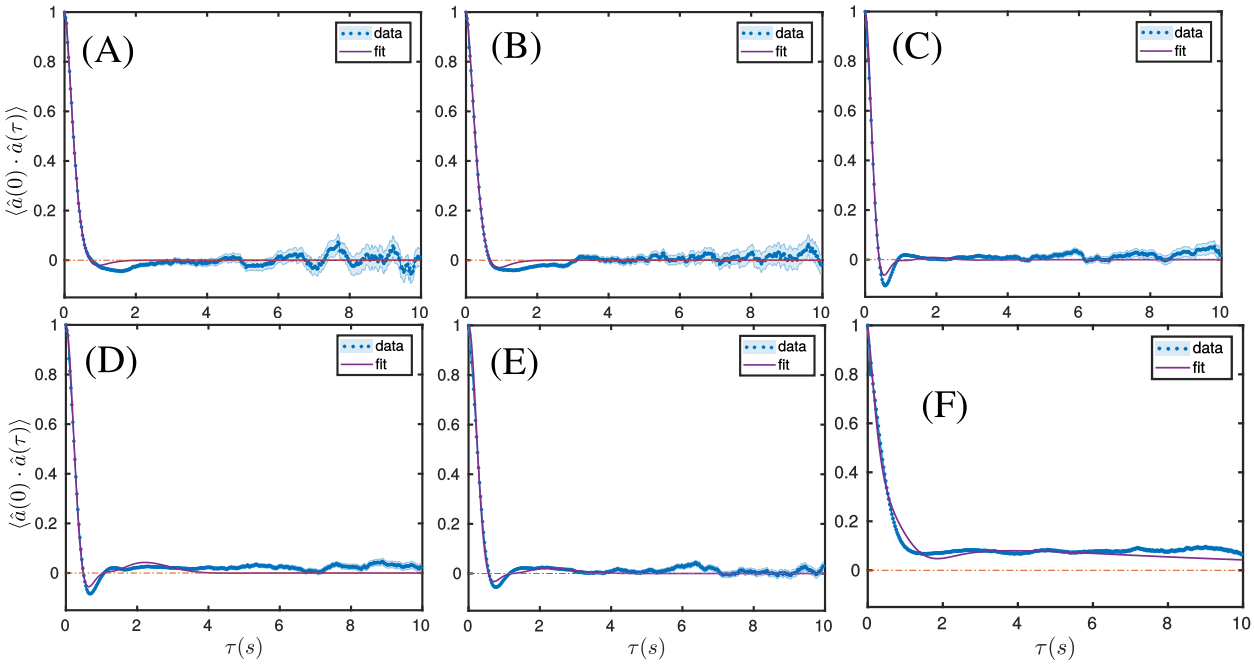

Figure 24: Fitting results using the Gamma model. On these linear-linear plots, the solid blue lines represent the measured directional ACFs and the purple lines are the fitting results using the Gamma model. (A - F) show results with polymer concentrations of 0%, 0.25% 1%, 2.25%, 2.5%, and 5% polymer solutions, respectively.

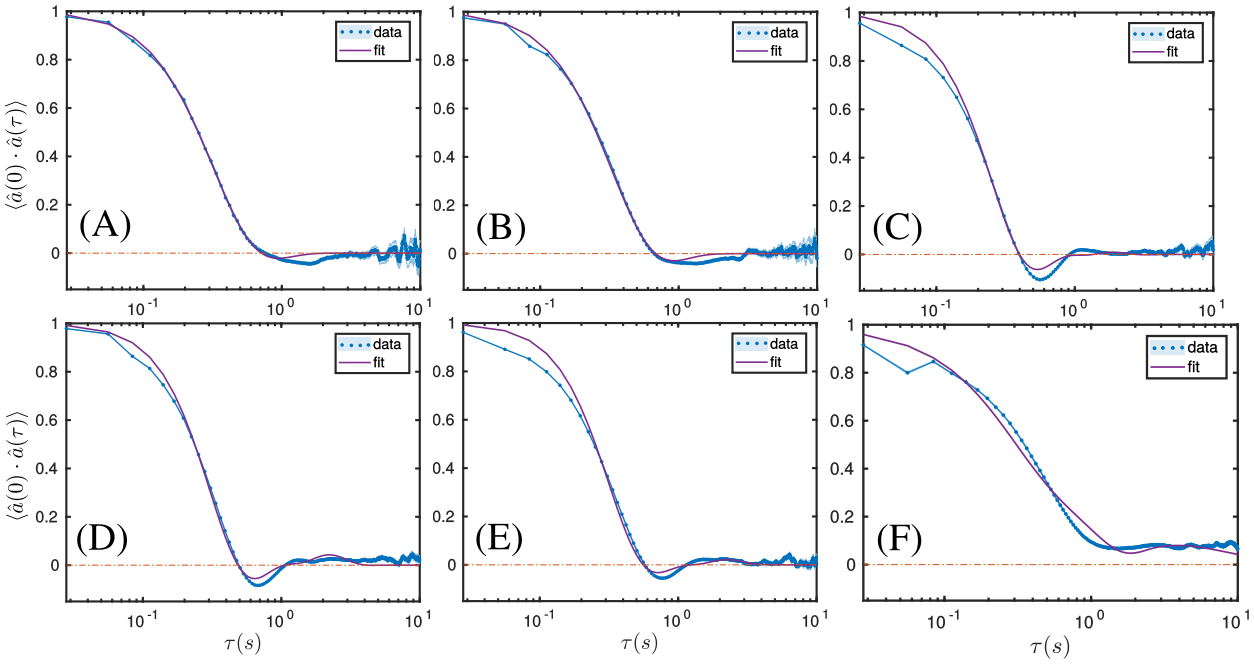

Figure 25: Fitting results using the Gamma model. The same as Fig. 24 but the horizontal axes are logarithmic.

ϕ (%)	α	β	k_1 (Hz)	k_2 (Hz)	μ	ν	m	$\bar{t}_1$ (s)	$\bar{t}_2$ (s)
0	-1.00	0.008	8.13	5.82	2	3	1	0.25	0.52
0.25	-0.99	0.007	7.58	5.80	2	3	1	0.26	0.52
1	-1.00	-0.78	6.48	8.48	2	3	4	0.31	0.47
2.25	-0.99	-1.0	4.34	7.85	2	3	4	0.46	0.38
2.5	-1.00	-0.73	3.92	8.23	2	3	4	0.51	0.36
5	-0.91	-1.0	0.9	5.4	1	2	15	1.1	0.37

Table 2: Fitting results using the Gamma distribution. α and β characterize the persistence of *V. alginolyticus*' swimming. k_1, k_2, μ, and ν are the parameters of the Gamma distribution used in the model. $\bar{t}_1$ and $\bar{t}_2$ indicate the mean run and reverse time, respectively.

run time $\bar{t}_1(\equiv \mu/k_1)$ and reverse time $\bar{t}_2(\equiv \nu/k_2)$ are close to the mean value obtained from Xie's data, which are 0.41 s and 0.46 s, respectively [6]. When the concentration becomes larger, $\phi = 1$, 2.25 and 2.5%, the flick events have been suppressed. The values of β become negative, indicating a reversal-like motion. The motility patterns become a sequence of run and reverse intervals. In our fitting procedure, we find the condition of $m = 4$ could capture this effect. The mean run time $\bar{t}_1$ is getting smaller and the mean reverse time $\bar{t}_2$ is getting bigger for these three concentrations, comparing with the mean times of the beginning two concentrations. In general, the mean run and reverse times are not influenced by the polymer solutions in a obvious way. It seems that the time cells take to finish one swimming cycle is roughly the same for different concentrations. For the highest concentration, the negative correlation in the directional ACF disappears and the motility pattern becomes the run-reverse type. The fitting results show that bacteria need to finish multiple run-reverse motility cycles ($m = 15$) until a very rare flick event happens. The directional ACF remains positive.

3.3.4 Mathematical preparations for the model with Gamma distributions

We will be dealing with Gamma distributions, which have some nice mathematical properties that we would like to discuss and use in the main text. First of all, the Gamma distribution is a series convolution of the Poisson distribution defined as,

$$f(k,t) = ke^{-kt}. \tag{3.41}$$

For an n-fold convolution, denoted as $f^n(k,t)$, one obtains,

$$f^n(k,t) = k\frac{(kt)^{n-1}}{(n-1)!}e^{-kt}, \tag{3.42}$$

which is called nth-order Gamma function. Using the property of the Beta function, $\beta(x,y) = \int_0^1 t^{x-1}(1-t)^{y-1}dt = \Gamma(x-1)\Gamma(y-1)/\Gamma(x+y-1)$, the convolution of two Gamma distributions with the same $k's$ can be found,

$$f^{n_1}(k,t) * f^{n_2}(k,t) = k\frac{(kt)^{n_1+n_2-1}}{(n_1+n_2-1)!}e^{-kt}. \tag{3.43}$$

However, one often encounters situations when the $k's$ are not the same, $k_1 \neq k_2$. In this case, we need the use of hypergeometric functions ${}_1F_1(n_1, n_2, x)$. Let's define the convolution of $f^{n_1}(k_1, t)$ with $f^{n_2}(k_2, t)$ as $\psi(n_1, k_1; n_2, k_2; t)$, it can be shown [49],

$$\psi(n_1, k_1; n_2, k_2; t) = (-1)^{n_1-1} \frac{(n_1+n_2-2)!}{(n_1-1)!(n_2-1)!} \cdot \frac{k_1^{n_1} k_2^{n_2}}{(k_2-k_1)^{n_1+n_2-1}}$$
$$\cdot \Big\{ e^{-k_1 t} {}_1F_1\big(1-n_1, 2-n_1-n_2, (k_1-k_2)\,t\big) - e^{-k_2 t} {}_1F_1\big(1-n_2, 2+n_1+n_2, (k_2-k_1)\,t\big) \Big\}. \tag{3.44}$$

Whereas it is enticing that one can write convolution of two Gamma functions in a closed form given by 3.44, this equation is not robust enough for fitting the experimental data. The problem stems from the fact that when k_1 and k_2 are close, the two terms inside the curly brackets become very small, causing a numerical rounding error of the order of 10^{-15}, which fluctuates as noises. These rounding errors are then amplified by the denominator $(k_2 - k_1)^{n_1+n_2-1}$, which is similarly small when k_1 and k_2 are close. The problem becomes worse when n_1 and n_2 are large. To fix this problem, a better understanding of the convolution integral is needed particularly when $k_2 \to k_1$. We note that $\int \psi(n_1, k_1; n_2, k_2; t)\, \mathrm{d}t = 1$, which suggests $\frac{(n_1+n_2-2)!}{(n_1-1)!(n_2-1)!}(k_1 t_{max}) \frac{k_1^{n_1-1} k_2^{n_2} t^{n_1+n_2-1}\{...\}}{[(k_2-k_1)t]^{n_1+n_2-1}} \sim 1$. For this quantity to have a proper limit when $k_2 \to k_1$, $k_1^{n_1-1} k_2^{n_2} t^{n_1+n_2-1}\{...\} \sim \frac{(n_1-1)!(n_2-1)!}{(n_1+n_2-2)!} \frac{[(k_2-k_1)t]^{n_1+n_2-1}}{k_1 t_{max}} = \epsilon$, where ϵ can be set to the rounding error of the computer, which in our case is $\sim 10^{-15}$ and $t_{max} \approx 10$ s, a time scale relevant to our experiment. This allows us to estimate the range of time t when Eq. 3.44 is applicable, which we found to be,

$$t > t_0 \equiv \frac{1}{|k_2-k_1|} \Big[\epsilon \cdot (k_1 t_{max}) \cdot \frac{(n_1+n_2-2)}{(n_1-1)!(n_2-1)!} \Big]^{\frac{1}{n_1+n_2-1}}. \tag{3.45}$$

For $t < t_0$, the following approximation is used,

$$\psi(n_1, k_1; n_2, k_2; t) \approx \begin{cases} k_1 \frac{(k_1 t)^{n_1-1}(k_2 t)^{n_2}}{(n_1+n_2-1)!} e^{-k_1 t}, & \text{if } n_1 \geq n_2. \\ k_1 \frac{(k_1 t)^{n_1-1}(k_2 t)^{n_2}}{(n_1+n_2-1)!} e^{-k_2 t}, & \text{if } n_1 < n_2. \end{cases} \tag{3.46}$$

This equation yields the proper limit when $k_2 = k_1 = k$ with the result $\psi(n_1, k; n_2, k; t) = f^{n_1+n_2}(k, t)$. The above scheme allows us to calculate convolution of two Gamma functions efficiently and with a high accuracy.

Finally, if the swimming interval distribution is given by a Gamma process with a density $f(\mu, k, t)$, the mean dwell time $\bar{t}$ is given by μ/k and the survival probability $F(\mu, k, t) = 1 - \int_0^t f(\mu, k, t')\,\mathrm{d}t'$ is given by,

$$F(\mu, k, t) = \sum_{l=1}^{\mu} f(\mu - l + 1, k, t)/k. \tag{3.47}$$

For simplicity, we will assume μ to be an integer.

These are basically all we need to calculate the directional ACF for a non-Poisson swimmer.

3.4 A BROWNIAN HARMONIC OSCILLATOR MODEL

In Chapter 1, we show briefly how the velocity ACF of a Brownian harmonic oscillator is obtained. In this section, we try to explain its connection to our experimental observations. One reason motivating us to use the harmonic oscillator model is that the mathematical form of directional ACF in the Poisson model ($\cosh kt + \sinh kt$) has similarity with the velocity ACF of a Brownian particle in a harmonic potential. The advantage of this model is that it offers not only a reasonable agreement with experimental observation but also a clear physics picture, comparing with the phenomenological models of bacterial motility patterns in previous sections.

We re-plot the measured directional ACFs of all polymer concentrations $\leq 5\%$ together in Fig. 26. In the absence of polymers (green dots) the measured directional ACF decays non-monotonically; it passes through a broad minimum at $t \approx 1.05$ s before approaching zero at a long time. Therefore the measured directional ACF is oscillatory in time similar to the response function of a damped harmonic oscillator. The shallowness of the minimum suggests that system is close to the condition of critical damping. We found that this oscillatory behavior is strongly affected by the presence of polymers in the swimming buffer. For too low a concentration, say $\phi = 0.25\%$, its directional ACF is nearly identical to the directional ACF when $\phi = 0$. Unexpectedly, however, we found that there is a range of polymer concentrations in which the oscillation in the autocorrelation is amplified as delineated in

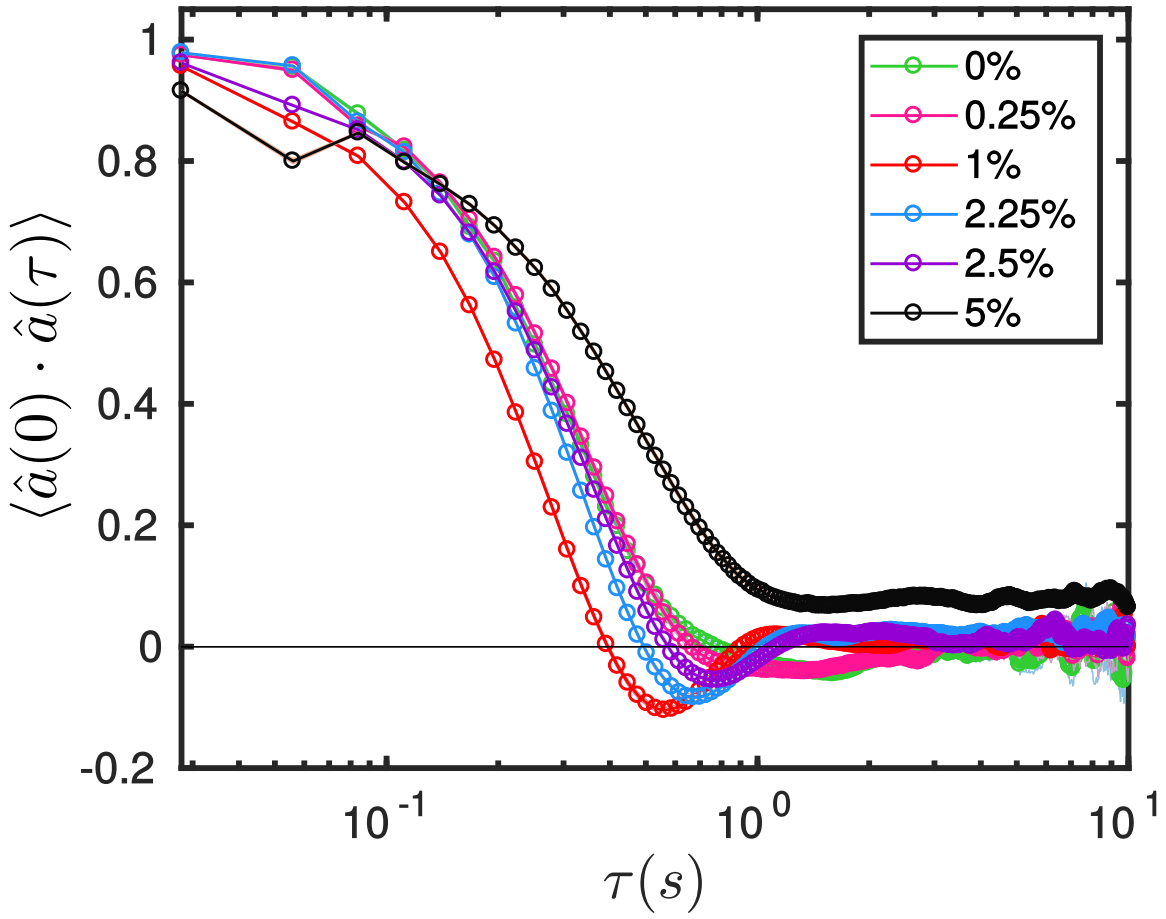

Figure 26: Directional ACFs of 0%, 0.25%, 1%, 2.25%, 2.5% and 5% concentrations of polymer solutions. For comparing the effect of polymer concentrations on bacterial swimming, all the correlation functions are graphed on this single plot, where in increasing polymer concentrations, $\phi = 0, 0.25, 1, 2.25, 2.5$ and 5%, the corresponding correlation functions are plotted in circles of green, pink, blue, purple, and black, respectively. Even without polymers (green circles), the measured directional ACF is oscillatory showing a shallow minimum at $\tau \approx 1$ s. Adding a moderate amount of polymers (a few percent) to the motility buffer has the effects of making the oscillation faster and a larger amplitude (red circles). For polymer concentrations $\phi = 5\%$, the oscillation is completely suppressed (black circles).

Fig. 26 by the red (1%), blue (2.25%), and purple circles (2.5%); in the language of harmonic oscillators, this regime can be classified as underdamped. When the polymer concentration is increased further, such as $\phi = 5\%$ (black circles) in Fig. 26, the oscillation is totally suppressed, and the correlation function cesses to decay in long times. For even higher polymer concentrations, $\phi \geq 5\%$, observations showed that the directional randomization by flicking is significantly suppressed and the motility pattern is the run-reverse type. This gives rise to the residual correlation in the swimming velocity in long times as depicted in the figure.

Usually when polymers are added to a solution, the dominant effect is an increased viscosity that enhances damping of the system. Our observed amplification of the oscillation amplitude, when a small amount of polymers is added, appears quite odd in this light. Inspection of data in Fig. 26 reveals certain regularities as ϕ is increased, i.e., we found that a higher oscillation frequency is associated with a larger oscillation amplitude. Such a behavior is akin to a mechanical oscillator with an intrinsic frequency of ω_0; when coupled to a viscous environment, this frequency drops according to $\omega_0' = \sqrt{\omega_0^2 - (\gamma/2)^2}$, where γ is a damping coefficient. What is surprising however is that there appears to have an optimal polymer concentration at which the system is close to resonance with the greatest oscillation amplitude.

To appreciate what we have observed, it is useful to recall how bacterial motion is generated. The microorganisms swim by rotating helical flagella driven at their bases by molecular motors. The direction of motor rotation is controlled by an internal network known as chemotaxis network. For *E. coli* under a neutral condition (unstimulated), the motor fluctuations between CCW and CW states as a result of concentration fluctuations of the regulator protein, CheY-P, that binds to the motor complex. Studies have shown that the interval length of these states is Poisson distributed with the mean for the CCW (run) state $\sim$ 1 s and the CW (tumbling) state $\sim$ 0.1 s. Over a long time, the trajectory of a bacterium is akin to the motion of a "massive" particle with the particle's inertia playing the role of persistent in a run and random kickings by surrounding molecules playing the role of a tumble. The symmetry of marine bacterial swimming presented above suggests that the response of the polar flagellar motor to CheY-P is different from an *E. coli*'s motor.

Herein we would like to promote the idea that the polar flagellar motor is internally driven by a (noisy) oscillator, and the behavior of such an oscillator is influenced by the viscoelastic properties of the surrounding medium.

3.4.1 A Brownian harmonic oscillator behavior of motility patterns of *V. alginolyticus* in buffers

During our measurements, we gradually realized that the internal degree of freedom driving the *V. alginolyticus* movement in motility buffers could be approximated by a harmonic oscillator. By assigning values of "+1" to run intervals and "−1" to reverse intervals, which means we only account for cells' swimming directions in a time series, random telegraph-like time series can be obtained and their time correlations functions can be well approximated by a harmonic oscillator subject to a white noise [32] [50]. The ensemble averaged correlation function for individual cell to a high precision can be described by

$$C(t) = \frac{\cos(\Omega_0 t - \Phi_0)}{\cos\Phi_0} e^{-\Gamma_0 t}, \tag{3.48}$$

where Ω_0, Φ_0 and Γ_0 are the characteristic parameters for the cell population. Here, $1/\Gamma_0$ describes the damping time, Ω_0 is the oscillation frequency, and $\Phi_0 = \cos^{-1}\left[1 + (\Omega_0/\Gamma_0)^2\right]^{-1/2}$ is the phase shift.

A Langevin equation can be used to describe cell motion here. We notice that the random forcing term on the right-hand side of Eq. 1.10 should not be a Gaussian white noise since the cell is driven by molecular motors rather than thermal noise, so Eq. 1.10 should be changed to,

$$\frac{\mathrm{d}}{\mathrm{d}t}\vec{v}(t) = -\gamma\vec{v}(t) + \frac{\vec{F}(t)}{m}, \tag{3.49}$$

where $\gamma = \frac{6\pi\eta a}{m}$ is the damping term for a swimming cell of an effective mass m and radius a, and $\vec{F}$ is the thrust force. Additional terms may be added to the right-hand side of Eq. 3.49 to account for thermal fluctuations and active directional randomization. These effects serve to enhance the rate of decay, making Γ_0 in Eq. 3.49 larger. Ignoring these details, we expect that the thrust force should have the property $\langle\vec{F}\rangle = 0$, but $\langle\vec{F}(0)\cdot\vec{F}(t)\rangle \neq 0$.

The behaviors of flagellar motors are controlled by the chemotaxis network. For the chemotaxis network of *E. coli*, the motor fluctuation between CCW and CW states is due to concentration fluctuations of the regulator protein, CheY-P, that binds to the motor complex. The marine bacteria *V. alginolyticus* we used is different from that of *E. coli* in the sense that the marine bacteria has a symmetric run-reverse period. While the details of how the bacteria behave in an oscillatory fashion is unknown, an internal variable, such as CheY-P concentration, that oscillates in time may not be surprising because a variety mechanism can give rise to such a behavior; such as the existence of a feedback loop in the chemotaxis network or simply a delayed reaction at the motor level will do [51]. We assume that the noisy force at the motor level follows

$$C_f(t) = \langle \frac{\vec{F}(t)}{m} \cdot \frac{\vec{F}(0)}{m} \rangle = \langle \vec{f}(t) \cdot \vec{f}(0) \rangle = (F/m)^2 \frac{\cos(\Omega_0 t - \Phi_0)}{\cos \Phi_0} e^{-\Gamma_0 t}, \tag{3.50}$$

as seen in Xie et al.'s experiment [32]. We have $\vec{f}(t) = \frac{\vec{F}(t)}{m}$ in the equation above. Additionally, people typically use a memory time rather than an effective mass to account for persistent swimming, but the net effects are the same [52]. For our problem, the external parameters are much faster than the internal parameters with the result $\gamma \gg \Gamma_0$ or Ω_0, so these two sets of time scales are well separated. In this sense, the velocity ACF from Eq. 3.49 has the same mathematical form (see derivation) as the force ACF,

$$C_v(t) = v_{sm}^2 \frac{\cos(\Omega_0 t - \Phi_0)}{\cos(\Phi_0)} e^{-\Gamma_0 t}, \tag{3.51}$$

where $v_{sm}^2 = f/2\gamma$ is the swimming speed of a bacterium. A non-linear least square fitting to the buffer data shows that $\Omega_0 = 3.41$ rad/s, $\Phi_0 = 0.85$ rad, and $\Gamma_0 = 4.40$ s^{-1} and it is plotted in Fig. 27. The closeness of Ω_0 and Γ_0 suggests that the internal oscillator operates near the critical damping condition.

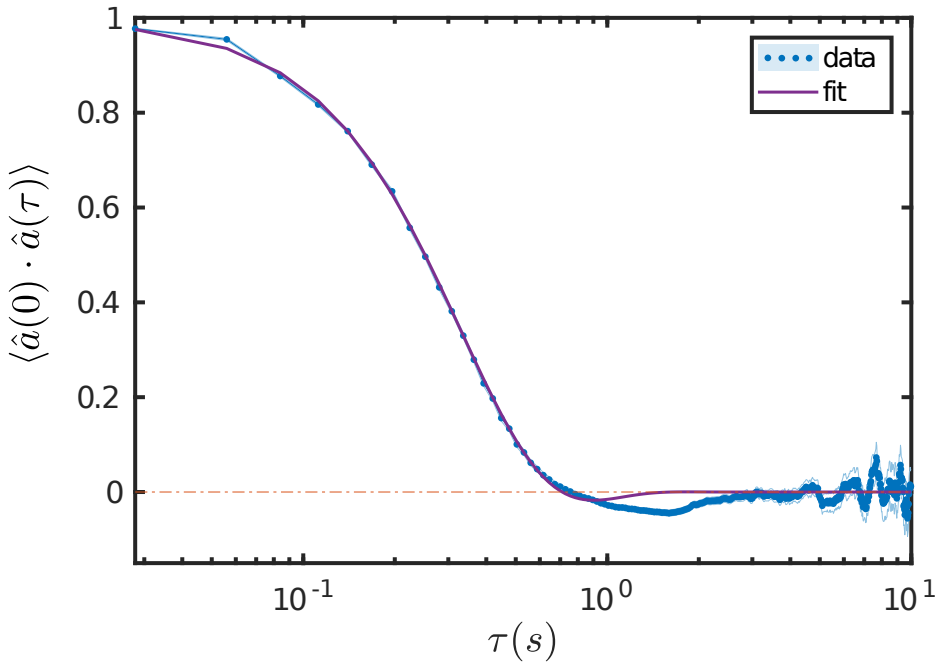

Figure 27: The fitting result of the harmonic oscillator model for *V. alginolyticus* swimming in the motility buffer. The parameters obtained are $\Omega_0 = 3.41$ rad/s, $\Phi_0 = 0.85$ rad, and $\Gamma_0 = 4.4$ s^{-1}. The deviation of data and the prediction between 1 s and 2.5 s is likely due to the heterogeneity of the bacteria population.

3.4.2 Polymer's viscoelastic effect

When polymers are added to the motility buffer, a swimming bacteria in the polymer medium not only feels the viscous force but also an elastic force. Based on our calculation, the overlapping concentration of polymer solutions ϕ^* is around 1%, which marks the onset of viscoelasticity in the medium, and beyond which both the viscosity and elasticity increase rapidly with ϕ. Polymer physics tells us that the shear modulus (viscosity, the dissipative part) grows faster than the storage modulus (elasticity, non-dissipative part) as a function of ϕ [46]. A good approximation of this system is to add a restoring-force term in Eq. 3.49, and the resulting equation then mimics a damped harmonic oscillator,

$$\frac{\mathrm{d}}{\mathrm{d}t}\vec{v}(t) = -\omega_0^2\vec{r}(t) - \gamma\vec{v}(t) + \vec{f}(t). \tag{3.52}$$

The velocity ACF can be calculated and the result in Eq. 3.53 shows that the extra restoring force only adds an additional phase shift $\Delta\Phi$ to Eq. 3.51, leaving the internal variables Ω_0, Φ_0 and Γ_0 unchanged,

$$\begin{aligned} C_v(t) &= e^{-\Gamma_0 t}\left[\left(1 - \frac{A\left(A-\Gamma_0\right)}{\left(A-\Gamma_0\right)^2+\Omega_0^2}\right)\cos\left(\Omega_0 t - \Phi_0\right) - \frac{A\Omega_0}{\left(A-\Gamma_0\right)^2-\Omega_0^2}\sin\left(\Omega_0 t - \Phi_0\right)\right] \\ &= C_0\left(A,\Gamma_0,\Omega_0\right)e^{-\Gamma_0 t}\cos\left(\Omega_0 t - \Phi_0 + \Delta\Phi\right). \end{aligned} \tag{3.53}$$

Since the set of parameters Γ_0, Φ_0 and Ω_0 characterizes the cell behavior, we try to fix these parameters but only allow $\Delta\Phi$ to be the adjustable parameter. As the green dashed lines in Fig. 28 shows, the model cannot fit the data in this case and the values of the corresponding parameter $\Delta\Phi$ is shown in Table 3. This implies that the internal variables Γ_0, Φ_0 and Ω_0 are changed in response to the polymers. Getting rid of the constraint on the fitting procedure, the data for different concentrations of polymers can be reasonably fitted by the model, which are shown by purple solid lines in Fig. 28. For the final concentration (5%), the oscillation part $\cos(\Omega_0 t - \Phi_0)$ in the correlation function changes into $\cosh(\Omega_0 t - \Phi_0)$ since both Ω_0 and Φ_0 turn imaginary. In this case, oscillations of the correlation function disappear.

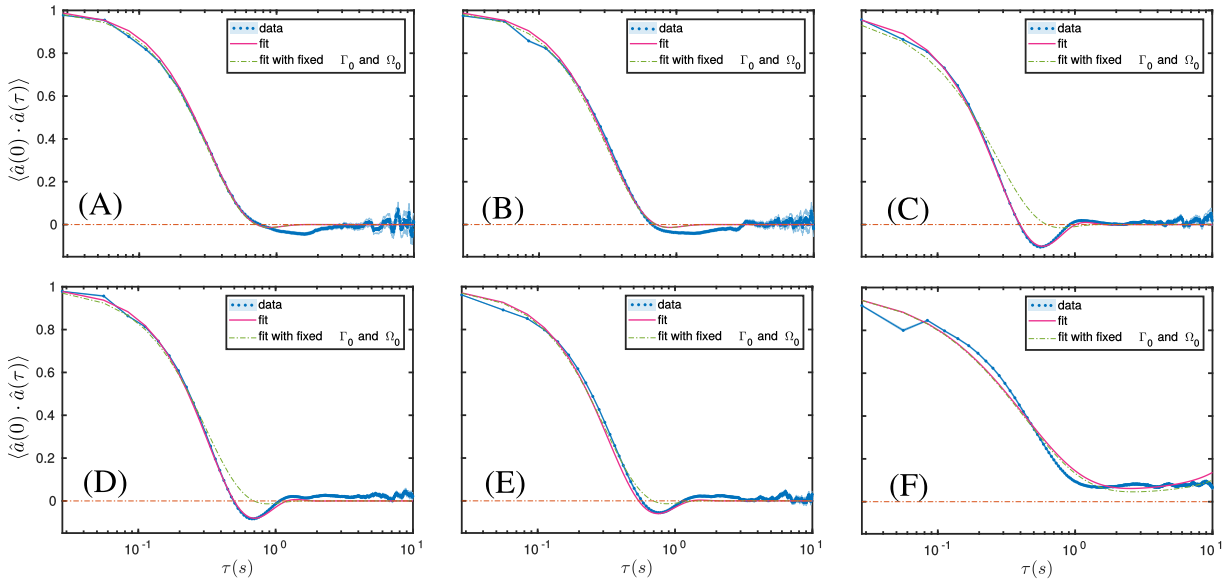

Figure 28: Damped harmonic oscillator model fitting results. The velocity ACFs $C_v(t)$ are normalized, $C(t) \equiv C_v(t)/v_{sm}^2$, and plotted for concentrations $\phi = 0\%$ (A), 0.25% (B), 1% (C), 2.25% (D), 2.5% (E) and 5% (F). The green dashed lines are fits to the model assuming that internal variables, such as $\Omega_0 = 3.41$ rad/s, $\Phi_0 = 0.85$ and $\Gamma_0 = 4.4$ s^{-1}, are fixed and the effect of polymers only changes the phase $\Delta\Phi$ of the correlation function. The fitting procedure shows that the assumption is not good enough, especially when oscillation amplitudes are large, such as (D) and (E). This indicates that the influence from environment does change internal variables. After we eliminate the restriction on the internal parameters, a much better agreement is found, which is shown by purple curves. The result of the fitting procedure is given in Table 4. It is seen that for large polymer concentrations, such as (F), the ACF decays monotonically in time and the functional dependence changes into $C(t) \propto \cosh(\Omega_0 t - \Phi_0) \exp(-\Gamma_0 t)$.

ϕ (%)	0	0.25	1	2.25	2.5	5
$\Delta\Phi$ (rad)	0	0.2	0.39	0.24	0.23	-0.68

Table 3: Results of fitting with fixed Ω_0, Γ_0 and Φ_0. Here we assume that polymer does not affect the internal valuables, Ω_0 and Γ_0, as well as the phase of oscillation Φ_0. Their values are fixed and the effect of added polymer is to change the phase of oscillations, $\Delta\Phi$.

The fitting parameters are listed in Table 4 and plotted in Fig. 29. It shows that both Ω and $\Phi = \Phi_0 - \Delta\Phi$ reaches extrema when $\phi \approx 1\%$, where Ω has a peak and Φ reaches the minimum value, but Γ appears to decay monotonically with ϕ. The latter may be expected because Γ, as discussed earlier, can be effected by bacterial motility pattern. As the polymer concentration increases, bacterial gradually lose their ability to flick and hence Γ is reduced.

It is curious that polymer concentrations in the neighborhood of 1% have a large "resonance-like" effect on marine bacterial swimming. What is special about these concentrations? The following analysis provides a useful clue. In the simple model where one assumes that the internal oscillator of a bacterium is rigid with fixed Ω_0 and Γ_0, the additional phase shift $\Delta\Phi$ resulting from exterior viscoelastic medium is proportional to ω_0^2/γ. Since $\gamma = 6\pi a\eta/m$ and $\omega_0^2 = k/m$, where m is the effective mass of the bacterium and k is the effective spring constant of the polymer matrix. k should be proportional to the plateau modulus, and it follows $\Delta\Phi \sim k/\eta \sim G_N^{(0)}(\phi)/\eta(\phi)$, where $G_N^{(0)}$ is the plateau modulus. Based on Ref. [46], it is shown that the following scaling,

$$G_N^{(0)}(\phi) = \frac{\phi}{N} k_B T \left(\frac{\phi}{\phi^*}\right)^{\frac{1}{3\nu-1}} \propto \left(\frac{\phi}{\phi^*}\right)^{\frac{3\nu}{3\nu-1}}, \tag{3.54}$$

and

$$\eta(\phi) \approx \eta_s \left[1 + \left(\frac{\phi}{\phi^*}\right)^{\frac{3}{3\nu-1}}\right], \tag{3.55}$$

where N is the number of monomers in a polymer chain. According to this simple model, therefore, $\Delta\Phi$ vanishes for both $\phi \ll \phi^*$ and $\phi \gg \phi^*$, indicating that there is a maximum

ϕ (%)	Ω (rad/s)	Γ (s^{-1})	Φ (rad)
0	3.4 ± 0.5	4.4 ± 0.4	0.9 ± 0.2
0.25	3.4 ± 0.3	3.5 ± 0.4	0.7 ± 0.1
1	5.1 ± 0.3	3.8 ± 0.6	0.46 ± 0.02
2.25	4.4 ± 0.5	3.5 ± 0.4	0.61 ± 0.06
2.5	4.0 ± 0.5	3.6 ± 0.4	0.62 ± 0.09
5	1.2 ± 0.3	1.1 ± 0.1	1.5 ± 0.2

Table 4: Results of fitting without fixing Ω_0, Γ_0, and Φ_0. Here we assume that polymers affect the internal valuables, Ω and Γ, as well as the phase of the oscillation $\Phi = \Phi_0 - \Delta\Phi$.

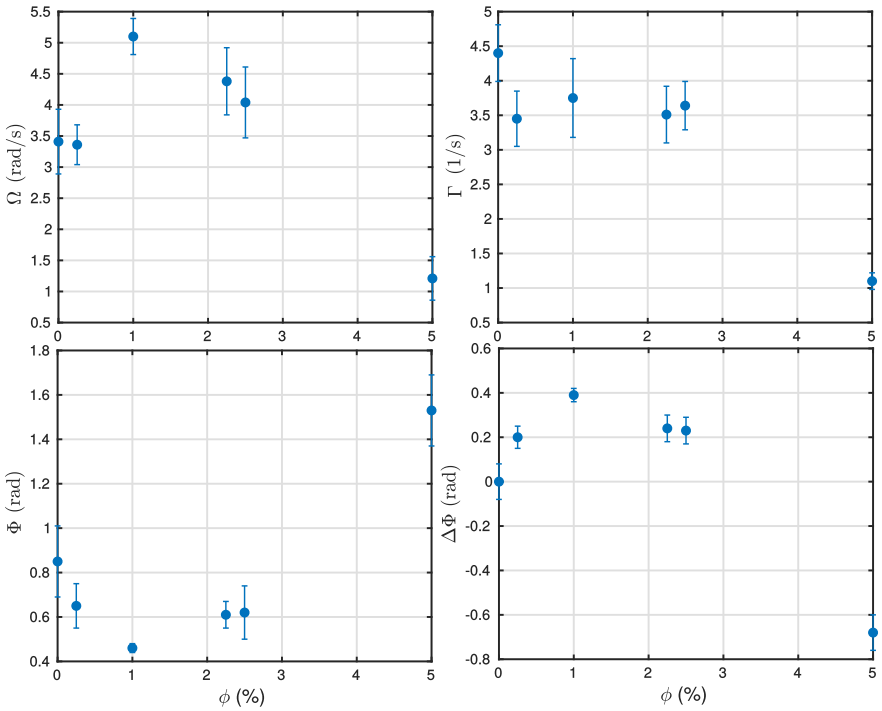

Figure 29: Fitting parameters vs. concentrations. Both Ω and Φ have extrema (Ω reaches the maximum value but Φ reaches the minimum value.) at $\phi \approx 1\%$ but Γ decreases monotonically as the polymer concentration ϕ is increased. The latter is expected because swimming direction randomization is suppressed by the polymer.

added phase shift $\Delta\Phi_{max}$. We note that the effect of $\Delta\Phi$ is to reduce Φ_0, i.e., $\Phi = \Phi_0 - \Delta\Phi$, and effectively makes the system closer to resonance. We also noticed that $\Delta\Phi_{max}$ occurs at a polymer concentration ϕ_0 obeying the equation,

$$\phi_0 \approx \phi^* \left(\frac{\nu}{1-\nu}\right)^{\frac{3\nu-1}{3}}. \tag{3.56}$$

For $\nu = 0.6$, we find $\phi_0/\phi^* \approx 1.1$, i.e., about 10% above ϕ^*. Using statistics of polymer physics and available data for our PVP polymer, ϕ^* is close to $\sim 1\%$, which is consistent with the resonance-like condition observed. Importantly this analysis suggests that ϕ^* is special for coupling to a harmonic oscillator due to the emergence of an elastic compenent of the fluid but its viscosity still remains relatively low.

3.4.3 Mathematical details for the harmonic oscillator model

Let's focus on the Langevin equations in one dimension for simplicity. Higher dimension can be obtained accordingly.

(i) Viscous case

In Fourier space, Eq. 3.49 becomes

$$i\omega\tilde{v}(\omega) = -\gamma\tilde{v}(\omega) + \tilde{f}(\omega), \tag{3.57}$$

$$\tilde{v}(\omega) = \frac{\tilde{f}(\omega)}{i\omega + \gamma}, \tag{3.58}$$

$$\tilde{S}_v(\omega) = \frac{\tilde{S}_f(\omega)}{\omega^2 + \gamma^2}, \tag{3.59}$$

The mobility function is

$$M_v(t) = \frac{1}{2\gamma} e^{-\gamma|t|}. \tag{3.60}$$

So the velocity ACF becomes ($t > 0$)

$$C_v(t) = M_v(t) * \left(\frac{F}{m}\right)^2 \frac{\cos(\Omega_0 t - \Phi_0)}{\cos(\Phi_0)} e^{-\Gamma_0 t} = \frac{1}{2\gamma} e^{-\gamma t} * f^2 \frac{\cos(\Omega_0 t - \Phi_0)}{\cos(\Phi_0)} e^{-\Gamma_0 t}, \tag{3.61}$$

where $f = \frac{F}{m}$.

It is equal to

$$\begin{aligned} C_v(t) &= \frac{f^2}{2\gamma\cos\Phi_0}\frac{1}{\sqrt{(\gamma-\Gamma_0)^2+\Omega_0^2}}\Bigg\{\Bigg[\cos(\Omega_0 t-\Phi_0)\cos\psi+\sin(\Omega_0 t-\Phi_0)\sin\psi\Bigg]e^{-\Gamma_0 t} \\ &- \Bigg[\cos\Phi_0\cos\psi-\sin\Phi_0\sin\psi\Bigg]e^{-\gamma t}\Bigg\} \\ &= \frac{f^2}{2\gamma\cos\Phi_0}\frac{1}{\sqrt{(\gamma-\Gamma_0)^2+\Omega_0^2}}\Bigg[\cos(\Omega_0 t-\Phi_0-\psi)e^{-\Gamma_0 t}+\cos(\Phi_0+\psi)e^{-\gamma t}\Bigg], \end{aligned} \tag{3.62}$$

where $\cos\psi = \frac{\gamma-\Gamma_0}{\sqrt{(\gamma-\Gamma_0)^2+\Omega_0^2}}$. With the condition of $\gamma \gg \Gamma_0$ and Ω_0, we have that $\psi \to 0$ and $\cos\psi \to 1$. The Eq. 3.62 thus is simplified into

$$C_v(t) = \frac{f^2}{\cos\Phi_0}\frac{1}{2\gamma^2}\Bigg[\cos(\Omega_0 t-\Phi_0)e^{-\Gamma_0 t}\Bigg]. \tag{3.63}$$

(ii) Viscoelastic case

In Fourier space, Eq. 3.52 becomes

$$i\omega\tilde{v}(\omega) = -\omega_0^2\tilde{r}(\omega)-\gamma\tilde{v}(\omega)+\tilde{f}(\omega), \tag{3.64}$$

where $\gamma = 6\pi\eta a/m$, and

$$i\omega\tilde{r}(\omega) = \tilde{v}(\omega). \tag{3.65}$$

The position of the cell $r(t)$ in Fourier space is

$$\tilde{r}(\omega) = \frac{1}{\omega_0^2-\omega^2+i\omega\gamma}\tilde{f}(\omega) = \tilde{M}_r(\omega)\tilde{f}(\omega), \tag{3.66}$$

where $\tilde{M}_r(\omega)$ is the mobility function. Like what we have done in Chapter 1, we hope to calculate $\tilde{S}_r(\omega)$, which is

$$\tilde{S}_r(\omega) = |\tilde{M}_r(\omega)\tilde{f}(\omega)|^2 = \frac{1}{(\omega^2-\omega_0^2)^2+(\gamma\omega)^2}|\tilde{f}(\omega)|^2, \tag{3.67}$$

and then in time domain we have

$$C_r(t) \equiv \langle r(t)r(0)\rangle = \frac{1}{2\omega_0^2\gamma}e^{-\frac{\gamma}{2}t}\Bigg[\cos(\omega_0' t)+\frac{\gamma}{2\omega_0'}\sin(\omega_0' t)\Bigg] * C_f(t), \tag{3.68}$$

where $\omega_0' = \sqrt{\omega_0^2 - (\frac{\gamma}{2})^2}$. Suppose the cell is only driven by thermal noise, $C_f(t) \equiv c = \frac{2k_BT\gamma}{m}$,

$$C_r(t) = \frac{c}{2\omega_0^2\gamma} e^{-\frac{\gamma}{2}t} \left[\cos(\omega_0' t) + \frac{\gamma}{2\omega_0'} \sin(\omega_0' t) \right], \tag{3.69}$$

The mean squared displacement $R(t)$ is

$$\begin{aligned} R(t) &= \langle (r(t) - r(0))(r(t) - r(0)) \rangle = 2\langle r^2(0) \rangle - 2\langle r(t) r(0) \rangle \\ &= \frac{c}{\omega_0^2 \gamma} \left[1 - e^{-\frac{\gamma}{2}t} \left(\cos \omega_0' t + \frac{\gamma}{2\omega_0'} \sin \omega_0' t \right) \right]. \end{aligned} \tag{3.70}$$

The diffusion coefficient $D(t)$ and velocity ACF can be calculated below [53], which is

$$D(t) = \frac{1}{2} \frac{\mathrm{d}R(t)}{\mathrm{d}t} = \frac{c}{2\omega_0^2\gamma} e^{-\frac{\gamma}{2}t} \left(\frac{\gamma^2}{4\omega_0'} + \omega_0' \right) \sin \omega_0' t, \tag{3.71}$$

and

$$C_v(t) = \frac{\mathrm{d}D(t)}{\mathrm{d}t} = \frac{c}{2\omega_0'\gamma} e^{-\frac{\gamma}{2}t} \left[\omega_0' \cos \omega_0' t - \frac{\gamma}{2} \sin \omega_0' t \right]. \tag{3.72}$$

From Eq. 3.72, we know that the $M_v(t)$ is

$$\begin{aligned} M_v(t) &= \frac{1}{2\omega_0'\gamma} e^{-\frac{\gamma}{2}t} \left[\omega_0' \cos \omega_0' t - \frac{\gamma}{2} \sin \omega_0' t \right] \\ &= \frac{e^{-\frac{\gamma}{2}t}}{2\gamma} \frac{\cos(\omega_0' t + \phi_0)}{\cos \phi_0}, \end{aligned} \tag{3.73}$$

where $\cos \phi_0 = \frac{\omega_0'}{\sqrt{\omega_0'^2 + (\frac{\gamma}{2})^2}}$.

Then we replace the Gaussian noise with the flagellar motor thrust force, and the $C_f(t)$ becomes $(\frac{F}{m})^2 e^{-\Gamma_0 t} \frac{\cos(\Omega_0 t - \Phi_0)}{\cos \Phi_0}$, where $\cos \Phi_0 = \frac{\Omega_0}{\sqrt{\Omega_0^2 + \Gamma_0^2}}$. The velocity ACF in this case is

$$\begin{aligned} C_v(t) &= \int_0^t M_v(t' - t) C_f(t') \, \mathrm{d}t' \\ &= \left(A_m e^{-\frac{\gamma}{2}t} \cos(\omega_0' t + \phi) \right) * \left(A_{ff} e^{-\Gamma_0 t} \cos(\Omega_0 t - \Phi_0) \right), \end{aligned} \tag{3.74}$$

where $A_m = \frac{1}{2\gamma}\frac{1}{\cos\phi_0}$ and $A_{ff} = \frac{(F/m)^2}{\cos\Phi_0}$. By calculating the convolution, we have

$$
\begin{aligned}
C_v(t) = {} & \frac{\frac{1}{2}A_m A_{ff}}{(\frac{\gamma}{2}-\Gamma_0)^2+(\omega_0'+\Omega)^2}\Big\{(\frac{\gamma}{2}-\Gamma_0)\left[\cos(\Omega_0 t-\phi_0-\Phi_0)e^{-\Gamma_0 t}-\cos(\omega_0' t+\phi_0+\Phi_0)e^{-\frac{\gamma}{2}t}\right] \\
& +(\omega'+\Omega_0)\left[\sin(\Omega_0 t-\phi_0-\Phi_0)e^{-\Gamma_0 t}+\sin(\omega_0' t+\phi_0+\Phi_0)e^{-\frac{\gamma}{2}t}\right]\Big\} \\
& +\frac{1}{(\frac{\gamma}{2}-\Gamma_0)^2+(\omega_0'-\Omega)^2}\Big\{(\frac{\gamma}{2}-\Gamma_0)\left[\cos(\Omega_0 t+\phi_0-\Phi_0)e^{-\Gamma_0 t}-\cos(\omega_0' t+\phi_0-\Phi_0)e^{-\frac{\gamma}{2}t}\right] \\
& -(\omega'-\Omega_0)\left[\sin(\Omega_0 t+\phi_0-\Phi_0)e^{-\Gamma_0 t}-\sin(\omega_0' t+\phi_0-\Phi_0)e^{-\frac{\gamma}{2}t}\right]\Big\}.
\end{aligned}
\tag{3.75}
$$

Calculate the convolution in Eq. 3.75.

$$
\begin{aligned}
C_v(t) &= A_m A_{ff}\int_0^t e^{-\frac{\gamma}{2}(t-t')}\cos\left(\omega_0'(t-t')+\phi_0\right)e^{-\Gamma_0 t'}\cos\left(\Omega_0 t'-\Phi_0\right)\mathrm{d}t' \\
&= \frac{A_m A_{ff}e^{-\frac{\gamma}{2}t}}{2}\int_0^t e^{(\frac{\gamma}{2}-\Gamma_0)t'}\left\{\cos\left[\omega_0'(t-t')+\phi_0-\Omega_0 t'+\Phi_0\right]+\cos\left[\omega_0'(t-t')+\phi_0+\Omega_0 t'-\Phi_0\right]\right\}\mathrm{d}t' \\
&= \frac{A_m A_{ff}e^{-\frac{\gamma}{2}t}}{2}\int_0^t e^{(\frac{\gamma}{2}-\Gamma_0)t'}\left\{\cos\left[\omega_0' t+\phi_0+\Phi_0-(\omega_0'+\Omega_0)t'\right]+\cos\left[\omega_0' t+\phi_0-\Phi_0-(\omega_0'-\Omega_0)t'\right]\right\}\mathrm{d}t' \\
&= \frac{A_m A_{ff}e^{-\frac{\gamma}{2}t}}{2}\int_0^t e^{(\frac{\gamma}{2}-\Gamma_0)t'}\left\{\cos\left[(\omega_0'+\Omega_0)t'-\omega_0' t-\phi_0-\Phi_0\right]+\cos\left[(\omega_0'-\Omega_0)t'-\omega_0' t-\phi_0+\Phi_0\right]\right\}\mathrm{d}t' \\
&= \frac{A_m A_{ff}e^{-\frac{\gamma}{2}t}}{2}\times \\
&\Bigg\{e^{(\frac{\gamma}{2}-\Gamma_0)t'}\frac{(\frac{\gamma}{2}-\Gamma_0)\cos\left[(\omega_0'+\Omega_0)t'-\omega_0' t-\phi_0-\Phi_0\right]+(\omega_0'+\Omega_0)\sin\left[(\omega_0'+\Omega_0)t'-\omega_0' t-\phi_0-\Phi_0\right]}{(\frac{\gamma}{2}-\Gamma_0)^2+(\omega_0'+\Omega_0)^2} \\
&+e^{(\frac{\gamma}{2}-\Gamma_0)t'}\frac{(\frac{\gamma}{2}-\Gamma_0)\cos\left[(\omega_0'-\Omega_0)t'-\omega_0' t-\phi_0+\Phi_0\right]+(\omega_0'-\Omega_0)\sin\left[(\omega_0'-\Omega_0)t'-\omega_0' t-\phi_0+\Phi_0\right]}{(\frac{\gamma}{2}-\Gamma_0)^2+(\omega_0'-\Omega_0)^2}\Bigg\}\Bigg|_0^t \\
&= \frac{A_m A_{ff}}{2}\frac{1}{(\frac{\gamma}{2}-\Gamma_0)^2+(\omega_0'+\Omega)^2}\Big\{(\frac{\gamma}{2}-\Gamma_0)\left[\cos(\Omega_0 t-\phi_0-\Phi_0)e^{-\Gamma_0 t}-\cos(\omega_0' t+\phi_0+\Phi_0)e^{-\frac{\gamma}{2}t}\right] \\
&+(\omega'+\Omega_0)\left[\sin(\Omega_0 t-\phi_0-\Phi_0)e^{-\Gamma_0 t}+\sin(\omega_0' t+\phi_0+\Phi_0)e^{-\frac{\gamma}{2}t}\right]\Big\} \\
&+\frac{A_m A_{ff}}{2}\frac{1}{(\frac{\gamma}{2}-\Gamma_0)^2+(\omega_0'-\Omega)^2}\Big\{(\frac{\gamma}{2}-\Gamma_0)\left[\cos(\Omega_0 t+\phi_0-\Phi_0)e^{-\Gamma_0 t}-\cos(\omega_0' t+\phi_0-\Phi_0)e^{-\frac{\gamma}{2}t}\right] \\
&-(\omega'-\Omega_0)\left[\sin(\Omega_0 t+\phi_0-\Phi_0)e^{-\Gamma_0 t}-\sin(\omega_0' t+\phi_0-\Phi_0)e^{-\frac{\gamma}{2}t}\right]\Big\}.
\end{aligned}
\tag{3.76}
$$

By introducing the phase shift $\phi_+ = \cos^{-1}\left(\frac{\frac{\gamma}{2}-\Gamma_0}{\sqrt{(\frac{\gamma}{2}-\Gamma_0)^2+(\omega_0'+\Omega_0)^2}}\right)$ and $\phi_- = \cos^{-1}\left(\frac{\frac{\gamma}{2}-\Gamma_0}{\sqrt{(\frac{\gamma}{2}-\Gamma_0)^2+(\omega_0'-\Omega_0)^2}}\right)$, we have

$$C_v(t) = \frac{A_m A_{ff}}{2(\frac{\gamma}{2}-\Gamma_0)}\Big\{ \cos\phi_+\big[\cos\left(\Omega_0 t-\phi_0-\Phi_0-\phi_+\right)e^{-\Gamma_0 t} - \cos\left(\omega_0' t+\phi_0+\Phi_0+\phi_+\right)e^{-\frac{\gamma}{2}t}\big] + \cos\phi_-\big[\cos\left(\Omega_0 t+\phi_0-\Phi_0+\phi_-\right)e^{-\Gamma_0 t} - \cos\left(\omega_0' t+\phi_0-\Phi_0+\phi_-\right)e^{-\frac{\gamma}{2}t}\big]\Big\}. \tag{3.77}$$

Calculation of Eq. 3.77.

$$\begin{aligned} C_v(t) &= \frac{A_m A_{ff}}{2\sqrt{(\frac{\gamma}{2}-\Gamma_0)^2+(\omega_0'+\Omega_0)^2}}\left[\cos\left(\Omega_0 t-\phi_0-\Phi_0-\phi_+\right)e^{-\Gamma_0 t} - \cos\left(\omega_0' t+\phi_0+\Phi_0+\phi_+\right)e^{-\frac{\gamma}{2}t}\right] \\ &+ \frac{A_m A_{ff}}{2\sqrt{(\frac{\gamma}{2}-\Gamma_0)^2+(\omega_0'-\Omega_0)^2}}\left[\cos\left(\Omega_0 t+\phi_0-\Phi_0+\phi_-\right)e^{-\Gamma_0 t} - \cos\left(\omega_0' t+\phi_0-\Phi_0+\phi_-\right)e^{-\frac{\gamma}{2}t}\right] \\ &= \frac{A_m A_{ff}}{2(\frac{\gamma}{2}-\Gamma_0)}\Big\{ \cos\phi_+\big[\cos\left(\Omega_0 t-\phi_0-\Phi_0-\phi_+\right)e^{-\Gamma_0 t} - \cos\left(\omega_0' t+\phi_0+\Phi_0+\phi_+\right)e^{-\frac{\gamma}{2}t}\big] \\ &+ \cos\phi_-\big[\cos\left(\Omega_0 t+\phi_0-\Phi_0+\phi_-\right)e^{-\Gamma_0 t} - \cos\left(\omega_0' t+\phi_0-\Phi_0+\phi_-\right)e^{-\frac{\gamma}{2}t}\big]\Big\}. \end{aligned} \tag{3.78}$$

Now let's look at the case of overdamped oscillation in the environment, where $\omega_0^2-(\frac{\gamma}{2})^2 < 0$. So we have $\omega_0' = \sqrt{\omega_0^2-(\frac{\gamma}{2})^2} = i\sqrt{(\frac{\gamma}{2})^2-\omega_0^2} = i\omega_0''$. The mobility $M_v(t)$ is,

$$M_v(t) = \frac{1}{4\gamma\omega_0''}e^{-\frac{\gamma}{2}t}\left[\left(\omega_0''-\frac{\gamma}{2}\right)e^{-(\frac{\gamma}{2}-\omega_0'')t} + \left(\omega_0''+\frac{\gamma}{2}\right)e^{-(\frac{\gamma}{2}+\omega_0'')t}\right]. \tag{3.79}$$

Calculation of Eq. 3.79.

$$\begin{aligned} M_v(t) &= \frac{1}{2\gamma\omega_0'}e^{-\frac{\gamma}{2}t}\left(\omega_0'\cos\left(\omega_0' t\right) - \frac{\gamma}{2}\sin\left(\omega_0' t\right)\right) \\ &= \frac{1}{2i\gamma\omega_0''}e^{-\frac{\gamma}{2}t}\left(i\omega_0''\cosh\left(\omega_0'' t\right) - i\frac{\gamma}{2}\sinh\left(\omega_0'' t\right)\right) \\ &= \frac{1}{2\gamma\omega_0''}e^{-\frac{\gamma}{2}t}\left(\omega_0''\cosh\left(\omega_0'' t\right) - \frac{\gamma}{2}\sinh\left(\omega_0'' t\right)\right) \\ &= \frac{1}{4\gamma\omega_0''}e^{-\frac{\gamma}{2}t}\left(\omega_0''\left(e^{\omega_0'' t}+e^{-\omega_0'' t}\right) - \frac{\gamma}{2}\left(e^{\omega_0'' t}-e^{-\omega_o'' t}\right)\right) \\ &= \frac{1}{4\gamma\omega_0''}\left[\left(\omega_0''-\frac{\gamma}{2}\right)e^{-(\frac{\gamma}{2}-\omega_0'')t} + \left(\omega_0''+\frac{\gamma}{2}\right)e^{-(\frac{\gamma}{2}+\omega_0'')t}\right]. \end{aligned} \tag{3.80}$$

Define $A = \frac{\gamma}{2}-\omega_0''$ and $B = \frac{\gamma}{2}+\omega_0''$, we have

$$M_v(t) = \frac{1}{4\gamma\omega_0''}\left[-Ae^{-At}+Be^{-Bt}\right]. \tag{3.81}$$

and the velocity ACF in the overdamped case is

$$C_v(t) = M_v(t) * C_f(t) = \int_0^t \frac{1}{4\gamma\omega_0''} \frac{\left(\frac{F}{m}\right)^2}{\cos\Phi_0} \left[-Ae^{-A(t-t')} + Be^{-B(t-t')}\right] e^{-\Gamma_0 t'} \cos\left(\Omega_0 t' - \Phi_0\right) \mathrm{d}t'$$
$$= \frac{1}{4\gamma\omega_0''} \frac{\left(\frac{F}{m}\right)^2}{\cos\Phi_0} \int_0^t \left[-Ae^{-A(t-t')} + Be^{-B(t-t')}\right] e^{-\Gamma_0 t'} \cos\left(\Omega_0 t' - \Phi_0\right) \mathrm{d}t'. \tag{3.82}$$

We try to calculate the integral part $C(t)$, which is defined below, and its derivation is shown in detail in Eq. 3.84,

$$\begin{aligned} C(t) &= \int_0^t \left[-Ae^{-A(t-t')} + Be^{-B(t-t')}\right] e^{-\Gamma_0 t'} \cos\left(\Omega_0 t' - \Phi_0\right) \mathrm{d}t' \\ &= -\frac{A}{\sqrt{\left(A-\Gamma_0\right)^2 + \Omega_0^2}} \left[\cos\left(\Omega_0 t - \Phi_0 - \phi_A\right) e^{-\Gamma_0 t} - \cos\left(\Phi_0 + \phi_A\right) e^{-At}\right] \\ &+ \frac{B}{\sqrt{\left(B-\Gamma_0\right)^2 + \Omega_0^2}} \left[\cos\left(\Omega_0 t - \Phi_0 - \phi_B\right) e^{-\Gamma_0 t} - \cos\left(\Phi_0 + \phi_B\right) e^{-Bt}\right], \end{aligned} \tag{3.83}$$

where $\cos\phi_A = \frac{A-\Gamma_0}{\sqrt{(A-\Gamma_0)^2+\Omega_0^2}}$ and $\cos\phi_B = \frac{B-\Omega_0}{\sqrt{(B-\Gamma_0)^2+\Omega_0^2}}$.

Calculation of Eq. 3.83.

$$
\begin{aligned}
&\int_0^t \left[-Ae^{-A(t-t')} + Be^{-B(t-t')}\right] e^{-\Gamma_0 t'} \cos\left(\Omega_0 t' - \Phi_0\right) \mathrm{d}t' \\
&= -Ae^{-At} \int_0^t e^{(A-\Gamma_0)t'} \cos\left(\Omega_0 t' - \Phi_0\right) \mathrm{d}t' + Be^{-Bt} \int_0^t e^{(B-\Gamma_0)t'} \cos\left(\Omega_0 t' - \Phi_0\right) \mathrm{d}t' \\
&= -Ae^{-At} e^{(A-\Gamma_0)t'} \frac{(A-\Gamma_0)\cos\left(\Omega_0 t' - \Phi_0\right) + \Omega_0 \sin\left(\Omega_0 t' - \Phi_0\right)}{(A-\Gamma_0)^2 + \Omega_0^2}\Big|_0^t \\
&+ Be^{-Bt} e^{(B-\Gamma_0)t'} \frac{(B-\Gamma_0)\cos\left(\Omega_0 t' - \Phi_0\right) + \Omega_0 \sin\left(\Omega_0 t' - \Phi_0\right)}{(B-\Gamma_0)^2 + \Omega_0^2}\Big|_0^t \\
&= -\frac{Ae^{-At}}{(A-\Gamma_0)^2 + \Omega_0^2}\Big\{ (A-\Gamma_0)\left[\cos\left(\Omega_0 t - \Phi\right) e^{(A-\Gamma_0)t} - \cos\left(-\Phi_0\right)\right] \\
&+ \Omega_0 \left[\sin\left(\Omega_0 t - \Phi\right) e^{(A-\Gamma_0)t} - \sin\left(-\Phi_0\right)\right] \Big\} \\
&+ \frac{Be^{-Bt}}{(B-\Gamma_0)^2 + \Omega_0^2}\Big\{ (B-\Gamma_0)\left[\cos\left(\Omega_0 t - \Phi\right) e^{(B-\Gamma_0)t} - \cos\left(-\Phi_0\right)\right] \\
&+ \Omega_0 \left[\sin\left(\Omega_0 t - \Phi\right) e^{(B-\Gamma_0)t} - \sin\left(-\Phi_0\right)\right] \Big\} \\
&= -\frac{A}{(A-\Gamma_0)^2 + \Omega_0^2}\Big\{ (A-\Gamma_0)\left[\cos\left(\Omega_0 t - \Phi\right) e^{-\Gamma_0 t} - \cos\left(\Phi_0\right) e^{-At}\right] \\
&+ \Omega_0 \left[\sin\left(\Omega_0 t - \Phi\right) e^{-\Gamma_0 t} + \sin\left(\Phi_0\right) e^{-At}\right] \Big\} \\
&+ \frac{B}{(B-\Gamma_0)^2 + \Omega_0^2}\Big\{ (B-\Gamma_0)\left[\cos\left(\Omega_0 t - \Phi\right) e^{-\Gamma_0 t} - \cos\left(\Phi_0\right) e^{-Bt}\right] \\
&+ \Omega_0 \left[\sin\left(\Omega_0 t - \Phi\right) e^{-\Gamma_0 t} + \sin\left(\Phi_0\right) e^{-Bt}\right] \Big\} \\
&\text{let } \cos\left(\phi_A\right) = \frac{A-\Gamma_0}{\left(A-\Gamma_0\right)^2 + \Omega_0^2} \text{ and } \cos\left(\phi_B\right) = \frac{B-\Gamma_0}{\left(B-\Gamma_0\right)^2 + \Omega_0^2} \\
&= -\frac{A}{\sqrt{\left(A-\Gamma_0\right)^2 + \Omega_0^2}} \left[\cos\left(\Omega_0 t - \Phi_0 - \phi_A\right) e^{-\Gamma_0 t} - \cos\left(\Phi_0 + \phi_A\right) e^{-At}\right] \\
&+ \frac{B}{\sqrt{\left(B-\Gamma_0\right)^2 + \Omega_0^2}} \left[\cos\left(\Omega_0 t - \Phi_0 - \phi_B\right) e^{-\Gamma_0 t} - \cos\left(\Phi_0 + \phi_B\right) e^{-Bt}\right].
\end{aligned}
\tag{3.84}
$$

With Taylor expansion, $A = \frac{\gamma}{2} - \omega_0'' = \frac{\gamma}{2} - \sqrt{\left(\frac{\gamma}{2}\right)^2 - \omega_0^2} = \frac{\gamma}{2}\left(1 - \sqrt{1 - \left(\frac{2\omega_0}{\gamma}\right)^2}\right) \approx \frac{\gamma}{2} \times \frac{1}{2}\left(\frac{2\omega_0}{\gamma}\right)^2 = \omega_0\left(\frac{\omega_0}{\gamma}\right)$ and $B = \frac{\gamma}{2} + \omega_0'' \approx \gamma$. For $\gamma \gg \Gamma_0$, Ω_0, $\cos\phi_B \approx 1$ and $\phi_B \to 0$

$$
\begin{aligned}
C(t) = &-\frac{A}{\sqrt{(A-\Gamma_0)^2 + \Omega_0^2}} \left[\cos\left(\Omega_0 t - \Phi_0 - \phi_A\right) e^{-\Gamma_0 t} - \cos\left(\Phi_0 + \phi_A\right) e^{-At}\right] \\
&+ \cos\left(\Omega_0 t - \Phi_0\right) e^{-\Gamma_0 t} - \cos\Phi_0 e^{-\gamma t}.
\end{aligned}
\tag{3.85}
$$

This is a well-separation of time scales, i.e. $\gamma \gg \Gamma_0$ and Ω_0, such that for $t_0 \sim \frac{1}{\gamma}$, $\cos(\Omega_0 t_0 - \Phi_0)e^{-\Gamma_0 t_0} \to \cos(\Omega_0 \frac{1}{\gamma} - \Phi_0)e^{-\Gamma_0/\gamma} \approx \cos\Phi_0$ and $\cos(\Omega_0 t - \Phi_0)e^{-\Gamma_0 t} - \cos\Phi_0 e^{-\gamma t} \approx \cos\Phi_0(1-e^{-\gamma t})$ $(0 \le t \le t_0)$. So we can ignore the last $\cos\Phi_0 e^{-\gamma t}$ term. Likewise for $\Gamma_0 \gg A$, and for the time scale $t < \frac{1}{A}$, we can ignore the $\cos\Phi_0 e^{-\gamma t}$ term. The Eq. 3.85 is simplified into

$$\begin{aligned} C(t) &= e^{-\Gamma_0 t}\left[\cos\left(\Omega_0 t - \Phi_0\right) - \frac{A}{\sqrt{(A-\Gamma_0)^2+\Omega_0^2}}\cos\left(\Omega_0 t - \Phi_0 - \phi_A\right)\right] \\ &= e^{-\Gamma_0 t}\left[\left(1 - \frac{A\left(A-\Gamma_0\right)}{\left(A-\Gamma_0\right)^2+\Omega_0^2}\right)\cos\left(\Omega_0 t - \Phi_0\right) - \frac{A\Omega_0}{\left(A-\Gamma_0\right)^2-\Omega_0^2}\sin\left(\Omega_0 t - \Phi_0\right)\right] \\ &= C_0\left(A,\Gamma_0,\Omega_0\right)e^{-\Gamma_0 t}\cos\left(\Omega_0 t - \Phi_0 + \Delta\Phi\right), \end{aligned} \tag{3.86}$$

where

$$\begin{aligned} C_0(A,\Gamma_0,\Omega_0) &= \sqrt{\left(1 - \frac{A(A-\Gamma_0)}{(A-\Gamma_0)^2+\Omega_0^2}\right)^2 + \left(\frac{A\Omega_0}{(A-\Gamma_0)^2+\Omega_0^2}\right)^2} \\ &= \frac{1}{(A-\Gamma_0)^2+\Omega_0^2}\sqrt{(\Gamma_0^2 - \Gamma_0 A + \Omega_0^2)^2 + A^2\Omega_0^2}. \end{aligned} \tag{3.87}$$

3.5 MECHANICS OF CELL BODY AND FLAGELLA

Using the resistive force theory in Chapter 1, the motion of cell can be described by three parameters: the swimming speed v, the flagellum angular speed ω, and the body angular speed Ω, with $(v,\omega,\Omega) > 0$. Let's assume they are in the vector form as follows, $\vec{v} = (-v,0,0)$, $\vec{\omega} = (\omega,0,0)$, and $\vec{\Omega} = (-\Omega,0,0)$.

Following Fig. 30, we have

$$\begin{bmatrix} -F_f \\ N_f \end{bmatrix} = \begin{bmatrix} A & -B \\ -B & D \end{bmatrix} \cdot \begin{bmatrix} v \\ \omega \end{bmatrix}, \tag{3.88}$$

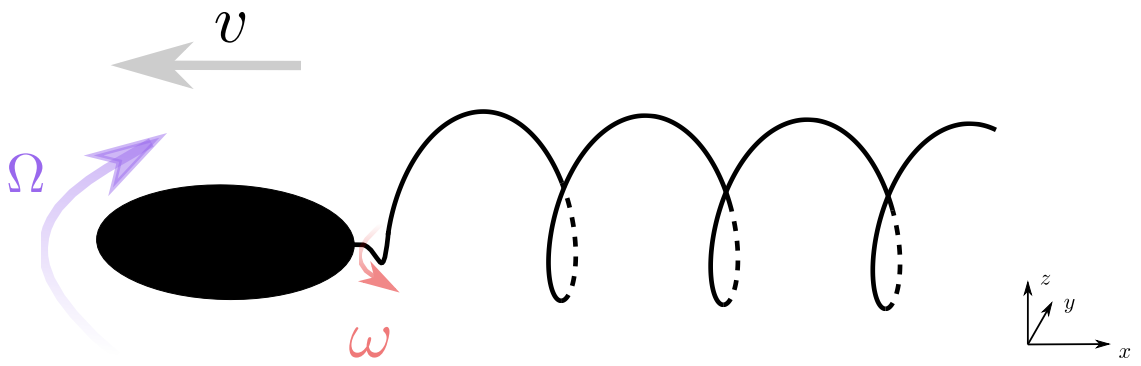

Figure 30: Schematic figure of a bacterium swimming with the corresponding parameters. Ω, ω, and v are the angular speed of the cell body, the angular speed of the flagellum, and the swimming speed of the cell, respectively.

where F_f and N_f are the thrust force and the torque of the flagellum, respectively. The coefficients A, B and D defined above, are positive and proportional to fluid viscosity η. For a helical coil, the expressions of A, B, and D can be obtained [54],

$$A = k_n l \frac{1-\beta}{\beta^{1/2}}\big(1 + \gamma_k \frac{\beta}{1-\beta}\big) = A'\eta, \tag{3.89}$$

$$B = k_n l (\frac{\lambda}{2\pi}) \frac{1-\beta}{\beta^{1/2}}\big(1 - \gamma_k\big) = B'\eta, \tag{3.90}$$

and

$$D = k_n l (\frac{\lambda}{2\pi})^2 \frac{1-\beta}{\beta^{1/2}}\big(1 + \gamma_k \frac{1-\beta}{\beta}\big) = D'\eta. \tag{3.91}$$

The parameters in Eq. 3.89 - 3.91 can be obtained from Ref. [55] and are listed in Table 5, in which l, λ, R and r are the total length, the pitch, the coil radius, and the radius of the flagella, respectively. $\psi = \arctan(2\pi R/\lambda)$ is the angle made by the flagellar filament with the flagellar axis. β in the above equations is defined as $\cos^2\psi$. The normal k_n $(= \frac{8\pi\eta}{2\ln(\frac{c\lambda}{r})+1})$ and the tangential k_t $(= \frac{4\pi\eta}{2\ln(\frac{c\lambda}{r})-1})$ resistive coefficients have been derived in Chapter 1, where $c = 0.18$ is the Lighthill constant [19], and the ratio $r_k = k_t/k_n \approx 0.7$.

Bacterial strain	Flagellar dimensions				Cell size
Genus Name	l (μm)	λ (μm)	$2R$ (nm)	r (nm)	a, b (μm)
V. alginolyticus YM42	3.7 (1)	1.2 (0.02)	280 (1)	16	0.35, 2.3

Table 5: The parameters of cell geometry. The uncertainties in parenthesis are standard errors of the mean.

For swimming bacteria, the torques and forces of the cell body and those of flagella are balanced, so $N_f = N_b = D_0\Omega$, $F_f = F_b = A_0 v$, where D_0 and A_0 are the drag coefficients of the cell body. They can be expressed as $D_0 = \frac{16\pi\eta a^2 b}{3} = D_0'\eta$ and $A_0 = \frac{4\pi\eta b}{\ln(\frac{2b}{a})-\frac{1}{2}} = A_0'\eta$, where a and b are semi-minor and semi-major length of cell body, respectively. The values of a and b are also shown in Table 5. The force and torque balance equations are

$$\begin{aligned} -A_0 v &= Av - B\omega, \\ D_0\Omega &= -Bv + D\omega, \end{aligned} \tag{3.92}$$

where Ω and ω are related to the motor angular speed Ω_m as

$$\Omega_m = \Omega + \omega. \tag{3.93}$$

We can write both v and Ω in terms of Ω_m, which can be viewed as a control parameter for the given a, b, flagellar geometry, and η.

Using Eq. 3.92 and Eq. 3.93, we find that

$$\begin{aligned} \omega &= \frac{D_0(A+A_0)}{(D+D_0)(A+A_0)-B^2}\Omega_m, \\ v &= \frac{BD_0}{(D+D_0)(A+A_0)-B^2}\Omega_m, \end{aligned} \tag{3.94}$$

and

$$\Omega = \Omega_m - \omega = \Omega_m - \frac{D_0(A+A_0)}{(D+D_0)(A+A_0)-B^2}\Omega_m = \frac{D(A+A_0)-B^2}{(D+D_0)(A+A_0)-B^2}\Omega_m. \tag{3.95}$$

This shows that as long as the flagellar motor maintains a constant speed, ω, v, and Ω are independent of viscosity. However, the bacterial flagellar motors generally do not have a

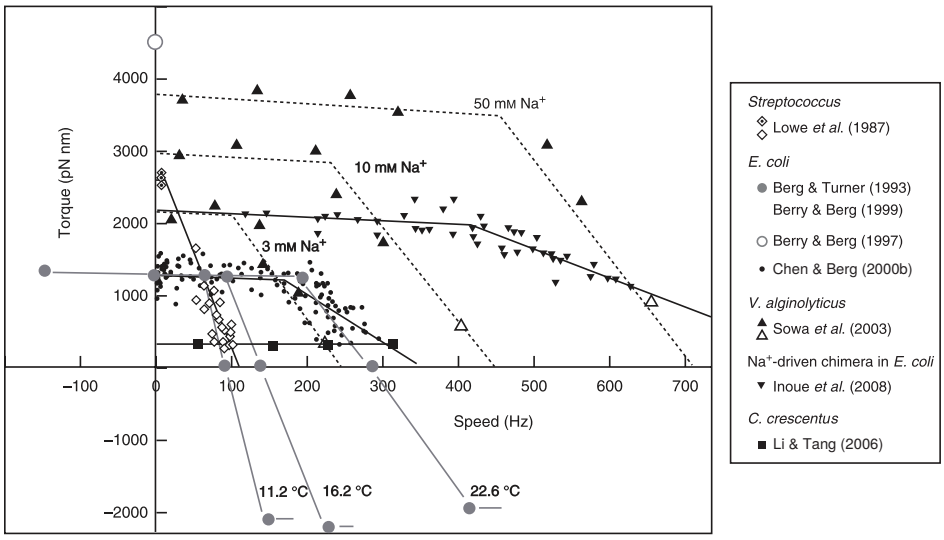

Figure 31: The torque-speed relationships for different kinds of bacterial motors. All measurements have been done under room temperature [7] except those indicated with temperature values in the figure.

constant speed. Rather, they obey the torque-speed relationships, which are shown in Fig. 31 and are adopted from Ref. [9].

The total torque acting on the flagellum motor N_m should be twice of that of the viscous torque on the cell body $N_m = 2D_0\Omega$, one due to cell body rotation and the other due to flagellar rotation. Thus, we have

$$N_m(\Omega_m) = 2D_0 \frac{D(A+A_0) - B^2}{(D+D_0)(A+A_0) - B^2}\Omega_m = \alpha\Omega_m. \tag{3.96}$$

This is the loading line and is plotted in Fig. 32. Its intersection defines the operating point (Ω_m^0, N_m^0) of the flagellar motor. We also see that the slope α increases with η.

For the latter calculation with a concise notation, let's define

$$\begin{aligned} f &= \frac{1}{\eta^2}\big(D(A+A_0) - B^2\big) = D'(A'+A_0') - B'^2, \\ g &= \frac{1}{\eta^2}\big((D+D_0)(A+A_0) - B^2\big) = (D'+D_0')(A'+A_0') - B'^2, \end{aligned} \tag{3.97}$$

where both f and g are independent of η and only depend on cell geometry.

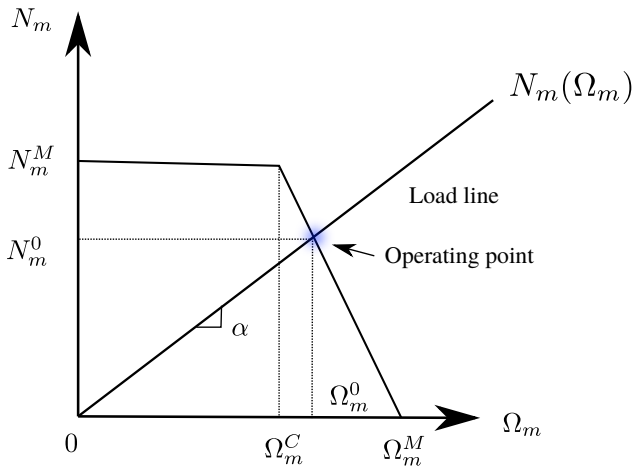

Figure 32: Schematic figure of the relationship between the loading line $N_m(\Omega_m)$ and flagellum motor torque N_m vs. its angular speed Ω_m. The loading line $N_m(\Omega_m)$ follows the form of Eq. 3.96. Intersection of torque-angular-speed relationship with the load-line, which determines the operating point, has been marked with blue color.

Let's find the operating point based on the above information. The motor torque and angular speed relationship can be expressed as follows,

$$N_m = \begin{cases} N_m^M & \Omega_m < \Omega_m^C, \\ \frac{N_m^M}{\Omega_m^M - \Omega_m^C}(\Omega_m^M - \Omega_m) & \Omega_m^C < \Omega_m < \Omega_m^M, \\ 0 & \Omega_m > \Omega_m^M. \end{cases} \tag{3.98}$$

First, let's examine the high-load regime, $\Omega_m < \Omega_m^C$. We have $N_m^0 = N_m^M$, and $\Omega_m^0 = N_m^M/\alpha$ and the cell's swimming speed is

$$v = \frac{BD_0}{(D+D_0)(A+A_0) - B^2}\Omega_m^0 = \frac{B}{D(A+A_0) - B^2}\frac{N_m^M}{2} = \frac{B'N_m^M}{2\eta f}. \tag{3.99}$$

This shows $v \sim \frac{1}{\eta}$, where B', N_m^M, and f are all constants, independent of η. Let η_0 be the viscosity of water as the reference, it shows that $\frac{v(\eta_0)}{v(\eta)} = \frac{\eta}{\eta_0}$ is only a function of viscosity, nothing else. Likewise we can examine the cell body rotation rate

$$\Omega = \frac{D(A+A_0) - B^2}{(D+D_0)(A+A_0) - B^2}\Omega_M^0 = \frac{N_m^M}{2D_0} = \frac{N_m^M}{2D_0'\eta}. \tag{3.100}$$

and we have

$$\frac{\Omega(\eta_0)}{\Omega(\eta)} = \frac{\eta}{\eta_0}. \tag{3.101}$$

So in the high-load regime, a swimming bacteria can be used as a living viscometer to probe the viscosity of the surrounding fluid, when v or Ω are measured.

Let's compare the calculation to our data. We need to change Eq. 3.99 into

$$\frac{v_0}{v} = \left(\frac{\eta(\phi)}{\eta_{solv}}\right) \times \left(\frac{2fv_0\eta_{solv}}{B'N_m^M}\right), \tag{3.102}$$

where $\eta_{solv} \approx 1.0518$ mPa·s is the viscosity of solvent (water at 18 °C) and $v_0 = \frac{B'D_0'\Omega_m^M}{g}$ (see the discussion in low load case below).

By applying $\log_{10}$ on both sides, Eq. 3.102 becomes

$$\log_{10}\left(\frac{v_0}{v}\right) = \log_{10}\left(\frac{\eta(\phi)}{\eta_{solv}}\right) + \log_{10}\left(\frac{2fv_0\eta_{solv}}{B'N_m^M}\right). \tag{3.103}$$

The polymer viscosity of PVP K-90 can be calculated with Fikenscher's equation [56][57],

$$\log_{10}(\eta_{rel}) = \log_{10}\left(\frac{\eta(\phi)}{\eta_{solv}}\right) = \left(\frac{75K_0^2}{1+1.5K_0c} + K_0\right)\cdot c, \tag{3.104}$$

where c is the mass concentration in g/100 ml and η_{rel} is the relative viscosity, $\eta_{rel} = \eta(\phi)/\eta_{solv}$. K-90 PVP polymers are used in the experiment so $K = 90$ and $K_0 = K/1000 = 0.09$ [56]. If we convert this mass concentration into weight percentage concentration used in our experiment, we can divide c by density of solutions, which is about the same with the density of water $\rho = 1$ g/ml (the density of PVP solutions is about 1.2 g/ml), so we have $\phi = c/\rho = c/100$. Eq. 3.104 becomes

$$\log_{10}\left(\frac{\eta(\phi)}{\eta_{solv}}\right) = \left(\frac{75K_0^2}{1+1.5K_0\cdot 100\phi} + K_0\right)\cdot 100\phi. \tag{3.105}$$

Combining Eq. 3.103 and Eq. 3.105, we have

$$\begin{aligned}\log_{10}(\frac{v_0}{v}) &= \left(\frac{75K_0^2}{1+1.5K_0\cdot 100\phi} + K_0\right)\cdot 100\phi + \log_{10}\left(\frac{2fv_0\eta_{solv}}{B'N_m^M}\right) \\ &= \left(\frac{75K_0^2}{1+1.5K_0\cdot 100\phi} + K_0\right)\cdot 100\phi + b,\end{aligned} \tag{3.106}$$

where $b = \log_{10}\left(\frac{2fv_0\eta_{solv}}{B'N_m^M}\right)$.

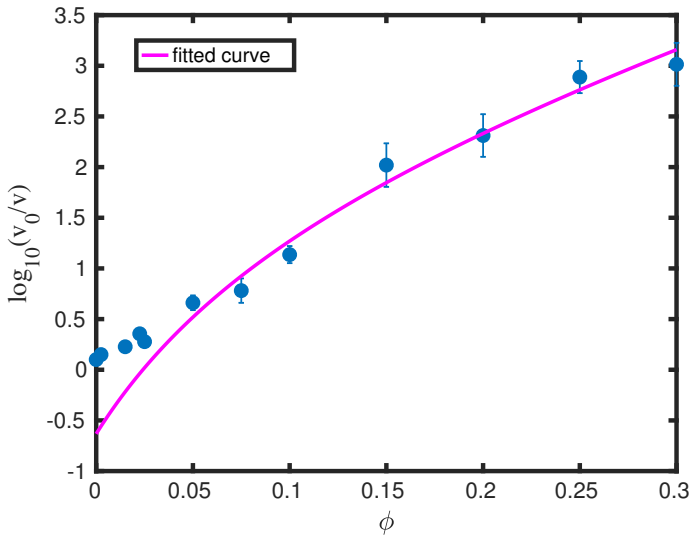

Figure 33: Log of reciprocal of swimming velocity vs. PVP concentration ϕ is plotted as blue dots for high load fitting. A nonlinear least squares fitting is applied for the high-load case and the purple line shows the fitting result.

In my measurement, when I plotted $\log_{10}(\frac{v_0}{v})$ v.s. ϕ, a quasi-linear relationship is obtained with a finite intercept, which is shown in Fig. 33. When the PVP concentration ϕ is getting large, Fikenscher equation can be well approximated by a linear relationship of $\log_{10}(\eta_{rel}) \propto \phi$. So I try to match the linear part of Fikenscher equation and the data, where $K(= 1000K_0)$ and b are the fitting parameters. After using Eq. 3.106 to fit the data as described above, we get $K \approx 60.0$ and the purple curve in Fig. 33 shows the fitting result. The K value is smaller than the nominal value of the sample we used. Following the Ashland manual, it belongs to PVP K-60 category, which is one grade lower than K-90. The "intercept" b obtained from fitting is -0.6 ± 0.3. By using the parameters in Table 5 and the information in Fig 31, we can find that $N_m^M = 3450\,\mathrm{pN}\cdot\mathrm{nm}$, based on which b is calculated with the value of -0.12. Considering the fact that all parameters are taken from indirect measurement, the deviation between fitted K value and nominal value is expected. The fact that the degradation of long polymer chains possibly makes K value smaller. But the data do capture the behavior of a quasi-linear relationship between $\log_{10}(\frac{v_0}{v})$ and PVP

concentration ϕ.

Let's see what happens in the low-load regime, $\Omega_m^C < \Omega_m < \Omega_m^M$. The angular speed at the operating point is equal to

$$\Omega_m^0 = \frac{\Omega_m^M}{2D_0'\eta\frac{f}{g}\frac{\Omega_m^M-\Omega_m^C}{N_m^M}+1}, \tag{3.107}$$

and the cell speed is

$$v = \frac{BD_0}{(D+D_0)(A+A_0)-B^2}\Omega_m^0 = \frac{B'D_0'}{g}\frac{\Omega_m^M}{2D_0'\eta\frac{f}{g}\frac{\Omega_m^M-\Omega_m^C}{N_m^M}+1} = \frac{B'D_0'\Omega_m^M}{2D_0'f\frac{\Omega_m^M-\Omega_m^C}{N_m^M}\eta+g}. \tag{3.108}$$

So the reciprocal of the speed is

$$\frac{1}{v} = \frac{1}{B'D_0'\Omega_m^M}\left(2D_0'f\frac{\Omega_m^M-\Omega_m^C}{N_m^M}\eta(\phi)+g\right). \tag{3.109}$$

Define $\frac{1}{v_0} = \frac{g}{B'D_0'\Omega_m^M}$, which has been used in the high-load case, it follows

$$\frac{v_0}{v}-1 = \frac{2fv_0}{B'\Omega_m^M}\frac{\Omega_m^M-\Omega_m^C}{N_m^M}\eta(\phi). \tag{3.110}$$

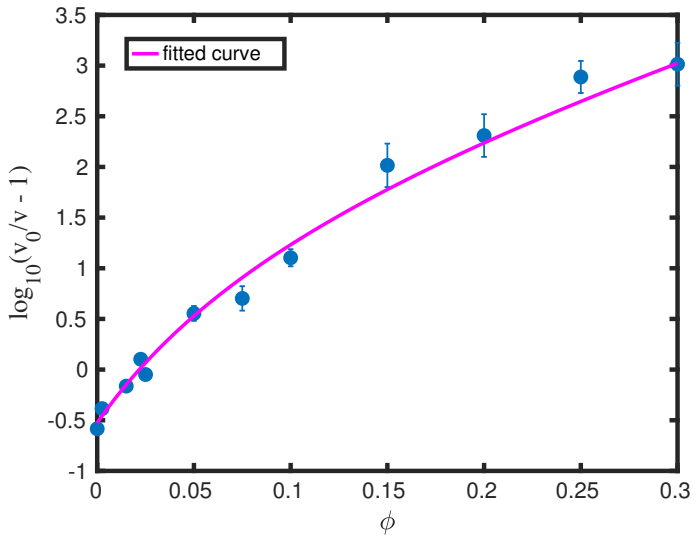

Figure 34: A nonlinear least squares fitting is applied with Eq. 3.111 for the low-load case and the purple line shows the fitting result.

Eventually, we have

$$\begin{aligned}\log_{10}\left(\frac{v_0}{v}-1\right) &= \log_{10}\left(\frac{\eta(\phi)}{\eta_{solv}}\right)+\log_{10}\left(\frac{2fv_0}{B'\Omega_m^M}\frac{\Omega_m^M-\Omega_m^C}{N_m^M}\eta_{solv}\right)\\ &= \left(\frac{75K_0^2}{1+1.5K_0\cdot 100\phi}+K_0\right)\cdot 100\phi+b.\end{aligned} \tag{3.111}$$

When I plotted $\log_{10}(\frac{v_0}{v}-1)$ v.s. ϕ in Fig. 34, the relationship is not quasi-linear any more. Following what we have done previously, it can be noticed that $|\,\mathrm{d}N_m/\,\mathrm{d}\Omega_m| = N_m^M/(\Omega_m^M-\Omega_m^C) = 13.68/2\pi\,\mathrm{pN\cdot nm/Hz}$, $\Omega_m^M = 650\times 2\pi\,\mathrm{Hz}$, and $v_0 = 42.37\,\mu\mathrm{m/s}$. Then we can calculate that b is equal to -0.529. After a nonlinear least squares fitting, it shows that $K = 54\pm 4$ and $b = -0.53\pm 0.5$ and this result is close to what we have already calculated. The measured swimming speed of *V. alginolyticus* in the buffer is $v = 33.62\,\mu$m/s and with Eq. 3.111, we can calculate that the viscosity of buffer is 0.93 mPa·s, which is a reasonable value, since the viscosity of water is 1.0518 mPa·s.

3.6 SWIMMING VELOCITY OF *V. ALGINOLYTICUS* SCALES WITH POLYMER CONCENTRATION

This section includes a simple estimation to capture how the swimming velocity of *V. alginolyticus* scales with PVP polymer concentration from an energetic perspective.

The rate of generating an empty volume in the polymer solution is, $r = Av_{sw}$ with $A = \pi a^2$ and a is cell's radius. The elastic energy density is given by the elastic modulus, $E = \frac{k_BT}{\xi^3}$ where $\xi = \langle R_{g0}^2\rangle^{\frac{1}{2}}(\frac{\phi}{\phi^*})^{-\frac{\nu}{(3\nu-1)}}$, and $\langle R_{g0}^2\rangle = R_0^2$ is the square coil size of the polymer when isolated. In Ref. [46], it is shown that

$$\xi = R_0(\frac{\phi}{\phi^*})^{-\frac{\nu}{(3\nu-1)}} \sim \begin{cases}(\frac{\phi}{\phi^*})^{-\frac{2}{3}}, & \text{Zimm Model.}\\ (\frac{\phi}{\phi^*})^{-1}, & \text{Rouse Model.}\end{cases} \tag{3.112}$$

The work per second done by the bacterium is $\frac{dw}{dt} = Er = EAv_{sw} = \frac{\pi a^2 k_BT}{\xi^3}v_{sw}$. If this is equal to the power generated by the motors, $\frac{dw}{dt} = P_{sw}$, which is assumed to be a constant

value, we have

$$v_{sw} = \frac{P_{sw}\xi^3}{\pi a^2 k_B T} \sim \begin{cases} \phi^{-2}, & \text{Zimm Model.} \\ \phi^{-3}, & \text{Rouse Model.} \end{cases} \tag{3.113}$$

In Fig. 35, the slope is approximately equal to -3, which confirms that Rouse Model is more realistic in this case.

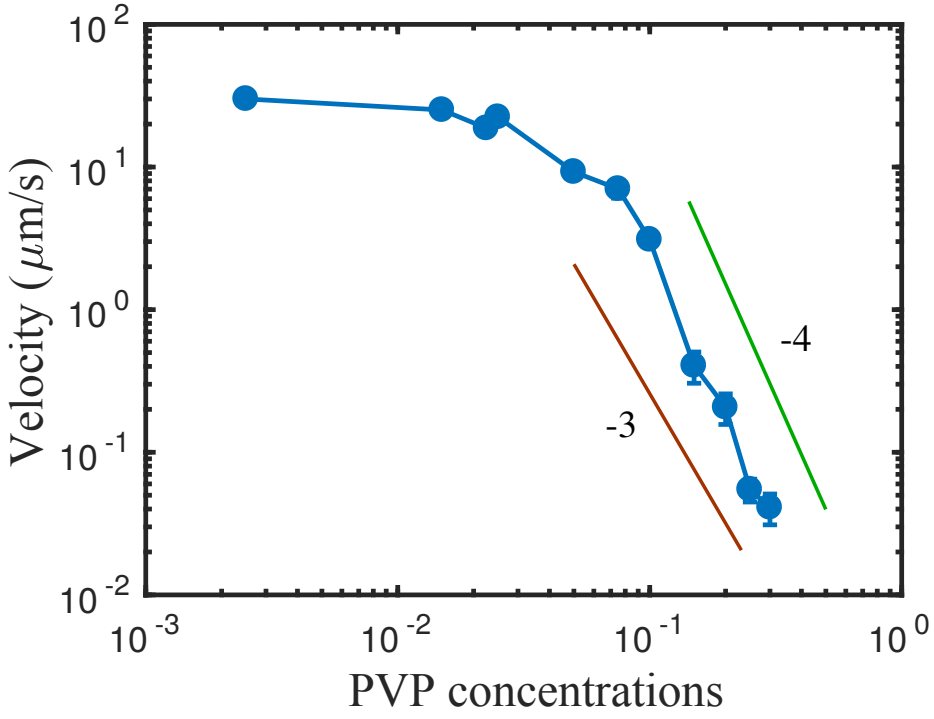

Figure 35: Swimming velocity vs. PVP concentration. The data is plotted as a blue curve with big points in log-log scale. The green and red lines indicate the slope of -4 and -3, respectively, and it can be noticed that the absolute value of slope of data curve is slightly larger than 3.

3.7 CONCLUSION

In this chapter, we have used the velocity ACF $\langle \vec{v}(t) \cdot \vec{v}(0) \rangle$ to analyze the bacterial motility patterns in different concentrations of polymer solutions. We discovered that the signal of

velocity ACF is generated from two channels: velocity's magnitudes, the speed fluctuations $\langle v(t)v(0)\rangle$ and the directional fluctuations $\langle \hat{a}(t)\cdot\hat{a}(0)\rangle$. The rounded tops of the directional ACFs for a short time confirm the non-Poissonian behavior of *V. alginolyticus*' motility patterns mentioned in Chapter 2.

Based on our measurement, we found that the bacteria gradually lose their ability to flick as the polymer concentration increases and at concentrations $\phi \geq 5\%$ the motility pattern is best described by the cyclic run-reverse pattern. This phenomenon has been captured by the model using the Gamma distribution for the dwell-time intervals, and the fitting results suggest that the mean swimming interval times are not significantly affected by polymers. In the meantime, the effect of suppression of tumbling by the polymer environment has also been found in case of *E. coli* [58].

A more cyclic run-reverse pattern due to addition of polymers in swimming buffers can be described by the damped harmonic oscillator model as well. By increasing polymer concentration in the solutions, the elasticity starts to emerge when $\phi \geq \phi^*$, and we observed a "resonance-like" behavior in directional ACFs. The damped harmonic oscillator model in this chapter suggests that this behavior may be due to bacterial response to this viscoelastic environment by adjusting its internal degree of freedom of motors switches. The phase shift $\Delta\Phi$ stemming from the polymer effect reaches a maximum value when $\phi \sim \phi^*$, implying that the emergence of viscoelastic property of polymer solutions generates the "resonance-like" behavior.

In experimental studies of polymer solutions, the presence of ϕ^* represents a subtle feature in a bulk measurement. However, for a polar flagellated marine bacterium *V. alginolyticus*, such a special point is rendered observable by a resonance-like effect in the velocity ACF. This potentially opens new doors for studying micro-rheology of complex fluids using bacteria as probe particles. The observation also begs for answers for how an internal oscillator of a bacteria responds to external mechanical environments. That a bacterium regulates its motility based on environmental cues is a well-known phenomenon and is one of the important survival strategies of microorganisms. However, it is unclear whether the changes in the internal parameters, such as the oscillation frequency and phase, seen in our experiment is a result of genuine biological response to the environmental stress or a physical response

governed by non-equilibrium statistical mechanics. New experiments and better theoretical modeling are called for to address these questions.

With the resistive force theory, we also find the swimming velocity dependence on the viscosity of polymer solutions in high and low motor load regions. Using non-linear least squared fitting, our results suggest that the polymer sample we used has a lower K value than nominal value $K = 90$. Here K value is used to characterize polymer solutions. One possibility for this is that PVP polymer chains are not stable enough and the degradation of polymer chains makes K value small. However, Ref. [59] claims that the PVP polymer is very stable. An alternative possibility is that PVP is polydispersed. The viscosity measurements in K-value system are based on bulk rheology rather than a micro-rheology. The viscosity calculated by the resistive force theory should be the viscosity "seen" by bacteria. In this case, the polymer chains with smaller molecular weights should tend to play important roles in contributing to viscosity in the dimension of bacterial size, which means the corresponding K value would be smaller. Finally, based on an energetic consideration, we found that bacteria swimming velocity obeys a scaling relation. That is a reasonable agreement with the Rouse model, which may be expected because such model is applicable to a solution with high polymer concentrations when hydrodynamic interactions between polymer strands are negligible.

BIBLIOGRAPHY

[1] Michael Eisenbach and Adler Julius. Bacterial cell envelopes with functional flagella. *The Journal of Biological Chemistry*, 256(16):8807–8814, 1981.

[2] Linda Turner, William S. Ryu, and Howard C. Berg. Real-time imaging of fluorescent flagellar filaments. *Journal of bacteriology*, 182(10):2793–2801, 2000.

[3] H.Y. Liang, L.Q. Xia, Z.H. Wu, J.C. Jian, and Y.S. Lu. Expression, purification and antibody preparation of flagellin *FlaA* from *Vibrio alginolyticus* strain HY9901. *Letters in Applied Microbiology*, 50(2):181–186, February 2010.

[4] Kwangmin Son, J.S. Guasto, and R. Stocker. Bacteria can exploit a flagellar buckling instability to change direction. *Nature Physics*, 9:494–498, 2013.

[5] Tuba Altindal, Suddhashil Chattopadhyay, and Xiao-Lun Wu. Bacterial chemotaxis in an optical trap. *PLoS ONE*, 6:e18231, 2011.

[6] Li Xie, Tuba Altindal, Suddhashil Chattopadhyay, and Xiao-Lun Wu. Bacterial flagellum as a propeller and as a rudder for efficient chemotaxis. *Proc. Natl. Acad. Sci. USA*, 108:2246–2251, 2011.

[7] Yoshiyuki Sowa, Hiroyuki Hotta, Michio Homma, and Akihiko Ishijima. Torquespeed Relationship of the Na+-driven Flagellar Motor of Vibrio alginolyticus. *Journal of Molecular Biology*, 327(5):1043–1051, April 2003.

[8] Ronald Bentley and S. R. Meganathan. Biosynthesis of vitamin k (menaquinone) in bacteria. *Microbiological Reviews*, 46(3):241–280, Spet 1982.

[9] Yoshiyuki Sowa and Richard M. Berry. Bacterial flagellar motor. *Quarterly Reviews of Biophysics*, 41(02), May 2008.

[10] Masaaki Furuno, Tatsuo Atsumi, Taku Yamada, Seiji Kojima, Noriko Nishioka, Ikuro Kawagishi, and Michio Homma. Characterization of polar-flagellar-length mutants in Vibrio alginolyticus. *Microbiology*, 143(5):1615–1621, 1997.

[11] Yasuhiro Onoue and Michio Homma. *Structure of the Sodium-Driven Flagellar Motor in Marine Vibrio*, pages 253–258. Springer New York, New York, NY, 2017.

[12] Jianhua Xing, Fan Bai, Richard Berry, and George Oster. Torquespeed relationship of the bacterial flagellar motor. *Proceedings of the National Academy of Sciences*, 103(5):1260–1265, 2006.

[13] Graeme Lowe, Markus Meister, and Howard C. Berg. Rapid rotation of flagellar bundles in swimming bacteria. *Nature*, 325(6105):637–640, Feb 1987.

[14] Y. Magariyama, S. Sugiyama, K. Muramoto, Y. Maekawa, I. Kawagishi, Y. Imae, and S. Kudo. Very fast flagellar rotation. *Nature*, 371(6500):752–752, Oct 1994.

[15] Nikita Vladimirov and Victor Sourjik. Chemotaxis: how bacteria use memory. *Biological Chemistry*, 390(11), January 2009.

[16] G. D. Reilly, C. A. Reilly, E. G. Smith, and C. Baker-Austin. Vibrio alginolyticus-associated wound infection acquired in British waters, Guernsey, July 2011. *Eurosurveillance*, 16(42):19994, 2011.

[17] Rober Brown. *The miscellaneous botanical works of Robert Brown.* R. Hardwicke, London, 1866.

[18] A. Einstein. *Investigations on the Theory of the Brownian Movement.* Dover Books on Physics Series. Dover Publications, 1956.

[19] M. J. Lighthill. *Mathematical biofluiddynamics.* Number 17 in CBMS-NSF regional conference series in applied mathematics. Society for Industrial and Applied Mathematics, Philadelphia, 1989. OCLC: ocm28157225.

[20] Stephen Childress. *Mechanics of swimming and flying.* Number 2 in Cambridge studies in mathematical biology. Cambridge University Press, Cambridge, 1981.

[21] E. M. Purcell. Life at low reynolds number. *American Journal of Physics*, 45(1):3–11, 1977.

[22] E. Leifson, B.J. Cosenza, R. Murchelano, and R.C. Cleverdon. Motile marine bacteria, i. techniques, ecology, and general characteristics. *Journal of Bacteriology*, 87:652–666, 1964.

[23] Johannes Taktikos, Holger Stark, and Vasily Zaburdaev. How the motility pattern of bacteria affects their dispersal and chemotaxis. *PLoS ONE*, 8(12):e81936, 2013.

[24] L. Xie and X.L. Wu. Bacterial motility patterns reveal importance of exploitation over exploration in marine microhabitats. part i: Theory. *Biophys J*, 107:1712–1720, 2014.

[25] H.C. Berg. Chemotaxis in bacteria. *Annu. Rev. Biophys. Bioeng.*, 4:119–136, 1975.

[26] Yukio Magariyama, Makoto Ichiba, Kousou Nakata, Kensaku Baba, Toshio Ohtani, Seishi Kudo, and Tomonobu Goto. Difference in bacterial motion between forward and backward swimming caused by the wall effect. *Biophys. J.*, 88:3648–3658, 2005.

[27] Michio Homma, Hisashi Oota, Seiji Kojima, Ikuro Kawagishi, and Yasuo Imae. Chemotactic responses to an attractant and a repellent by the polar and lateral flagellar systems of vibrio alginolyticus. *Microbiology*, 142(10):2777–2783, 1996.

[28] P.M. Chaikin and T.C. Lubensky. *Principles of condensed matter physics*. Cambridge University Press, New York, 1995.

[29] Peter S. Lovely and F.W. Dahlquist. Statistical measures of bacterial motility and chemotaxis. *Journal of Theoretical Biology*, 50(2):477–496, April 1975.

[30] H.C. Berg and Douglas A. Brown. Chemotaxis in *escherichia coli* analysed by three-dimensional tracking. *Nature*, 239:500–504, 1972.

[31] Matthias Theves, Johannes Taktikos, Vasily Zaburdaev, Holger Stark, and Carsten Beta. A bacterial swimmer with two alternating speeds of propagation. *Biophys. J.*, 105:1915–1924, 2013.

[32] Li Xie, Tuba Altindal, and Xiao-Lun Wu. An Element of Determinism in a Stochastic Flagellar Motor Switch. *PLOS ONE*, 10(11):e0141654, November 2015.

[33] Philip R. Bevington. *Data Reduction and Error Analysis for the Physical Science*. McGRAW-HILL Book Company, New York, 1969.

[34] Seiji Kojima, Yukako Asai, Tatsuo Atsumi, Ikuro Kawagishi, and Michio Homma. Na-driven falgellar motor resistant to phenamil, an amiloride analog, caused by mutations in putative channel components. *J Mol Biol*, 285:1537–1547, 1999.

[35] Christine Josenhans and Sebastian Suerbaum. The role of motility as a virulence factor in bacteria. *International Journal of Medical Microbiology*, 291(8):605–614, January 2002.

[36] S. Anaid Diaz and Olivier Restif. Spread and Transmission of Bacterial Pathogens in Experimental Populations of the Nematode Caenorhabditis elegans. *Applied and Environmental Microbiology*, 80(17):5411–5418, September 2014.

[37] P. Agamuthu and Putri Nadzrul Faizura. Biodegradability of degradable plastic waste. *Waste Management & Research*, 23(2):95–100, April 2005.

[38] Joseph Teran, Lisa Fauci, and Michael Shelley. Viscoelastic Fluid Response Can Increase the Speed and Efficiency of a Free Swimmer. *Physical Review Letters*, 104(3), January 2010.

[39] J. P. Celli, B. S. Turner, N. H. Afdhal, S. Keates, I. Ghiran, C. P. Kelly, R. H. Ewoldt, G. H. McKinley, P. So, S. Erramilli, and R. Bansil. Helicobacter pylori moves through mucus by reducing mucin viscoelasticity. *Proceedings of the National Academy of Sciences*, 106(34):14321–14326, August 2009.

[40] Saverio E. Spagnolie, Bin Liu, and Thomas R. Powers. Locomotion of Helical Bodies in Viscoelastic Fluids: Enhanced Swimming at Large Helical Amplitudes. *Physical Review Letters*, 111(6), August 2013.

[41] R. B. Kimsey and A. Spielman. Motility of lyme disease spirochetes in fluids as viscous as the extracellular matrix. *Journal of Infectious Diseases*, 162(5):12051208, Jan 1990.

[42] Susan s. Suarez and Xiaobing Dai. Hyperactivation enhances mouse sperm capacity for penetrating viscoelastic media1. *Biology of Reproduction*, 46(4):686–691, 1992.

[43] Vincent A. Martinez, Jana Schwarz-Linek, Mathias Reufer, Laurence G. Wilson, Alexander N. Morozov, and Wilson C. K. Poon. Flagellated bacterial motility in polymer solutions. *Proceedings of the National Academy of Sciences*, 111(50):17771–17776, December 2014.

[44] Ch Liu, W Cheng, Jp Hsu, and Jc Chen. Vibrio alginolyticus infection in the white shrimp Litopenaeus vannamei confirmed by polymerase chain reaction and 16s rDNA sequencing. *Diseases of Aquatic Organisms*, 61:169–174, 2004.

[45] M CARMEN BALEBONA, MANUEL J ANDREU, M ANGELES BORDAS, IRENE ZORRILLA, MIGUEL A MORIN IGO, and JUAN J BORREGO. Pathogenicity of Vibrio alginolyticus for Cultured Gilt-Head Sea Bream (Sparus aurata L.). 64:7, 2018.

[46] M. Doi and S.F. Edwards. *The Theory of Polymer Dynamics*. International series of monographs on physics. Clarendon Press, 1988.

[47] Johannes Taktikos. *Modeling the random walk and chemotaxis of bacteria: Aspects of biofilm formation*. PhD thesis, Universittsbibliothek der Technischen Universitt Berlin, 2012.

[48] Yang Yang, Jing He, Tuba Altindal, Li Xie, and Xiao-Lun Wu. A Non-Poissonian Flagellar Motor Switch Increases Bacterial Chemotactic Potential. *Biophysical Journal*, 109(5):1058–1069, September 2015.

[49] T. Kadri and K. Smaili. CONVOLUTIONS OF HYPER-ERLANG AND OF ERLANG DISTRIBUTIONS. *International Journal of Pure and Apllied Mathematics*, 98(1), January 2015.

[50] Ming Chen Wang and G. E. Uhlenbeck. On the Theory of the Brownian Motion II. *Review of Modern Physics*, 1945.

[51] Y. Tu, T.S. Shimizu, and H.C. Berg. Modeling the chemotactic response of *escherichia coli* to time-varying stimuli. *Proc. Natl. Acad. Sci. USA*, 105:14855, 2008.

[52] Etienne Fodor, Cesare Nardini, Michael E. Cates, Julien Tailleur, Paolo Visco, and Frdric van Wijland. How Far from Equilibrium Is Active Matter? *Physical Review Letters*, 117(3), July 2016.

[53] P.M. Chaikin and T.C. Lubensky. *Principles of Condensed Matter Physics*. Cambridge University Press, 2000.

[54] Suddhashil Chattopadhyay, Radu Moldovan, Chuck Yeung, and X. L. Wu. Swimming efficiency of bacterium Escherichiacoli. *Proceedings of the National Academy of Sciences*, 103(37):13712–13717, 2006.

[55] S. Chattopadhyay and X.L. Wu. The effect of long-range hydrodynamic interaction on the swimming of a single bacterium. *Biophys. J.*, 96:2023–2028, 2009.

[56] Jason Swei and Jan B. Talbot. Viscosity correlation for aqueous polyvinylpyrrolidone (PVP) solutions. *Journal of applied polymer science*, 90(4):1153–1155, 2003.

[57] H Fikentscher. Systematik der Cellulosen auf Grund ihrer Vislositat in Losung. *Cellulosechemie*, 13(58), 1932.

[58] A. E. Patteson, A. Gopinath, M. Goulian, and P. E. Arratia. Running and tumbling with E. coli in polymeric solutions. *Scientific Reports*, 5:15761, October 2015.

[59] Y. K. Du, P. Yang, Z. G. Mou, N. P. Hua, and L. Jiang. Thermal decomposition behaviors of PVP coated on platinum nanoparticles. *Journal of Applied Polymer Science*, 99(1):23–26, January 2006.